INVESTIGATING THE EFFECT OF SURFACE PROPERTIES ON ICE SCALING IN EUTECTIC FREEZE CRYSTALLIZATION

MASTERS DISSERTATION

Author: Ms Lerato Motsepe

Co-supervisor: Mr. Jemitias Chivavava
Supervisor: Prof. Alison Lewis

Submitted in fulfilment of the academic requirements
for a Masters Degree in Chemical Engineering
in the Department of Chemical Engineering
at the University of Cape Town
www.crystal.uct.ac.za

2020

Declaration

I know the meaning of plagiarism and declare that all the work in the document, save for that which is appropriately acknowledged, is my own. This dissertation has been submitted to the Turnitin module, and I confirm that my supervisor has seen my report and any concerns revealed by such have been resolved with my supervisor.

Signed by candidate

…………………………………………………….

Lerato Motsepe

Acknowledgements

I am grateful to my sponsors, DRD Gold, Julian Baring and Prentec, for their financial support throughout my journey.

Thank you to my supervisors, Jemitias Chivavava and Alison Lewis, for providing me with the opportunity to be part of this research team. I have learned a lot in the CPU environment and grown as a professional. Thank you for the technical support and guidance. Thank you for believing in my ideas and for allowing me to be creative in my scientific work.

A huge thank you, Dr Marcos Rodriguez-Pascual, for teaching me and assisting me with the imaging techniques. I owe the success of this project to you! Thank you very much!

To the CPU research team, Brenda "Bee", thanks for making my time at CPU so amazing, you have been a joy! For the endless late nights in the labs, trying to get my set up to show us something, thanks "Bee". Mr Mgabhi, you have helped me settle in thanks for being such a good spirit! Thanks to Benita "Benidie" for the chats on a personal and professional level. Genevieve, "Gen" I still miss our heart to hearts. To Tawanda, thank you for your contributions, advice and great discussions, and Taona for being my number one "cheerleader". Thank you, Deborah, Ano and Jacks for your contributions and never-ending discussions. Zaeem, thank you for being there, you were great! Mel, thanks for assisting us in every way you can, you have been awesome!

Thank you, Joachim Macke, for manufacturing the main equipment ("the test cell") for this study, for always being there to assist with the lab equipment, and for the random chats of wisdom!

Curwin Nomdoe, Uthmaan Basardien, Eghsaan Matthews and Amin Jakoet thank you for the unlimited support, you guys are, undoubtedly the best!

Thanks to my friends in the Chemical Engineering Department. Sisanda thanks for being there to listen and always encouraging me to push on! TK Thanks for always being there to lighten up the mood! Zulfa, I know I found a good friend in you. Russell, thanks for the great chats and for always being able to bring laughter in the workspace.

Carol Hartley, thank you for taking the time to assist me, this document became because of you. You are greatly appreciated!

My family, as always, thank you for your patience and endless support, you have always made it easy for me to pursue my passion. Libby Modise, you are my pillar of strength, I wouldn't be where I am today without you.

To Onkgopotse Motsepe, it has been a challenging journey, thank you for being there.

Most importantly, thank God for giving me the mental, emotional, and physical strength to push through.

"Ikokobetse pele ha Morena o tla ho hodisa"

Abstract

Eutectic Freeze Crystallization (EFC) is an innovative technology that can be applied to treat reverse osmosis (RO) waste streams (brines), to produce pure salt and water. Scaling of the heat exchanger (HX) surface by both ice and salt is currently one of the major drawbacks in the industrial implementation of EFC. At present scaling is controlled by the use of mechanical scraping, which is susceptible to mechanical breakdown, thus reducing the overall process efficiency. Previous studies have shown that lower surface energy materials delay the onset of freezing, and that smooth surfaces reduce nucleation and adhesion sites, thereby reducing the probability of scale formation. Therefore, **this study aimed to investigate how the HX surface properties affect ice scaling in EFC, without the influence of mechanical scraping**. Copper, Aluminium, Stainless Steel 316 and Brass were the selected HX materials. Ice scaling on the HX materials was investigated using a near eutectic 4 wt.% Na_2SO_4 aqueous solution, in a crystallization test cell uniquely designed to mimic the region near the HX wall of a crystallizer. The Differential Interference Contrast (DIC) technique was used to study the formation of the initial ice scale layer on the HX material used in the test cell. This method of observation was effective, **as for the first time in a continuous system, the crystallization of the initial ice scale layer was observable in-situ and in real-time**. Therefore, with this method, it was possible to investigate the evolution of the predominant scaling modes (nucleation and growth), which differed for the different HX surfaces. The difference was proposed to be due to their distinct surface free energies and surface topographies. The effect of surface free energy and topography on the scaling induction time was investigated while operating at similar heat fluxes (similar cooling rates) for all the metals. The scaling induction time decreased with an increase in the surface free energy, with the Aluminium as an outlier. The recorded scaling induction times for Brass, primary-SS316 and Copper were 92.54, 70.95 and 54.06 min, respectively. Aluminium recorded the longest scaling induction time of 134.74 min. Both the p*olytetrafluoroethylene* (PTFE) coated-SS316 and the primary-SS316 HX surface were used to investigate further the effect of surface free energy on the scaling induction time. The PTFE-coated-SS316 was found to increase the scaling induction times 2.79-fold at a coolant temperature of -15°C, compared to that of the primary-SS316. However, at -20°C and -25°C, the scaling induction times on both surfaces were comparable, which indicated that the benefit of using a low surface free energy material was limited by the cooling rate of the system. It was also found that the scaling induction times were shorter when using a rough-SS316 HX plate, compared to the primary-SS316, because of the larger surface area available for heat transfer. The end of the scaling induction time was characterised by the heterogeneous nucleation and subsequent growth of the ice on the HX surfaces. There was no direct correlation between the HX surface free energy and the nucleation and growth rates. This was because the Brass, Aluminium, SS316 and Copper plates all consist of different surface topographies which also influenced the nucleation and growth rates. However, the nucleation rates consistently increased when the scaling induction times were longer, regardless of the HX material used. The presence of deep sharp crevices on the primary-SS316 also enhanced nucleation rates. These deep sharp crevices created regions of high local supersaturation, where heterogenous nucleation predominated. It was, therefore, reasonable to conclude that the ice scaling induction time was increased by using smooth materials and those of lower surface free energy. The scaling mode was dependent on the surface topography and length of the ice scaling induction time, as longer ice scaling induction times resulted in heterogenous nucleation dominated scaling mode and vice versa. Materials that had a low surface free energy and were smooth minimised the nucleation rate, resulting in a reduced overall scaling rate.

Table of Contents

List of Figures

List of Tables

0. Nomenclature

0.1. Main

Variable	Description	Unit
A	Pre-exponential factor	Nuclei.cm^{-3}s^{-1}
A	Area of heat transfer	m^{2}
B	Birefringence	-
$C_{p,c}$	Specific heat of the coolant at constant pressure	J kg^{-1} K^{-1}
J	Nucleation rate	m ^{3} s^{-1}
k	Boltzmann constant	m^{2} kg. s^{-2}K^{-1}
n^{E}, n^{O}	Refractive index for the extraordinary and ordinary rays of a light component	-
q	Volumetric flow rate	m^{3}.s^{-1}
Q	Heat flux	W.m^{-2}K^{-1}
Q_{loss}	Heat loss to the environment	W.m^{-2}K^{-1}
r_{crit}	Critical radius	m
S	Supersaturation ratio	-
t_{ind}	Induction time	s
t_{r}	Relaxation time	s
t_{n}	Nucleation time	s
t_{g}	Growth time	s
T	Temperature	°C or K
ΔT	Temperature difference between the actual and equilibrium temperature of the system, referred to as the undercooling	°C or K
ΔT_{lm}	Log mean temperature difference between the bulk temperature and the jacket temperature	°C or K
T_{actual}	The actual measured temperature of the system	°C or K
T_{eq}	The equilibrium temperature	°C or K
$T_{c, in, out}$	Coolant temperature, inlet, outlet	°C or K
T_{f}	Solution temperature	°C or K
T_{o}	Melt-solid interface temperature	°C or K

$T_{sol, in,out}$	Solution temperature, inlet, outlet	°C or K
T_w	Wall temperature on solution side	°C or K
T_i	Wall temperature on coolant side	°C or K
U_o	Overall heat transfer coefficient	W.m^{-2} K^{-1}
V_M	Molecular volume	m^{3}.mol^{-1}
W_A	Work of adhesion	J.m^{-2}

0.2. Greek Letters

Variable	**Description**	**Unit**
α_c	Heat transfer coefficient on the coolant side	W m^{-2} K^{-1}
α_0	Heat transfer coefficient on the process side	W m^{-2} K^{-1}
δ_w, δ	Heat transfer metal thickness, boundary layer thickness growing ice layer	m
f	Surface energy reduction factor	-
ΔG	Gibbs free energy of phase change	J mol^{-1}
ΔG_V	Overall free energy between a solid crystallizing particle in solution	J mol^{-1}
ΔG_v	Volume excess free energy	J mol^{-1}
ΔG_S	Surface excess free energy	J mol^{-1}
π	pi	-
γ_{sl}	the interfacial tension between the foreign surface and the bulk liquid	J m^{-2} or Nm^{-1}
γ_{sn}	the interfacial tension between the foreign surface and the nucleus	J m^{-2} or Nm^{-1}
γ_{nl}	the interfacial tension between the nucleus and bulk liquid	J m^{-2} or Nm^{-1}
γ_{lv}	The surface tension of water	J m^{-2} or Nm^{-1}
λ_w	Thermal conductivity wall	W m^{-1} K^{-1}
λ_s	Thermal conductivity crystallized solid	W m^{-1} K^{-1}
θ	Contact angle between a nucleus and a foreign substance	°
ρ_c	Density of the coolant	kg m^{3}

1. Introduction

1.1. Background

Mine impacted waters occur in different forms, i.e., as mining water, mill return water, process water, leachate, effluent and mine drainage water. All these water types have been exposed to mine workings or processes; hence they have the potential to contaminate natural water bodies if discharged or leakages occur. In addition to the pollution from operational mining sites, non-operational mines also continue to harm the environment. Bell et al. (2001) studied the impacts of an abandoned mine and found that there was a deterioration of groundwater quality due to seepage of mine impacted water, causing among other things the decreasing pH of the surrounding water resources and the increase in Total Suspended Solids (TSS) and Total Dissolved Solids (TDS). Therefore, to better control and monitor these mine waters, mining operations have implemented environmental management strategies. These strategies assist in reducing the possibility and extent of surrounding water contamination and encourage the sustainable use of water resources.

For the sustainable use of these waters, treatment processes like Reverse Osmosis (RO) are implemented to treat mine-impacted water. However, the efficiency of RO is limited by high osmotic pressures required to treat the highly concentrated (high TSS and TDS) water. Hence, RO based processes have been successful in producing potable waters, but also generate brine streams ranging from 1 % to 25 % of the feed stream (Randall and Nathoo, 2015). The concentrated brines (RO retentate) are currently stored in large brine storage ponds. The brine ponds are both costly and require large land areas, making them unsustainable in the long term. Environmental concerns regarding these brine ponds have resulted in stringent regulations leading to a search for alternative treatment options. A more sustainable solution for handling brines, is to implement treatment technologies that can minimise concentrated retentate streams, thereby eliminating the need for storage in brine ponds.

Evaporative crystallisation, a thermal-based technology, is conventionally used for treating the residual brine. This technology is energy-intensive and operates at high temperatures where corrosion of the heat exchanger (HX) surfaces can be severe (Van der Ham et al., 1998). An alternative method, Eutectic Freeze Crystallization (EFC), enables the treatment of concentrated brines by freezing. Thermodynamically, freezing is beneficial as it requires six times less energy than evaporative crystallization, resulting in reduced operational costs (Randall et al., 2011). The low operating temperatures are beneficial as they minimise the corrosion experienced in evaporative crystallization (Randall and Nathoo, 2015).

In addition, EFC exploits the eutectic properties of solutions to crystallize out pure salt and ice. This is achieved by co-crystallizing the individual salts with ice at their respective eutectic points, and then recovering the ice and salt products through density separation. The EFC process is based upon the phenomenon of ice crystallization, which excludes impurities from the crystallizing ice structure (Stepakoff et al., 1974). This characteristic of ice crystallization is valuable, as it allows the treatment of multicomponent aqueous solutions (such as brines), to produce high purity water and pure salt products (Vaessen et al., 2002).

However, the treatment of industrial brines using the EFC process has been hindered by salt and ice scaling in the crystallizer and on auxiliary equipment. This is problematic because scaling reduces the heat transfer in the crystallizer, hence decreasing the required driving force for crystallization. Scaling occurs at high-temperature driving forces, which are adapted to maximise the production rates. These high-temperature driving forces cause high local supersaturation near the crystallizer wall, which leads to excessive nucleation and subsequent ice scaling on the crystallizer wall (Myerson, 2002). In EFC, this occurs on the crystallizer cooling surface, which is the coldest region in the crystallizer. In addition, ice that crystallizes in suspension has a strong tendency to adhere to surfaces thus contributing to the scaling process through adhesion of ice crystals onto the crystallizer wall (Vaessen et al., 2002). The optimal situation, in this case, would be that ice crystallizes only in suspension, with reduced or no nucleation and adhesion onto the HX surface.

The severity of ice and salt scaling increased when treating dilute saline streams, which are saturated with sparingly soluble salts. Once supersaturated, these salts crystallize on to the heat exchanger surface, causing a salt scale layer. Salt scaling is predominantly caused by divalent metal cations, which are the source of hardness in water. Divalent ions such as magnesium and calcium are abundant in surface and ground waters, and they react with anions like carbonates and sulphates forming sparingly soluble salts. These sparingly soluble salts cause scaling on heat exchanger surfaces, and this problem has been inherited by the EFC process (Lei et al., 2011).

Considering the challenges posed by salt and ice scaling, it is necessary to develop an understanding of the factors affecting salt and ice scaling in EFC. Hence, this study focused on the physicochemical properties of the crystallizer HX surface, and to comprehend how they contribute to the severity of scaling. This will, therefore, aid in understanding the effect of surface properties, i.e., surface energy and roughness on ice and salt scaling in EFC. With this knowledge, a suitable selection of construction materials for crystallizers can be made.

1.2. Problem statement

Scaling of the Heat Exchanger (HX) surface by ice is currently one of the significant drawbacks in the industrial implementation of Eutectic Freeze Crystallization (EFC). Ice scaling becomes severe when treating dilute saline streams that are supersaturated with sparingly soluble salts; It is mainly controlled by mechanical scraping. The main drawback of mechanical scraping is the high susceptibility to mechanical breakdown, which hampers the overall process efficiency. In addition, the efficiency of scraping is dependent on the HX surface properties. This is because the surface properties affect scaling on that surface. At present, there is minimal knowledge of how the surface properties affect scaling during an EFC process.

It is imperative to decouple the effect of scraping and surface properties on ice scaling. This is to increase the understanding of the effect of surface properties on scaling, without the influence of scraping. Previous studies have shown that smoother surfaces and surfaces of lower surface energy can delay the onset of scaling through heterogeneous nucleation and adhesion (Förster and Bohnet, 1999; Qin et al., 2003; Ozbay and Erbil, 2016). However, these phenomena have not been investigated in an EFC system. Therefore, the knowledge gained from this study improves the understanding of how scaling is affected by the chosen material of construction. This will provide a starting point that enables the selection of suitable crystalliser HX materials, according to their physicochemical properties, thus, helping to reduce process downtime and improve the effectiveness of currently implemented ice scale mitigation methods such as scraping.

1.3. Aim and objectives

This study aimed to investigate the effect of Heat Exchanger (HX) surface properties on scaling in Eutectic Freeze Crystallization (EFC) of brines, without the influence of scraping.

The objectives of the study were to:

- Investigate the effect of surface free energy on the scaling induction time and scaling rate of ice during EFC,
- Investigate the influence of surface topography on the scaling induction time and scaling rate of ice during EFC and
- Use in-situ, optical methods to observe the scaling mode of the initial ice scale layer.

1.4. Scope and limitations

This project presents an investigation into how surface material of different surface energies and topography (roughness) affects scaling during crystallization. This was be achieved by using Copper, Brass, SS316, Aluminium, PTFE coated-SS316 and micro-blasted-SS316 metal plates as heat exchanger surfaces. The different thermal conductivities of the metal provide insight into the effect of temperature differences on the scaling process. A near eutectic, 4 wt.% sodium sulphate synthetic solution was used in the investigation, as it is the predominant salt in South African industrial brines (Lewis et al., 2010). In this investigation, EFC was conducted in a flow system, where nucleation and initial horizontal growth rates on the HX surface were observable in-situ, in real-time. Only horizontally scaling rates were calculated across the HX surface prior to vertical growth, as the horizontal scale represents the formation of the initial ice scale layer.

2. Theory

This chapter summarises the theory which relates to the crystallization of ice in a eutectic system. The fundamentals of crystallization such as supersaturation, induction time and metastability are discussed as they influence the nucleation and growth of the crystallizing species. Then finally, the different morphologies that occur in the crystallizing systems are considered. These fundamentals will assist in interpreting the findings from the experiments and answer the set key questions of this study.

2.1. Crystallization

Crystallization is defined as a phase change in which a crystalline product is obtained from a solution (Myerson, 2002). The process is driven by supersaturation (Myerson, 2002), which depends on temperature and concentration. There are numerous methods employed to crystallize material for separation and recovery purposes. *Table 2.1* provides a brief description of some of these technologies.

***Table 2.1**: Technologies for the crystallization of high solute concentration solutions* (Genceli, 2008; Lewis et al., 2015).

Crystallization Methods	Separation Principle	Disadvantages
Evaporative	The solvent is removed from solution through evaporation, leading to crystal formation.	High energy consumption Elevated temperature usage deteriorates organic material Poor purity.
Cooling	The solution is cooled below its saturation temperature, leading to crystallization.	The solubility of the crystallizing substance limits the yield.
Anti-solvent (AS)	Combines extraction and crystallization. An AS is introduced into the mixture and shows selective affinity with only the water molecules in that mixture, which causes components to crystallize.	AS needs to be recovered from the spent mother liquor after crystallization; therefore, extra chemicals are required.
Membrane	Integrates membrane separation and crystallization. The membrane is used to remove the solvent from the solution to create or to enhance crystallization driving force.	Scale formation on the membrane surface.
Chemical Reaction (Precipitation)	Reagents are added to form a slightly soluble compound that crystallizes out through precipitation reaction.	Poor purity.

The selection of any of these technologies depends on the properties of the solution and the desired product specifications (Lewis et al., 2015). Eutectic Freeze Crystallization (EFC) is a form of cooling crystallization that may be used in situations where a highly concentrated solution needs to be treated, and a product of very high purity is required. Using EFC, process streams of high salinity can be treated in an economically and ecologically sustainable way (Genceli et al., 2008). This is because there is no use of extra chemicals for wastewater treatment, and waste is converted to raw material in an energy-efficient manner.

2.1.1. Eutectic Freeze Crystallization (EFC)

A eutectic system is described as a homogeneous solution of chemical species, which freezes to the solid phases, so they co-crystalize into pure separate components (Randall et al., 2011). The general solubility and phase relationships based on the eutectic points are illustrated in *Figure 2.1*:

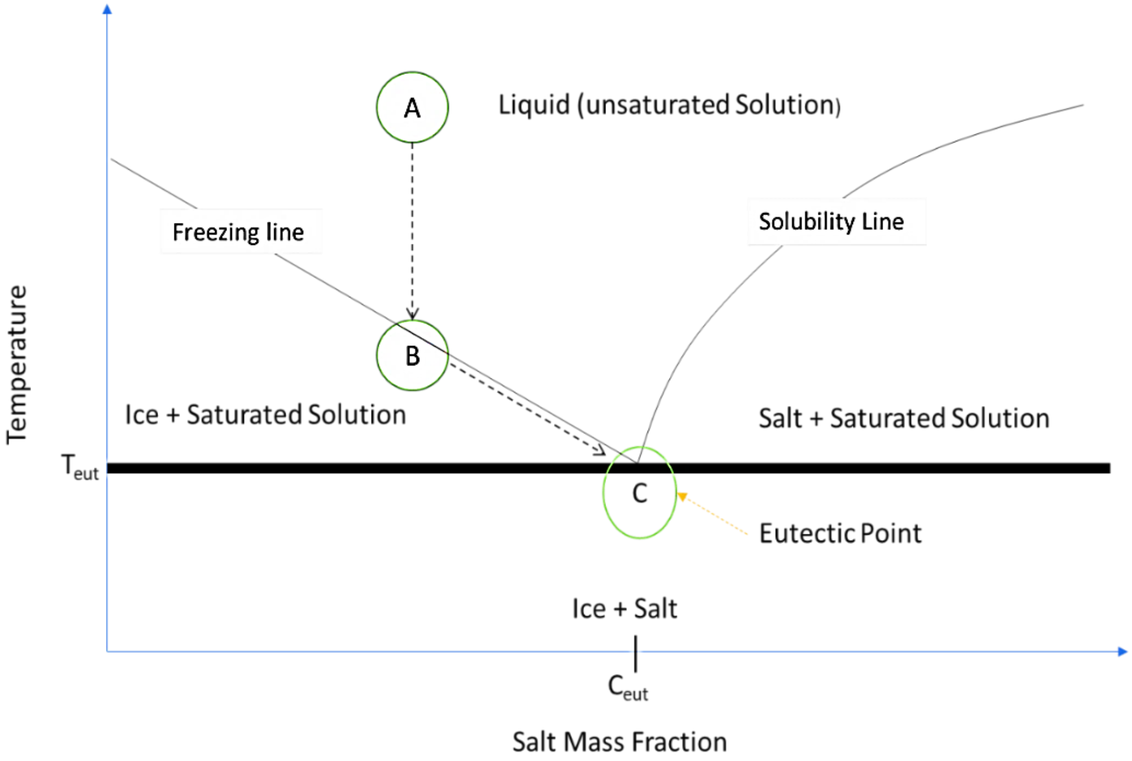

Figure 2.1*: Eutectic phase diagram of a binary system Adapted from* Genceli (2008).

Figure 2.1 illustrates a binary eutectic system, with a solvent, and two solid phases that are in equilibrium. The EFC process operates around the eutectic concentration C_{eut} and eutectic temperature T_{eut} of the aqueous solution. These eutectic points occur when the mother liquor and two solids (ice and salt) all co-exist at the same time and are in equilibrium when further cooled. The eutectic temperature is the lowest point at which a mix of solid salt and water (ice) can contain any solvent. It is the lowest possible melting temperature, where the physical mixture for the species involved co-exist (Mullin, 2001).

Using *Figure 2.1,* the principle of EFC can be described as follows: if an unsaturated solution (A) with a concentration lower (hypo-eutectic) than that of C_{eut} is cooled down to reach its freezing point, ice crystals start to form with further cooling (B). If cooling is continued, the solute concentration increases due to the formation of ice crystals along the line B to C. Upon reaching point C (eutectic point), where the ice and salt solubility lines intersect, the solute concentration reaches saturation and further cooling results in the co-crystallization of ice and salt (Genceli, 2008).

In the case where a solution starts with a higher salt concentration (hyper-eutectic) than the C_{eut}, the salt crystallizes out first, diluting the system. If cooling is continued, more salt crystallizes out along the solubility line until the system reaches its eutectic point C. The solution is now saturated with ice and any further cooling results in the co-crystallization of ice and salt. Consequently, the industrial implication of eutectic systems provides the advantage of producing pure products with a single separation step.

2.1.2. Supersaturation, induction time and metastability

Brines that are treated using EFC consist of dissolved salt species. The extent of dissolution depends on the solute, solvent and the temperature of the system. When dissolving a solute in a solvent, the resulting solution is either undersaturated, saturated, or supersaturated with respect to the solute. A supersaturated solution is not at equilibrium as it contains more solute than that required to form a saturated solution (Myerson, 2002). Therefore, this supersaturation provides the driving force for crystallization. For this reason, a solute crystallizes to relieve the supersaturation of the system and reach equilibrium (Myerson, 2002). Supersaturation is an outcome of the type of crystallizing system as some solutes are readily deposited from solution when cooled, whereas some may crystallize after some solvent has been removed (Mullin, 2001).

In cooling and melt crystallization, supersaturation can be estimated from the difference between the equilibrium (T_{eq}) and the actual temperature (T_{actual}) of the system. This difference is referred to as undercooling and can be represented by *equation 2.1*(Lewis et al., 2015). The maximum attainable degree of undercooling is dependent on the volume of the solution, the solution purity and the cooling rate of the system (Langham and Mason, 1958).

$$\Delta T = T_{eq} - T_{actual} \tag{2.1}$$

When a system has reached a point of supersaturation at a given temperature, an induction time (t_{ind}) may elapse before detectable crystals form. The induction time is defined as the period between the creation of supersaturation and the formation of a new phase (Myerson, 2002). The length of this period is mainly a function of parameters such as temperature, supersaturation, agitation, viscosity, and the presence of impurities. Hence, this period can be considered as being made of several parts which contribute to the overall induction time (*Equation 2.2*) (Mullin, 2001).

$$t_{ind} = t_r + t_n + t_g \tag{2.2}$$

The "relaxation time" (t_r) is required for a system to achieve a quasi-steady-state distribution of molecular clusters and is highly dependent on the viscosity of the solution, meaning diffusivity of the molecules (Mullin, 2001). The time required to form these critical nuclei (t_n) depends on the supersaturation, which affects the size of the critical nucleus (Mullin, 2001). The critical nuclei require time to grow to a detectable size, and this growth rate is not assumed to be similar to that of a microcrystal as they can be different (t_g) (Mullin, 2001).

Induction time determines the metastable limit (Lewis et al., 2015), which provides the boundary between the solubility and that limit, defined as the metastable zone *(Figure 2.2*). This metastable zone describes the region in the solubility diagram where a mother liquor phase is supersaturated, but has not yet responded with nucleation within a specific finite time (Beckmann, 2013).

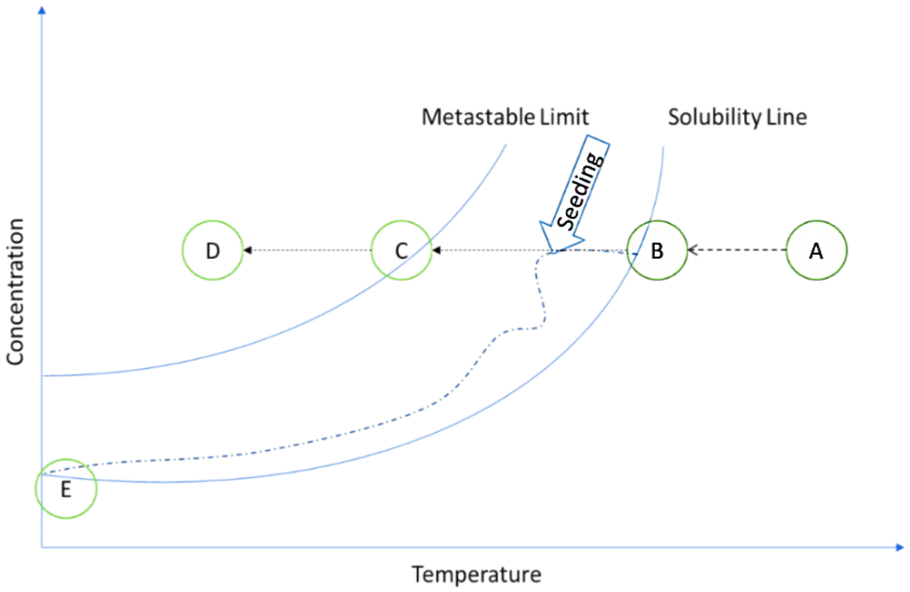

Figure 2.2*: Metastability of a solution with a change in temperature.*

The metastable zone width (B to C) is influenced mainly by the rate of supersaturation generation, which is determined by the rate of cooling and the thermal history of the phase, in the case of EFC (Beckmann, 2013). The temperature at which the first crystal is first observed varies with the cooling rate of the system (Myerson, 2002). When moving out of the metastable zone width (D), the solution enters the labile zone. In this region, spontaneous nucleation is highly probable, resulting in an uncontrolled system, where numerous small nuclei form. The density of the nuclei is an exponential function of the supersaturation (Beckmann, 2013). The region of stability of a solution is mapped out by the metastable zone, for systems with constantly increasing supersaturation, and the induction time, for systems with constant supersaturation (Beckmann, 2013). The induction time and the metastable zone width (MSZW) are related to the crystallization kinetics (nucleation rate) of a system, as they both are a function of the point when a detectable crystal is observed for a system.

Industrially, supersaturation and the metastable zone are important parameters that determine how nucleation proceeds in a crystallizer. Thus, for optimal operation, no region in the crystallizer may have supersaturations exceeding the limit of the metastable zone, to avoid primary nucleation and allow only secondary nucleation (Beckmann, 2013). The metastable zone width must, however, be exploited to a large extent so that the crystal growth rate available is sufficient (Beckmann, 2013).

2.2. Nucleation

2.2.1. Primary nucleation

Nucleation is the “birth” of new crystals and is the first step of a two-stage crystallization process (Myerson, 2002). This “birth” process can occur homogenously by spontaneous nucleation or heterogeneously by non-spontaneous nucleation. In homogenous nucleation, crystallization occurs from a solids-free supersaturated solution, while heterogeneous nucleation occurs when crystallization is triggered by a foreign substance like dust particles or a heat exchanger surface (HX) (Beckmann, 2013). Heterogeneous nucleation on the HX surfaces can cause scaling by both ice and salt.

2.2.1.1. Homogenous nucleation

Primary homogenous nucleation is based on molecular collisions within the supersaturated fluid which results in a build-up of lattice-structured bodies (aggregates and embryos) that may or may not achieve thermodynamic stability (Mullin, 2001). These embryos form clusters by the attachment and detachment of growth units (Lewis et al., 2015). In an undersaturated or just saturated solution, the system of cluster formation and cluster decay from the embryos and aggregates is in equilibrium, and the solution is stable against new phase formation (Lewis et al., 2015). However, in supersaturated solutions, the aggregates and embryos form clusters of a critical size that either re-dissolve or grow further. This depends on the free energy barrier for nucleation (Lewis et al., 2015).

The overall free energy (ΔG) between a solid and a dissolved molecule of the crystallizing species is equal to the sum of the surface excess free energy (ΔG_S) and the volume excess free energy (ΔG_V), as shown by *equation 2.3 and* 2.4 (Mullin, 2001; Myerson, 2002; Lewis et al., 2015).

$$\Delta G = \Delta G_V + \Delta G_s \tag{2.3}$$

$$\Delta G = \frac{4}{3}\pi r^3 \Delta G_v + 4\pi r^2 \gamma \tag{2.4}$$

where ΔG_v is the free energy of transformation per unit volume, γ is the interfacial tension, and r is the radius of the cluster. When minimizing the Gibbs Free Energy function with respect to the critical radius, r_{crit} can be represented as *equation 2.5*:

$$r_{crit} = \frac{-2\gamma}{\Delta G_v} \tag{2.5}$$

In classical nucleation theory, a forming cluster must reach a radius that is greater than a critical size (r_{crit}), which represents the minimum size of a stable nucleus. Beyond the critical size, the free energy for nucleation is minimised (*Figure 2.3*).

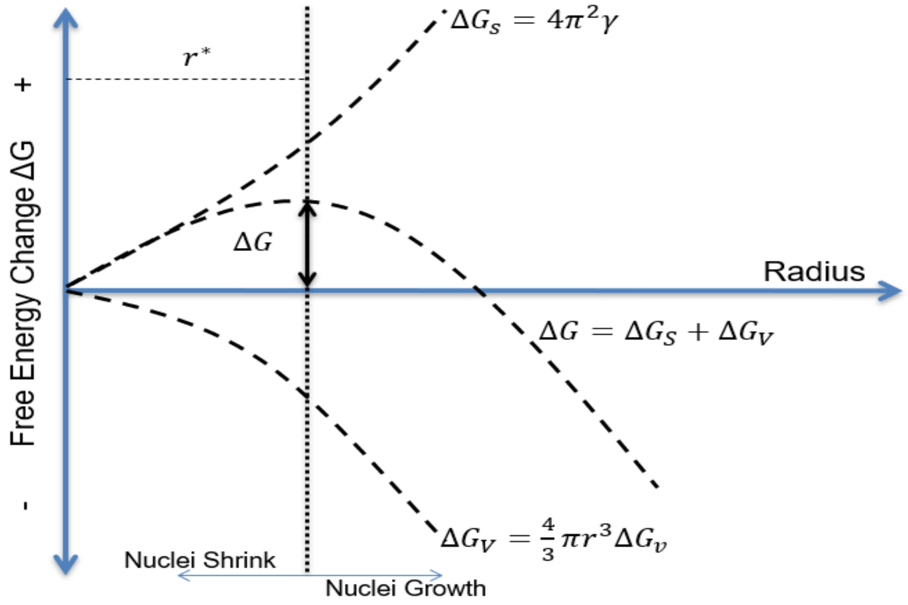

***Figure 2.3**: Gibbs free energy change for nucleation. Adapted from: Myerson (2002).*

The addition of further growth units decreases the free energy barrier ΔG_{crit} for nucleation to occur (Beckmann, 2013). The r_{crit} indicates the dependence of nucleation on the surface tension (γ) and the free energy for the transformation of a unit volume solution (ΔG_v). When high energy is required to transform a unit solution, it becomes harder for a nucleus to reach the critical radius, hence for nucleation to occur.

Energy is gained by decreasing the volume of a particle (Myerson, 2002). Therefore, when a nucleus increases in volume, energy is released, which stabilizes the nucleus. As indicated in *Figure 2.3*, the volume excess free energy change (ΔG_v) decreases as the radius of the nucleus increases. Energy is released when reducing the surface area of a particle, as indicated by ΔG_s. As the surface area increases, energy is gained by the growing nucleus, which results in an unstable nucleus. The combination of these two properties in the formation of a critical nucleus determines whether the nuclei will shrink or grow to a detectable size.

The critical Gibbs free energy is an exponential function of the supersaturation ratio as indicated by *equation 2.6*:

$$\Delta G_{crit} = \frac{16\pi\gamma^3 V_M^2}{3k^3T^3(\ln S)^2} \tag{2.6}$$

The rate of nucleation formed through this mechanism is given by *equation 2.7*:

$$J_{hom} = A_{hom} \times exp^{-(\Delta G_{crit})_{hom}} \tag{2.7}$$

Equation 2.7 indicates that the nucleation rate increases with an increase in supersaturation and decreases with the increase in surface tension (Beckmann, 2013). The rate equation predicts exponential growth once critical supersaturation is attained; however, practically an optimal temperature exists below which the liquid is too viscous to nucleate and above which molecular motions prevent crystal formation (Myerson, 2002). Therefore, excessive cooling does not necessarily aid nucleation after the attainment of critical supersaturation when crystallizing a dilute solution (Mullin, 2001).

2.2.1.2. Heterogeneous nucleation

The presence of a foreign surface in a supersaturated solution is generally known to reduce the overall ΔG_{crit} energy barrier that needs to be overcome for the creation of a critical nucleus. This is because the foreign surface facilitates the transition for an embryo to form on it and reach a critical size (Vali, 2008). Consequently, heterogeneous nucleation occurs at a lower supersaturation than homogenous nucleation, as the free energy barrier $(\Delta G_{crit})_{het}$ is lower than that for homogenous nucleation $(\Delta G_{crit})_{hom}$ (Beckmann, 2013). The rate of primary heterogeneous nucleation is given by *equation 2.8*:

$$J_{het} = A_{het} \times e^{-f(\theta)\cdot(\Delta G_{crit})_{het}} \tag{2.8}$$

where J_{het} can be measured by area (for nucleation on a surface) or length (for nucleation along a line) (Bi et al., 2017). A_{het} is the pre-exponential factor, which in the presence of dissolved impurities and physical features like, crystallizer walls, stirrers, baffles it is 10^3 to 10^5 (Beckmann, 2013). The extent of the $(\Delta G_{crit})_{het}$ barrier depends on the supersaturation level (S) of the system, and the contact angle (θ) of the nuclei on the foreign substrate surface (Keysar et al., 1994).

According to the classical nucleation theory, a decrease in the contact angle between the ice subcritical cluster and the surface minimises the free energy for nucleation (ΔG_{crit}). In this approach, three assumptions are made, namely: the nucleus on the foreign surface is cap-shaped rather than multifaceted, the boundary of the nucleus is well defined rather than diffusive, and microscopic interfacial free energies are the same as those of macroscopic crystals (Diao et al., 2011). However, limitations to these assumptions have been shown, which highlight that this approach is not intended for accurate description and prediction of the effect of substrates on heterogeneous nucleation (Diao et al., 2011). This is because the contact angle between a crystal and a solid is not a well-defined property, as in the case of vapour-liquid transition against a surface (Alizadeh et al., 2012; Lupi et al., 2014). Thus, Alizadeh et al. (2012), suggests that the ice nuclei-surface contact angle can be used as an effective parameter to represent the degree of wetting of the ice nucleus against the surface, granted it does not necessarily mirror the conventional liquid-surface contact angle. Therefore, the contact angle is preferably used to estimate the extent of interactions between the nucleus and the foreign surface in a solution environment from a perspective of interfacial tensions (Diao et al., 2011).

Figure 2.4 illustrates the interfacial tensions at the boundaries between a nucleus which results in wetting of the foreign surface. Wetting occurs when a solid surface forms an interface with a liquid to reduce its free energy. *Figure 2.4 (a)* illustrates wetting on a foreign surface of low surface energy, which results in de-wetting as indicated by the high contact angle (105°). *Figure 2.4 (b)* illustrates wetting on a foreign surface of high surface energy, which results in the wetting of the surface as illustrated where the contact angle is lower (47°).

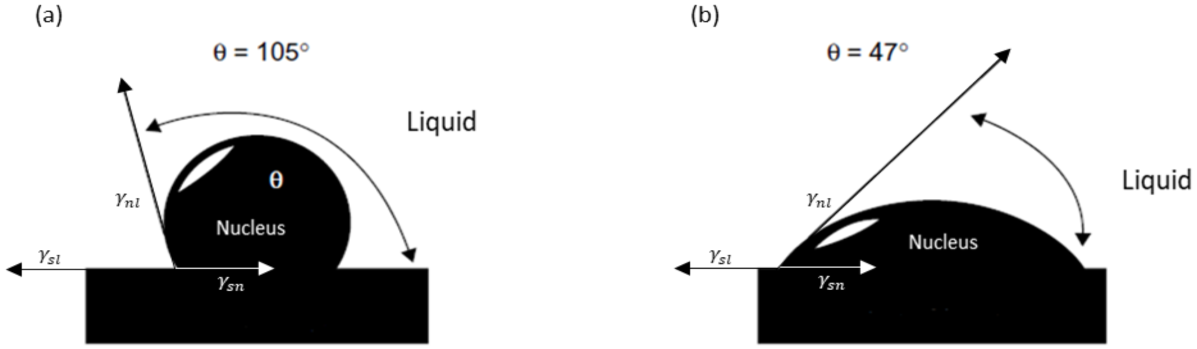

***Figure 2.4**: Contact angle of a nucleus crystallizing on a surface of low surface free energy (a) and of high surface free energy (b). Adapted from source: Mullin (2001), Mattox (2010) and Diao et al. (2011).*

Therefore, the wetting of the surface by the nucleus is increased as the contact angle decreases. This interaction of a nucleus with a solid can be described by Young's *equation 2.9*.

$$\cos\theta = \frac{\gamma_{sl} - \gamma_{sn}}{\gamma_{nl}} \qquad 2.9$$

Young's equation provides a relationship between three interfacial tensions in equilibrium. They are denoted by γ_{sl} (the interfacial tension between the foreign surface and the bulk liquid), γ_{nl} (the interfacial tension between the nucleus and bulk liquid), γ_{sn} (the interfacial tension between the foreign surface and the nucleus) and θ (the contact angle between the solid surface and nucleus). The contact angle of a nucleus corresponds to the angle of wetting in liquid-solid systems (Mullin, 2001).

The extent at which a surface is wetted affects the surface energy reduction factor, $f(\theta)$, as it is a function of the contact angle (θ), as indicated by *equation 2.10:*

$$f(\theta) = \frac{(2 + \cos\theta) \cdot (1 - \cos\theta)^2}{4} \tag{2.10}$$

Equation 2.10 indicates that the contact angle (θ) decreases from a completely non-wetting condition where θ = 180°, to a complete wetting condition where θ = 0°. The energy reduction factor varies from $f(\theta) = 1$, where no reduction in energy occurs, to $f(\theta) = 0$, where there is no energy barrier to overcome. *Table 2.2* summarises the trend indicating the dependence of the surface energy reduction factor on the contact angle of the nuclei.

Table 2.2: *Surface energy reduction factor for heterogeneous nucleation. Source: Mullin (2001) and Beckmann (2013)*

Contact angle (θ), (°)	**Surface energy reduction factor $f(\theta)$**
0	0
5	1.80×10^{-5}
10	1.72×10^{-4}
30	1.29×10^{-2}
45	5.81×10^{-2}
60	1.56×10^{-1}
90	0.5
120	0.84
180	1

From *Table 2.2*, it is evident that, when θ = 180°, cos θ = -1, hence $f(\theta)$ = 1, then *equation 2.11* holds true.

$$(\Delta G_{crit})_{het} = (\Delta G_{crit})_{hom} \tag{2.11}$$

This implies that the foreign surface is completely non-wetting. Therefore, the overall free energy will be the same as that for homogenous nucleation, which requires a higher supersaturation for nucleation to occur. When θ lies between 0° and 180°, i.e. $f(\theta) < 1$, then the Gibbs free energy required for heterogeneous nucleation to occur will be less than that of homogeneous nucleation (*Equation 2.12*).

$$(\Delta G_{crit})_{het} < (\Delta G_{crit})_{hom} \tag{2.12}$$

This implies that the energy required for a crystal to form on the specific foreign surface is lower, and nucleation becomes easier on the surface, due to partial wetting. When θ = 0°, then $f(\theta) = 0$. Therefore, the energy to be overcome tends to zero (*Equation 2.13*).

$$(\Delta G_{crit})_{het} = 0 \qquad 2.13$$

In this case, there is a complete affinity of the crystallizing material on the foreign surface due to complete wetting. When there is complete wetting of a foreign surface, there is little to no energy to be overcome for nucleation to occur on this surface, making heterogeneous nucleation highly likely (Mullin, 2001).

In summary, as θ is reduced, the affinity between a nucleus and a solid surface increase. Consequently, the surface energy reduction factor decreases, resulting in a reduction of the free energy barrier (ΔG_{crit}) for heterogeneous nucleation. Therefore, surface wettability plays a crucial role in determining the extent at which the surface free energy ΔG_{crit} can be reduced for nucleation on the foreign surface.

2.2.1.3. Foreign surfaces and heterogeneous nucleation

A foreign surface, such as a crystallizer wall, has properties that are different from those of its bulk material (Petrenko and Whitworth, 2002). The fundamental source of this difference is that molecules at the free surface only experience bonding forces to other molecules from one side, which results in a similar imbalance on the opposite side (Petrenko and Whitworth, 2002). This results in the displacement of atoms from their normal sites, changes in the energies and force constants, and consequent effects on the layers below the surface (Petrenko and Whitworth, 2002). This imbalance results in excess energy at the surface in comparison to the bulk of the surface. The unrealised bonding energy results in the surface free energy of the solid foreign surface.

Surface free energy is the work required to increase the surface area of a solid phase (Mattox, 2010). The surface free energy becomes higher if the exposure of the free surface area is increased, and if there are stronger bulk interactions (Mattox, 2010). In addition, the properties of the free surface area are dependent on the nature of the adsorbed medium, which may be a vacuum, water, vapour, or air (Petrenko and Whitworth, 2002). Consequently, the level of surface free energy can be used as an indicator of both contamination and the composition of the surface material (Mattox, 2010).

Adsorption is adhesion that occurs due to intermolecular forces that bind a substance to a different surface, such as ice to a metal surface. Through the adsorption process, exposed surface molecules with high energy are reduced through replacement with lower energy molecules such as hydrocarbons (Mattox, 2010). The strength of adhesion between two different materials is defined as the 'work of adhesion' (W_A). W_A is the free energy required to separate a boundary of the unit area between two media (Petrenko and Whitworth, 2002). The work of adhesion between a liquid and surface is indicated by *equation 2.14*:

$$W_A = \gamma_{LV}\,(1 + \cos\theta) \qquad 2.14$$

where θ is the contact angle and γ_{LV} is the water surface tension. For water on different surfaces, the value of W_A can be deduced from the contact angles (Petrenko and Whitworth, 2002). Because the interfacial energies of water molecules to different surfaces are expected to be similar in water and ice, it may be supposed that the values of W_A on different ice-surface interfaces will be correlated with the angles of contact of water on these surfaces (Petrenko and Whitworth, 2002).

Most liquids have lower surface tension than the surface free energy of solid materials. This difference is due to their weak cohesive intermolecular forces, which results in the wetting property of these liquids. Cohesion occurs as a result of intermolecular forces that bind similar molecules to one another, such as the hydrogen bonding in water (Andrews and Lockington, 1983). Cohesive forces of molecules cause the surface of a liquid to contract to the smallest possible surface area by pulling inwardly, creating what is called surface tension. Surface tension is the resistance of a fluid to deformation. This resistance is due to the enhancement of the intermolecular forces at the liquid's surface, due to force imbalances, as illustrated in the following figure.

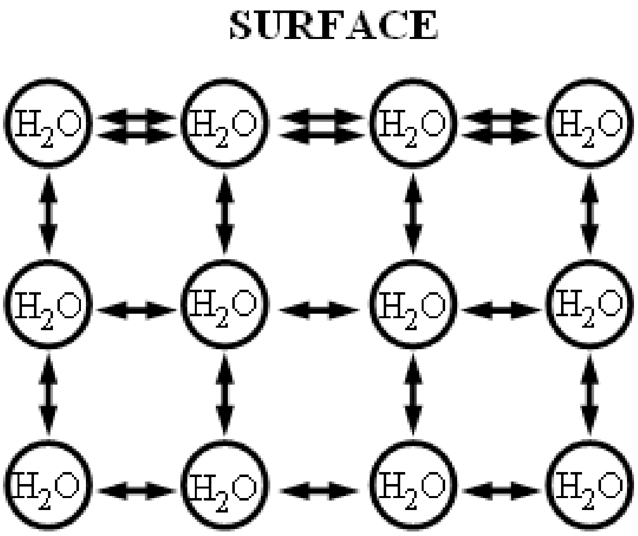

Figure 2.5*: Surface tension of a water droplet (double arrows) due to increased cohesive forces at its surface. Source:* https://www.usgs.gov/media/images/surface-tension-forms-a-strong-bond-surface-a-water-body

Figure 2.5 indicates the enhancement of cohesive forces due to an imbalance of intermolecular forces (double arrows) for molecules at the surface. These molecules at the surface are at a higher energy state than the molecules within the bulk, leading to surface tension. The surface tension exists to minimise the surface area, hence minimising the surface energy at the surface. This surface tension is overcome by the application of a measure of force, required to break a film of a unit length (*Equation 2.15*).

$$Surface\ Tension = \frac{Force}{Meter}\left[\frac{N}{m}\right] \tag{2.15}$$

Similarly, the surface tension of a fluid increases as its temperature decreases. This indirectly proportional relationship stems from the decrease in kinetic energy of the molecules as temperature decreases. The amount of kinetic energy is related to temperature as crystallization occurs. The average kinetic energy of molecules can, therefore, be said to be proportional to the absolute temperature (Myerson, 2002).

The data in *Figure 2.6* indicates that the surface tension of water is a perfectly linear function of temperature (Gittens, 1969). With a decrease in temperature, the kinetic energy weakens, which increases the strength of cohesive forces, leading to an increase in surface tension. Adhesion is also known to increase with decreasing temperature, which results in the stronger in the interfacial tensions between the nucleus and solid surface, thus giving rise to two-dimensional (2D) nuclei (Heydari et al., 2016).

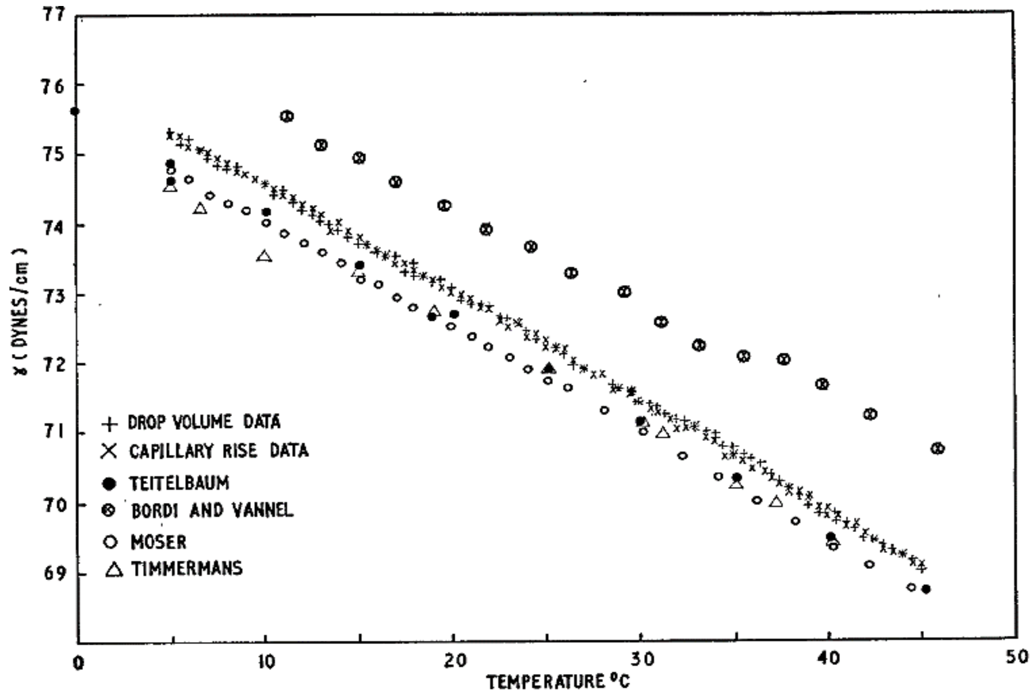

Figure 2.6: *The variation of surface tension with water temperature. Source: Gittens (1969).*

As a result, the rate of 2D nucleation is a strong function of temperature and supersaturation on the crystallizer surface during EFC (Myerson, 2002). *Figure 2.7* illustrates the process of forming a 2D nucleus on a solid flat surface through adhesion. In 2D nucleation, molecules are continually absorbing (a) on the surface, diffusing (b) and desorbing (c) (Myerson, 2002). Molecules also collide (d) with each other and form 2D clusters (Myerson, 2002).

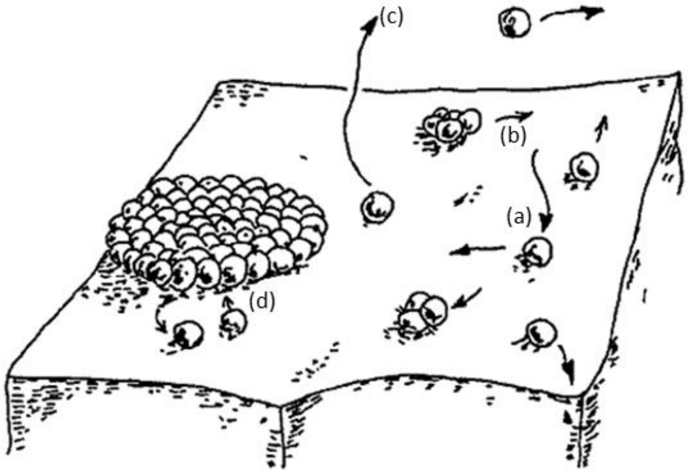

Figure 2.7*: Formation of a two-dimensional critical nucleus on a crystal surface. Source: Myerson (2002).*

Therefore, this decrease in temperature increases the supersaturation near the cooling surface, which may enhance the rate of 2D heterogeneous nucleation (Myerson, 2002). At this point, the surface free energy of the HX surface becomes of significant importance as it contributes to the force of interaction between itself and the molecular clusters, as shown in *Figure* 2.7. Once a critical nucleus is reached, scaling through primary heterogeneous nucleation commences.

2.2.2. Secondary nucleation

Secondary nucleation together with primary heterogeneous nucleation is highly influential in industrial crystallization as it provides a method of controlling a crystallization process by introducing seeds into a supersaturated solution. These parent crystals have a catalysing effect and act as templates that induce crystallization in a supersaturated solution. The introduction of seeds can induce nucleation at lower levels of supersaturation, allowing for control of the system by preventing spontaneous nucleation (Mullin, 2001; Beckmann, 2013).

Secondary nucleation can be summarised into three categories: true, apparent, and contact secondary nucleation (Mullin, 2001). True secondary nucleation occurs when embryos, or nuclei of subcritical sizes, are introduced into a solution of low supersaturation, where primary nucleation is negligible. If these nuclei survive, the addition of subcritical clusters can induce nucleation at observable rates. The addition of these sub-critical clusters reduces the activation energy nucleation (Mullin, 2001). This process occurs through both dendritic breeding (i.e. the detachment of weak outgrowths) and polycrystalline breeding (i.e. the fragmentation of weak polycrystalline mass) (Lewis et al., 2015). Apparent secondary nucleation occurs when small fragments are washed from the surface of a crystal and then reintroduced into the solution. This process is called initial or dust breeding, which is predominant in industrial crystallization (Lewis et al., 2015). Contact nucleation or collision breeding is the most significant secondary nucleation mechanism in high to moderately soluble solutes in the crystallizing process. This prevalence is caused by its high dependence on the operational parameters of the crystallizer (Genceli et al., 2008). This type of nucleation occurs through a process called collision breeding, a complex process resulting from the interaction of crystals with one another or with parts of the crystallization vessel such as HX surfaces (Mullin, 2001).

2.3. Crystal growth

Growth is the second step in crystallization after nucleation, where the nucleus increases in size through the addition of either solute or solvent molecules from the surrounding supersaturated solution. The growth process occurs in three stages: diffusion of molecules from the bulk solution through the boundary layer around the crystal, incorporation into the crystal lattice, and transport of heat of crystallization from the crystal into the bulk solution and HX surface In a dilute solution, with water as a solvent, the mass diffusion of solute molecules from the bulk on to the growing crystal face plays an important role in crystal growth. However, in the case of ice growth in the dilute solution, heat transfer plays an essential role in the rearrangement of atoms at the solid-liquid interface through heat removal (Sunagawa, 2007). Therefore, this section will focus on surface integration and heat transfer which are the main influencing factors in the growth of ice, as opposed to the mass transfer of rejected solutes (Hasan and Louhi-Kultanen, 2015).

2.3.1. Surface diffusion and integration kinetics

Various theories such as those that focus on the surface energy, the adsorption layer and two-dimensional growth have been developed to explain the mechanisms of the growth process (Mullin, 2001; Myerson, 2002). Although not completely abandoned, the surface energy theories have been found deficient due to limited quantitative evidence to support them (Mullin, 2001). The adsorption layer theory, and its subsequent developments, indicate the critical features of layer growth and highlight the role of surface inhomogeneities on the growth process (Mullin, 2001).

The adsorption layer theory suggests that when units of a crystallizing substance arrive at the crystal face, they lose a degree of freedom and are free to migrate over the crystal face through surface diffusion (Mullin, 2001). Ultimately, the migrating units integrate at the active centres on the surface. This migration results in a stepwise build up until the crystal face is completely formed. In addition to this theory, the Kossel theory explains the role of step and kink sites in the growth process of crystals (Mullin, 2001). This theory suggests that a flat crystal surface has steps of atomic height which contain more than one kink site (Mullin, 2001). These kink sites may arise due to 2D heterogeneous nucleation on a crystal surface. Growth units are easily incorporated into the crystal at these kinks, which diffuse along a step, eventually creating a complete face (Mullin, 2001).

However, the theory was not sufficient to explain the continuous growth of a crystal surface due to its dependence on 2D nucleation. To explain this phenomenon, dislocations are identified to provide the sources of steps required for the continuous growth of a crystal (Mullin, 2001). The screw dislocations are vital since they remove the necessity for surface nucleation while enhancing the growth of a surface. The growth rate from these dislocations is dependent on the degree of supersaturation (*Figure 2.8*)(Mullin, 2001).

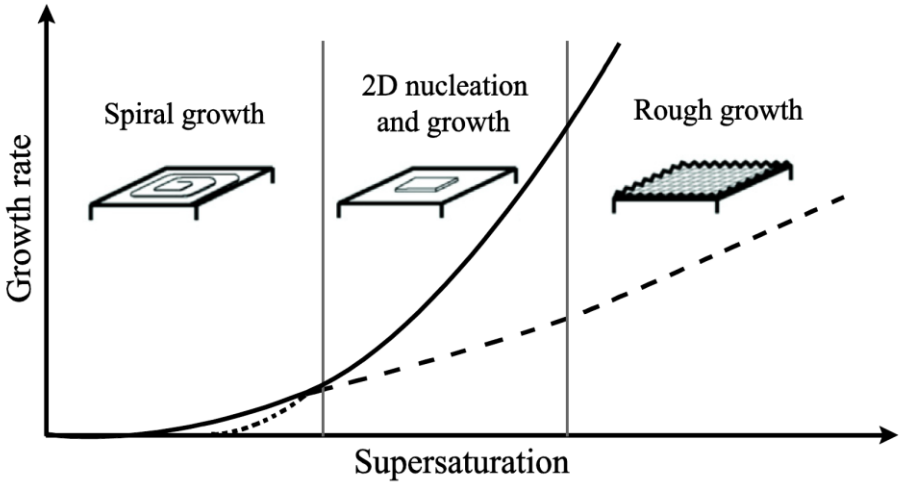

***Figure 2.8**: Progression of growth mechanisms with an increase in supersaturation. Source: Li et al. (2016).*

At low supersaturation levels, the spiral growth mechanism (solid line) is faster than 2D nucleation and growth (dotted line) and is the dominantly observed mechanism. The growth step starting from such a step advances like a spiral staircase around a dislocation. Since screw dislocation is a self-perpetuating step source, it is not necessary to overcome the energy barrier for two-dimensional nucleation. Crystals can grow by this mechanism below the critical driving force for layer-by-layer growth (Sunagawa, 2007).

Above a certain level of supersaturation, however, the 2D nucleation growth rate (now drawn as a solid line) can overtake the spiral mechanism (the dashed line represents a continuation of the spiral growth rate expression). Once a nucleus forms on the HX surface, it then spreads to form a complete layer through the rearrangement of atoms at the solid-liquid interface. Two-dimensional growth theories describe the growth models of 2D surface nuclei to complete a layer. These include the mononuclear, the polynuclear, and the birth and spread models (Myerson, 2002). The mononuclear model assumes that when a surface nucleus has formed, it spreads across the HX surface at an infinite velocity (Myerson, 2002). The surface must be completely covered before the formation of another surface nucleus, which is the rate-determining step. If, however, it is assumed that the nuclei that form on the surface do not spread at all after forming, then the layer would form by the nucleation of enough 2D nuclei of critical size to cover the entire surface (Myerson, 2002). This is known as the polynuclear model. In between these two extremes is a model called the birth and spread model. This model allows for the spreading of nuclei at a finite constant rate that is assumed to be independent of size (Myerson, 2002). It also assumes that nuclei can form at any location, including incomplete layers, and that there is no intergrowth between the nuclei (Myerson, 2002).

Eventually, increasing the supersaturation level causes a smooth interface to change into a rough interface, called roughening transition. A roughening transition resulting from increasing levels of supersaturation is called a kinetic roughening transition (Sunagawa, 2007). A rough growth regime may be reached as kink sites increase with the increase in supersaturation at the interface. Therefore, it is evident that as the supersaturation level rises with the increase in heat transfer, the interface becomes rougher.

2.3.2. Heat transfer

Crystal growth in a dilute solution occurs predominantly by the rearrangement of the atoms at the liquid-solid interface through the removal of heat (Sunagawa, 2007). Therefore, heat transfer plays a vital role as the driving force in processes of ice crystallization, as the mass transfer is not significantly involved. In most industrial crystallizers, heat transfer occurs through indirect cooling. This may result in 2D nucleation and subsequent growth on the HX surface, from the high driving force created near the HX surface. As with nucleation, growth is an exothermic process, as energy is given off when crystallization occurs. The energy required for crystallization of one mole of a substance is referred to as the enthalpy of crystallization (Van't Land, 2004). This energy is given off as heat and consumes the supersaturation as the ice layer continues to grow. As the layer cools down, it thickens, and this is generally called the enthalpy effect (Van't Land, 2004). The development of this ice layer creates an added resistance to heat transfer, hence diminishing the overall heat transfer in the EFC process.

Heat transfer through a cooling surface directly affects the crystallization process efficiency, and, as a result, the production capacity (Vaessen et al., 2004). It is therefore critical to control operating parameters affecting heat transfer to improve the efficiency of the crystallization process. The overall heat balance around a crystallizer is indicated by *equations 2.16* and *2.17*:

$$\dot{Q}_{overall} = UA\Delta T_{lm} + \dot{Q}_{loss} \tag{2.16}$$

$$\dot{q}\rho_c \; C_{p,c}\left(T_{c,out} - T_{c,in}\right) = UA\Delta T_{lm} + \dot{Q}_{loss} \tag{2.17}$$

The overall heat transfer coefficient (U) across a heat exchanger surface consists of the following resistances: the possible fouling layer caused by the coolant on the surface, the thickness of the heat exchanger wall, the scaling layer formed by the solution being cooled and the boundary layer formed by the fluid flowing in close contact with the heat exchanger surface shown by *equation 2.18*:

$$\frac{1}{U_o} = \left[\frac{1}{\alpha_c} + \frac{\delta}{\lambda_s} + \frac{\delta_w}{\lambda_w} + \frac{1}{\alpha_o}\right] \tag{2.18}$$

where U_o is the overall heat transfer coefficient Where, δ is the ice layer thickness, δ_w metal wall thickness, α_c is the heat transfer coefficient (medium side), λ_w is the metal wall thermal conductivity, λ_s is the solid thermal conductivity, α_0 is the heat transfer coefficient (process side). These parameters are presented in *Figure 2.9*:

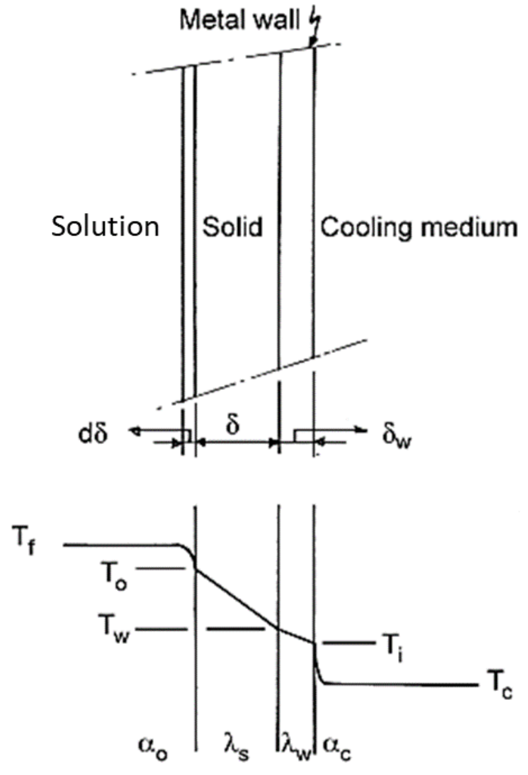

Figure 2.9: *Scaling on a cooled surface with temperature as the crystallization driving force. Source: Van't Land (2004).*

Figure 2.9 provides an illustration of the general solidification process on a cooling wall through crystallization. The temperatures of the cooling medium and metal surface are both lower than that of the liquid solution. The temperature T_f, is assumed uniform due to mixing in the bulk solution, and it decreases across the boundary layer to $T_{0,}$ which is at the melt-solid interface temperature. The temperature continues to decrease from T_o to T_w across the solid layer, and from T_w to T_i across the metal wall to a uniform coolant temperature of T_c.

The highest supersaturation due to temperature difference is found near the surface of the cooling wall, which leads to the crystallization of ice on the cooling wall. The crystallization of this ice scale layer may occur through heterogeneous nucleation, growth, adhesion, and fusion of already crystallized particles in the bulk medium. Ultimately, the supersaturation generated influences the resulting ice scale structure and morphology.

2.4. Crystal structure and morphology

Crystal growth occurs by the rearrangement of atoms at the solid-liquid interface through the removal of heat, which is required for atomic rearrangement to occur. As a result, low supersaturation levels result in atomically smooth interfaces, and high supersaturation levels result in rough interfaces, thus defining the surface morphology of a growing ice layer (*Figure 2.10*) (Sunagawa, 2007). Therefore, as the crystal growth mechanisms change with supersaturation, so does the resulting crystal morphology. The growth process affects crystal morphology by altering size and habit. The resulting morphology affects the purity, perfection, strength, and abrasion resistance of the resulting crystal. These crystal properties are essential in the final product specifications (Garside, 1985; Myerson, 2002).

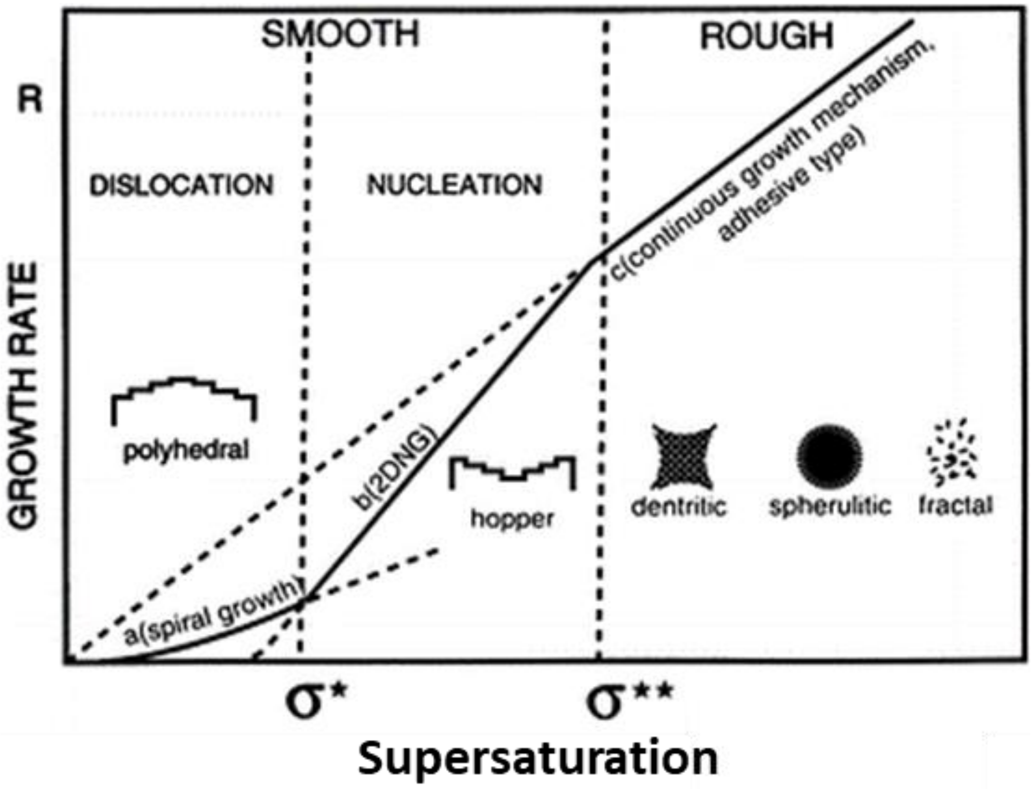

Figure 2.10: *Changes in the morphology of crystals, shown on growth vs driving force as supersaturation. Source: Sunagawa (2007).*

The crystal morphologies expected are those of a polyhedron bounded by flat faces, when the growth mechanism is of a spiral growth. In the region where 2D nucleation occurs, a hopper morphology is expected, while a dendritic and spherulitic type of crystal morphology forms when the growth mechanism is of the rough, adhesive type (Sunagawa, 2007). This range of crystal morphology from polyhedral to dendritic is exhibited by single crystals (*Figure 2.10*).

When crystals consist of both smooth and rough interfaces, continued growth will result in a complete smooth polyhedral interface (Sunagawa, 2007). This is a result of diminishing supersaturations as growth proceeds, implying that an initially dendritic crystal ultimately becomes a smooth polyhedral one. The dendritic growth can be seen through a cross-sectional view of the crystal, which will show the progression of the crystal morphology. The changes in crystal morphology with temperature can be represented by a morphodrom (*Figure 2.11*).

This diagram depicts the relation between the ice crystals of different morphologies in relation to the supersaturation of a water system.

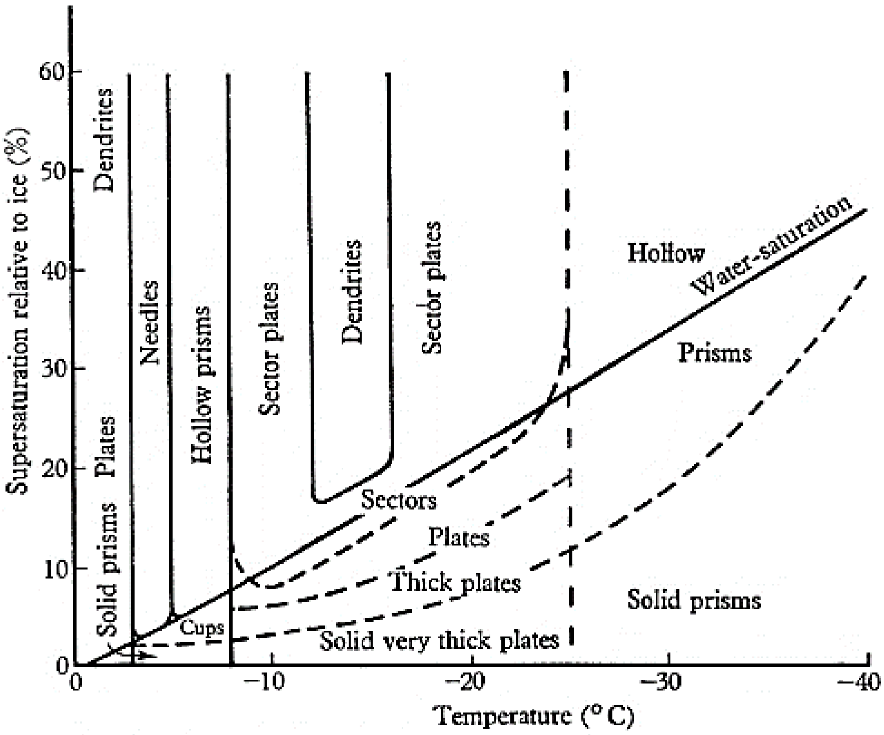

Figure 2.11: *A morphodrom indicating the variation of crystal habit with temperature and supersaturation. Source: Sunagawa (2007).*

Figure 2.11 indicates that crystals take on a polyhedral morphology in the region of low supersaturation of water, whereas they assume a dendritic morphology in the regions of high supersaturation. This phenomenon is due to the crystal comprising many faces with different orders of morphological importance (Sunagawa, 2007). The graph indicates that a face with a lower order of morphological importance will show roughening transition at a lower temperature and driving force than does the face with a higher order of morphological importance (Sunagawa, 2007). As a result, there will be changes in the morphology with the changes in temperature and supersaturation.

2.4.1. Crystal optical properties

The ice crystal is known to be an anisotropic, uniaxial crystal, which belongs to the hexagonal crystal systems (Murphy et al., 2020). This classification means that ice is an example of a weakly birefringent crystal which appears bright with interference colours on a dark background (Petrenko and Whitworth, 2002). The birefringence property, also known as double refraction, is a property of optical crystals where an incident ray of light passing through the material results in two refractive indices. These refractive indices are called the ordinary (n^O) ray, which travels parallel to the electric field, and extraordinary *(n^E*) ray which travels perpendicular to the electric field (Yamamoto, 2012). For ice, the refractive index for the n^E is larger than the refractive index for the n^O. Consequently, ice is has a positive birefringence at -3.6°C for refractive indices at 589nm, as indicated by *equation 2.19* (Petrenko and Whitworth, 2002).

$$Birefringence(B) = |n^E - n^O| \qquad 2.19$$

$$Birefringence(B) = |1.3105 - 1.3091| = 0.0014$$

The n^O and n^E rays are mutually perpendicular to each other and travel at different characteristic velocities in an ice crystal. Each ray emerges from the crystal with a path difference called the retardation, which is measured in nanometres (nm) (Delly, 2012).

Differential interference contrast (DIC) techniques can be used to observe the retardation resulting from a transparent ice specimen of a specific thickness (*Figure 2.12*). The technique makes use of the birefringent property and the thickness of the specimens. The retardation increases linearly with the birefringence and thickness of the specimen (Delly, 2012). Since the birefringence of ice is a known constant variable at a specific temperature, the retardation will increase with the thickness of ice observed under DIC.

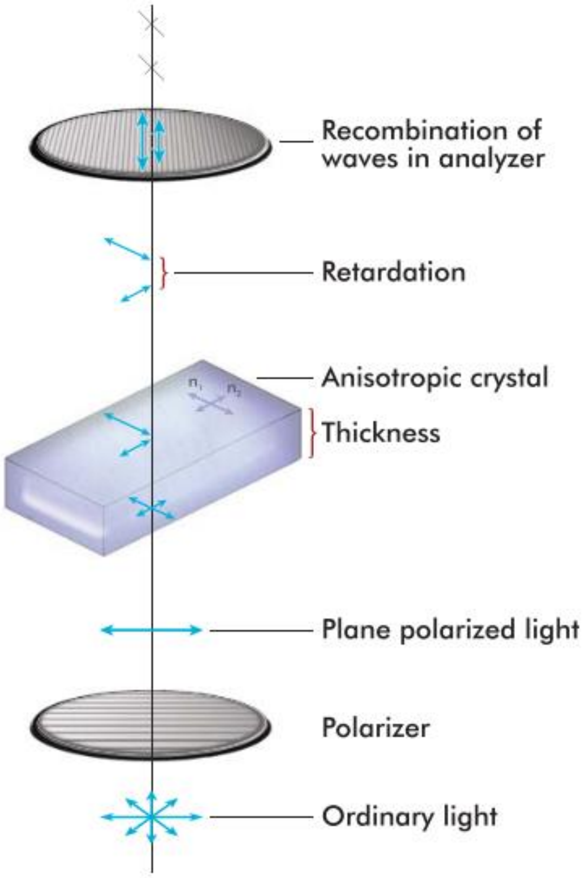

***Figure 2.12**: Polarised light passing through an anisotropic, birefringent crystal. Source: Delly (2012).*

Figure 2.12 shows ordinary light that is linearly polarised, and this incident light enters a crystal at 45° to the *c*-axis. The maximum brightness for a birefringent material is observed along the optical axis of a crystal oriented at 45° to both the polarizer and analyser (Murphy et al., 2020). The incident ray is resolved into the ordinary (n^o) and extraordinary (n^E) components which are responsible for the birefringent character of ice (Petrenko and Whitworth, 2002).

The n^O and n^E rays emerge from the birefringent ice crystal vibrating at right angles to one another, passing through the analyser in the same plane. The waves follow different optical path lengths (retardation) due to the differences in the thickness or refractive index at the point of passing through the sample. This results in a phase shift of one wave compared to another. Interference (constructive or destructive) occurs between the waves passing through the analyser. The overall result is that some birefringent samples gain a spectrum of colour when observed in white light through cross polarizers (Murphy et al., 2020). Thereafter, the waves are focused by the objective lens, and an elliptically polarised light is generated and recombined to one wave. This light passes through the analyser and produces plane-polarized light having a finite amplitude and ultimately generating an image of the forming ice scale layer (Lang, 1968).

Quantitative analysis of the interference colours observed in the birefringent ice scale can be accomplished using the Michel Lévy chart (*Appendix A.4*)(Sørensen, 2013). The graph indicates that the polarization colours visualised in the digital recordings can be associated with the retardation, thickness, and birefringence of the ice (Sørensen, 2013). If two of these three required variables are known, the third variable can be obtained from the chart. In the case of ice in this study, the retardation, and the birefringence of ice are both known. Therefore, it is possible to extrapolate the angled lines back to the ordinate, with the result that the thickness of the ice can be estimated as it forms. *Table 2.3* provides approximate thicknesses of the ice scale layer at its different retardations, according to the Michael-Lévy chart.

Table 2.3 *Ice thickness in relation to the retardation and the ice refractive index of 1.3. Data extracted from Michael-Lévy chart Delly (2012)*

Retardation (nm)	**Approximate Thickness (nm)**
Black	25 - 35
Grey	35 - 80
White - Yellowish White- Light Yellow	80 - 125
Bright Yellow	130 - 170
Brown Yellow	170 - 190
Red Orange	190 - 200
Indigo	Thickness > 200

Using the observed colours, which represent the retardation indicated by the polarised light on to the scaling ice, it is possible to use the Michael-Lévy chart to obtain the relative thickness correlated to the birefringence of ice and this observed retardation (Delly, 2012).

With all the wealth of theoretical knowledge on the topic of EFC, industrial applications have been faced with challenges which have resulted in numerous studies aimed at increasing the knowledge base and improving the applications of crystallization. The following section synthesises the investigations that have added to the knowledge foundations of the practical applications of crystallization.

3. Literature Review

The industrial implementation of EFC has been hampered by ice scaling on its HX surfaces. Scraping of the HX surfaces has been widely investigated to prevent and reduce ice scale formation. Studies on the heat transfer in crystallizers, the efficacy of scraping methods because of scraping speed and force, and the response of ice to scraping have been conducted to optimize the scraping process. These studies are reviewed in the first section of the literature. However, it became evident that minimal work has been done to understand the effect of HX surface properties on ice scaling in EFC. Therefore, the second section focuses on studies that illustrate the effect of HX surface properties on ice scaling. Various researchers have studied the mechanisms of ice scale formation at the interface, and the effects of materials surface free energy and topography on the accumulation of ice onto a surface. This knowledge could be assimilated into EFC, to potentially improve the efficiency of ice scale reduction in the eutectic freeze crystallization of brines.

3.1. Eutectic freeze crystallization

In EFC, brine solutions have been processed to recover salts and ice from solutions. Researchers such as Himawan et al. (2006) have demonstrated $MgSO_4{\cdot}7H_20$ recovery in a eutectic system, while Reddy et al. (2010) recovered $Na_2SO_4{\cdot}10H_20$ in a 4 wt% solution with impurities. Later, Aspeling (2019) managed to selectively recover these salts in a multicomponent solution which is typical of industrial brines. In order to operate these recovery processes optimally, Randall and Nathoo (2015) suggested that the feed stream into the EFC process needed to be concentrated as close to its eutectic point as possible. However, industrial brines can be dilute yet supersaturated with sparingly soluble salts, and these brines may vary in their composition. A varying feed composition introduces difficulties in process control and scale prevention. Moreover, the dilute brines, and the presence of the sparingly soluble salts, increase the scaling potential on the HX surface upon cooling. As a result, the successful processing of multicomponent brines is challenged by scaling of the HX surface.

Scaling poses a major drawback in the industrial implementation of EFC, as it reduces the process efficiency due to the overall drop in heat transfer rates, which results in low product recoveries (Vaessen et al., 2002). Scaling increases the energy consumption within the process, which raises the production costs (Sheikholeslami, 2004). This increase in energy consumption is needed to partially restore the initial product/energy ratio required for an efficient process (Sheikholeslami, 2004). Therefore, significant investments have been made to mitigate scaling in EFC and improve the overall process efficiency. Consequently, most EFC crystallizers are fitted with scrapers to reduce scaling on HX surfaces and to a lesser extent, direct cooling has been used to avoid scaling that is inherent to HX surfaces.

The most obvious method to avoid scaling on HX surfaces would be to eliminate the presence of the cooled surface. In EFC, this has been achieved using direct cooling. Examples of direct cooling methods include the Crystalex^{TM} process (Stepakoff et al., 1974). It involves direct contact crystallization and pressurized counter wash water (Stepakoff et al., 1974). Freon refrigerant R114 is used and is non-toxic, non-flammable, and allows operation near atmospheric temperatures (Stepakoff et al., 1974). The disadvantage of this configuration is that the solid products become contaminated by the refrigerant. Most recently, Hasan et al. (2017) investigated the recovery of $NaSO_4.10H_2O$ from aqueous solutions using EFC, by air cooling of static layer growth. This method of cooling was also limited due to the contamination by salt molecules retained in the inclusions of the ice layer.

3.1.1. Scale mitigation by scraped crystallizers

Since the development of the direct cooling method is still ongoing, most researchers have focused on the improvement of scrapers used in the indirectly cooled crystallizers. The use of scrapers in reducing ice scaling has been widely investigated, with a focus on improving scraper and crystallizer designs to reduce scaling and enhancing heat transfer within the crystallizing unit (Vaessen et al., 2004; Genceli, Trambitas, et al., 2005; Pronk et al., 2008; Rodriguez Pascual et al., 2010).

3.1.1.1. Heat transfer in scraped crystallizers

Heat transfer rate is one of the most critical design parameters of EFC crystallizers, as it directly determines the attainable level of supersaturation, which reduces the production rate and separation efficiency of the system (Vaessen et al., 2004; Genceli et al., 2005; Himawan et al., 2006). Increasing the supersaturation can result in the formation of ice scale at the HX surface, because of the supersaturation is highest near the HX plate (*Figure 3.1*).

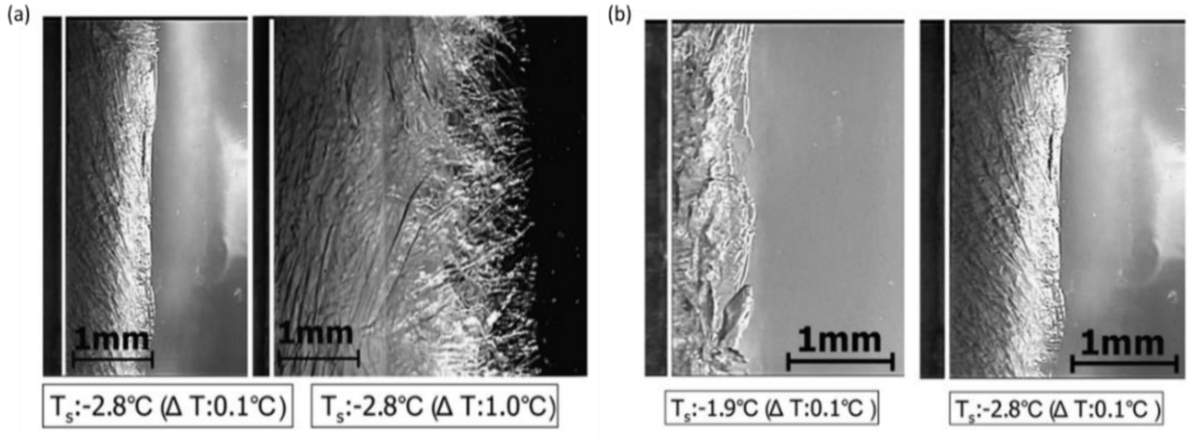

***Figure 3.1**: Enlarged photographs of the side view of the ice scale at similar surface temperatures and different supersaturations (a). Photographs of ice scale at different surface temperatures and similar supersaturations (b). Source:* Matsumoto et al. (2010).

The formed ice scale layer results in differences in its growing structures depending on the bulk supersaturation. According to Matsumoto et al. (2010), a high bulk supersaturation results in a dendritic ice scale layer at the ice scale-bulk solution interface, with a sparse structure at the HX surface. At the same time, a lower bulk supersaturation results in a smooth ice scale layer that is dense in structure (*Figure 3.1(a)).* In the case of similar bulk supersaturations, a lower surface temperature resulted in a smooth surface at the ice-bulk solution interface, with a dense structure at eh HX surface (*Figure 3.1(b))*. At a higher surface temperature, ice was uneven, and the ice structure near the HX surface seemed sparse.

Since the thermal conductivity of ice is 10 - 20 times less than that of the stainless steel used in most crystallizers, heat transfer is reduced when ice scaling occurs (Vaessen et al., 2002). As a result, ice scale increases the resistance to heat transfer at the HX surface, leading to a stagnation of the crystallization process. Scrapers have been widely used to prevent this stagnation of the crystallization process due to scaling. Work conducted by Leyland et al. (2019), showed that scrapers prevented ice accumulation onto the HX surface by increasing the scraping rotational speed, which increases the distribution of supersaturation in the bulk solution. This work is supported by Vaessen et al. (2002), who mentioned that the purpose of scrapers is to provide continuous replenishment of the thermal boundary layer. Therefore, this scraper action enhanced heat transfer between the wall and the surrounding fluid.

Heat transfer during crystallization has been studied in scraped surface heat exchangers (SSHE). Numerous authors have agreed that heat transfer was significantly improved by increasing scraper rotational speed (De Goede and De Jong, 1992; Crespí-Llorens et al., 2013). De Goede and De Jong (1992) and Crespí-Llorens et al. (2013) suggested that this was due to increased turbulence produced in the flowing fluid, as well as the generation of vortices, which improved the heat transfer in the system. Moreover, numerical studies by Dehkordi et al. (2015) indicated that the scraper RPM in SSHE increased the heat transfer performance more than changes in the scraper shape and the number of scraper blades. These studies indicated that the hydrodynamics created by the scrapers affected the thermodynamics at the interface, in turn, impacted the crystallization process.

A study by Martínez et al. (2014) confirmed that increased scraping velocities increased heat transfer. The researchers investigated the action of two different scraper arrangements, one rigid and the other with adaptable scrapers pushed by torsion springs, on a scraped surface plate heat exchanger (SSPHE). Contrary to De Goede and De Jong (1992) and Crespí-Llorens et al. (2013), the study further emphasised that the effect of scraper speed on heat transfer was small compared to the scraper system used. This result highlighted that the adaptable scrapers improved the heat transfer coefficient and the heat flux two-fold compared to the rigid scrapers on an SS316 HX surface. This was a key finding as it indirectly emphasised that the efficiency of mitigating ice scale was not only a function of scraper velocity and scraper design but also dependent on the ability of the scraper to follow the HX surface topography. Therefore, surface topography is vital in controlling ice scaling.

Heat transfer in cooled disk column crystallizers (CDCC-1 and CDCC-2), and the scraped cooled wall crystallizer (SCWC-1 and SCWC-2) have been widely investigated. The efficiency of heat transfer in the cooled disk column crystallizer (CDCC-1) and scraped wall cooling crystallizer (SCWC-1), with HX surfaces constructed from SS316 were investigated by Vaessen et al. (2004). Both crystallizers were fitted with *polytetrafluoroethylene* (PTFE) scrapers of different geometries. The heat transfer rate was enhanced up to 7.2 kW.m^{-2} with increasing scraping rate in the CDCC-1. In addition, the height of the CDCC-1 scrapers increased the mixing of the ice slurry produced, which contributed to the efficiency in heat transfer.

In contrast, the wing-shaped SCWC-1 was not as efficient as the CDCC-1 in mixing the ice slurry produced (Vaessen et al., 2003; Vaessen et al., 2004). Consequently, the increase in ice content of the crystallizer dominated the scraper speed, thereby decreasing the process-side heat transfer at higher temperature difference and scraping rates. This observation was contrary to general expectations, where higher rotational speeds led to better mixing and therefore higher heat transfer rates. The use of wing-like scrapers resulted in the presence of an insulating ice layer at the HX surface. It highlighted the limitation of scraper design in improving heat transfer during crystallization.

Genceli et al. (2005) studied the CDCC-2 to optimize the scraper-HX plate system. The HX plate was made from SS316, and the four rotating scrapers were made of high-molecular-weight- *polyethene* (HMPE). The researchers found that by lowering the coolant temperature from -7.6 to -11.7°C the heat flux increased from 2.61 to 5.75 kW.m^{-2} under the same operating conditions used by Vaessen et al. (2002), where the SCWC heat flux was 0.9 - 2.5 kW.m$^{-2,}$ and the CDCC-1 was 2.5 kW.m^{-2} in the best case. This was due to the increased volume, from 110 ℓ in CDCC-1 to 150 ℓ used in the CDCC-2. The larger crystallizer volume provided a larger cooling area (5.6 m^{3}m^{-2}). This larger cooling area enhanced the heat flux while preventing ice scaling by using the maximum scraping speed.

3.1.1.2. Scraper speed for ice scale removal

In addition to continuously replenishing the thermal boundary layer, scraping speed is an essential parameter in the efficient mechanical removal of scaled ice from the HX surface. For efficient scale prevention and control in a fluidised bed, Pronk et al. (2008) deduced that the rate for ice removal had to be faster than the rate of ice accumulation on the HX surface. This statement was corroborated by a study conducted by Leyland et al. (2019), who found that the scaling induction time (the period between bulk nucleation and ice scale layer formation) increased with scraper speed. This showed that the increasing scraping speed reduced the accumulation of ice on to the HX surface.

Vaessen et al. (2002) investigated the scraping rates required to keep the SS316 HX surface free of ice. The induction time was measured by determining the minimum scraping rate required to keep the heat transfer surface free of an ice layer (Vaessen et al., 2002). The study found that the required scraping rate for ice removal increased with increasing supersaturation. A study by Matsumoto et al. (2010), agreed with these findings, and the scraping rate required to remove ice on a carbon steel HX surface was also found to increase with a drop in the HX surface temperature. This indicated that higher supersaturations (ΔT) at the HX surface resulted in shorter scaling induction time, which required faster scraping rates. In the industry, the faster scraping rates are a cause of major mechanical breakdowns in the crystallizing process, which reduces the process efficiency.

Even with the increased probability of mechanical breakdown, both studies found that increasing the scraping rate did not completely remove the ice layer from the SS316 HX surface. Vaessen et al. (2002) mentioned that this was due to the thin ice layer that was always present on the metal surface during scraping. Work by Matsumoto et al. (2010) practically demonstrated this phenomenon using a carbon steel HX surface. In this work, the scraper force increased with an increase in the number of scrapings. This relationship was a result of several surviving ice islands on the carbon steel surface, which increased after every scraping. The surviving ice was due to scraping occurring elsewhere than the ice-HX interface, due to the uneven surface topography. Martínez et al. (2014) has attributed this to rigid scrapers which were unable to follow the SS316 HX surface topography, so a continuous layer developed during crystallization. Therefore, after scraping, ice grew on the surviving ice islands as well as on the HX surface. In turn, the scraping force increased with the number of scrapings as the ice layer continued to crystallize with time.

3.1.1.3. Scraper force for ice scale removal

When an ice scale layer has been in contact with the HX surface for an extended amount of time, the required force for its removal increases (*Figure 3.2(a)*). The thin ice layer persists because of localised supersaturated regions created by uneven surface topography. Moreover, uneven surfaces play a role in increasing the adhesion strength of the scaled ice, as shown in *Figure 3.2 (b)*.

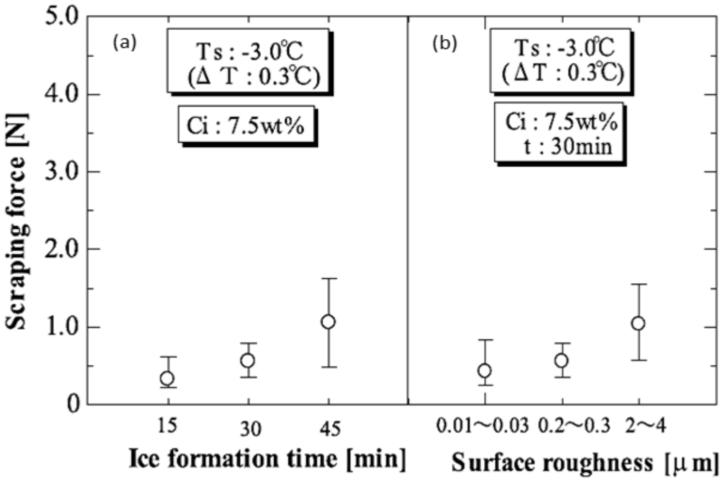

Figure 3.2*: The effect of ice formation time (a), and surface roughness(b) on the scraping force. Source:* Matsumoto et al. (2010).

Matsumoto et al. (2010) found that rougher surfaces required a higher scraping force because of the larger ice-HX surface contact area (Matsumoto et al., 2010). The larger surface area increased the interfacial contact area, and, as a result, the interfacial tension between the ice and HX surface strengthened. However, Martínez et al. (2014) showed that adaptable scrapers were able to move along the surface contours, preventing the ice layer from developing. Therefore, it is evident that rigid scrapers could prevent the continued growth of the ice scale layer but were incapable of completely removing ice once it had formed on an uneven surface. Although Martínez et al. (2014) did not investigate the effect on scraping force, the swift removal of ice by adaptable scrapers would have reduced the ice-HX surface contact time, thus reducing the requirement for greater scraping force, as shown by Matsumoto et al. (2010).

Uneven surfaces have been shown to allow residual ice crystals to remain after scraping, providing a site for continued ice scale growth. Vaessen et al. (2004) found that the observed decrease in the heat transfer coefficient with the slower scraping rate was due to an insulating layer resulting from inefficient ice removal by scrapers. This observation was explained by the work conducted by Matsumoto et al. (2010), who stated that even with more scrapings, fragments of ice remained with each scrape, resulting in an insulating ice layer. Martínez et al. (2014) explained that the accumulation of ice fragments was a result of the HX surface topography, which allowed for quiescent regions of local supersaturation and adhesion of ice. This study indicated that the rigid scrapers, such as those used in the studies by Vaessen et al. (2004) and Matsumoto et al. (2010), were not able to follow the surface topography, and led to continued ice scaling. These studies indicated that it would be beneficial to use an HX surface that minimised the conditions which were conducive to ice scaling, in order to avoid the persistence of the thin ice scale layer and ultimately improve the efficiency of scraping.

3.1.1.4. Adhesive and cohesive breaks of ice scale as a result of scraping

When the persistent ice scale layer is scraped, the ice tends to break off from the HX surface. A study by Matsumoto et al. (2010) has indicated that scraping of the persistent ice scale layer has resulted in cohesive breaks, adhesive breaks, or both. *Figure 3.3* (*A*) shows the scraping of ice through adhesive breaks, while *Figure 3.3* (*B*) shows ice scale removal through cohesive breaks. The applied scraping force indicated the cohesive and adhesive strength of the scalant onto the HX surface. The cohesive strength depended on the supersaturation at the HX surface and solution properties and the structure of the ice layer. The adhesive strength depended on the HX surface temperature and the HX surface properties, such as surface free energy and topography.

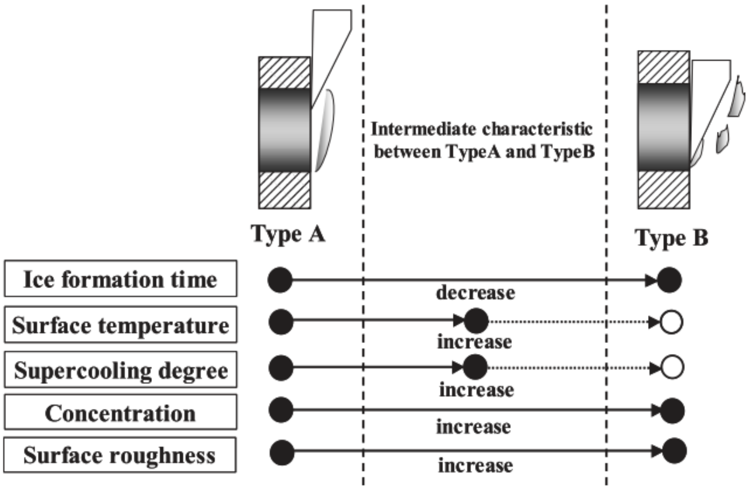

***Figure 3.3**: Scraping resulting in adhesive breaks (A) and cohesive breaks (B). Source:* Matsumoto et al. (2010).

Matsumoto et al. (2010) found that Adhesive breaks occurred when the ice formation time was longer, and the surface temperature, degree of supersaturation and solution concentration were low. The ice removal that was caused by adhesive breaks (Type A) had and dense structure (due to higher cohesive forces) (Matsumoto et al., 2010). However, when the ice formation time was shorter, and the solution concentration high, cohesive breaks occurred (Type B). This form of ice breakage was because of the sparse structure of ice, which made it softer and susceptible to cohesive breaks.

A smoother topography was found to result in adhesive breaks, while a rough topography led to cohesive breaks. This observation highlighted the effect of surface topography on the ice scale layer formed, and the resulting behaviour of ice upon scraping. In these studies, SS316 and carbon steel were used as HX materials. These materials have inherently uneven surface topographies, meaning that~~,~~ scraping ice from their surfaces resulted in residual fragments of ice on the HX surface.

It is essential to highlight that adhesion was also dependent on the surface free energy of the HX material, as indicated by the work of adhesion (W_A). The effect of this surface property on scaling or scraper efficiency has not been explored in EFC, leaving a gap in the attempt to solve the scaling problem. Continued use of HX surfaces that promote ice scaling is counterproductive to solving the scaling problem. Since HX materials are prone to ice scaling, it would be advantageous to use a material that would result in clean adhesive breaks when removing the ice scale and so avoid residual ice on the HX surface.

3.2. Effect of surface properties on ice scaling

Crystallizers provide surfaces which may be constructed of various materials on which scaling may occur. In industry, surfaces like mixing blades, scrapers, pipelines, and the heat exchanger (HX) wall reduce the free enthalpy for nucleation (ΔG_{crit}), resulting in crystallization on to these surfaces. Because these surfaces have properties that are conducive to scaling, it would be useful to investigate these inherent properties, to understand better the extent of their contribution to the scaling process. Therefore, this section focuses on the surface free energy and surface topography of HX materials, as they directly affect the scaling process through heterogeneous nucleation and adhesion. As an introduction, the first section delves into understanding the solid-bulk solution interactions at the interface, as it is the first step towards scaling at cryogenic temperatures.

3.2.1. Crystallization at the interface

Although it is known that solid-liquid interfacial area is a strong function of the solid surface chemistry, topography and supersaturation near this surface, to understand of the solid-liquid interface in the molecular scale under continuous operational conditions has proved to be very challenging, even when using both experimental and theoretical methods (Alizadeh et al., 2012; Björneholm et al., 2016). This is because the knowledge of the physical chemistry of the liquid-solid interface is still minimal due to the intrinsic complexities when investigating this interface. Similarly, the extent to which the interface can be practically investigated is also limited (Björneholm et al., 2016). This limitation makes the study of the scaling process very complex as it is dependent on theoretical knowledge.

According to Hodgson and Haq (2009), water adsorption at the interface with the metal surface is governed by a subtle balance between water-water hydrogen bonding, and water-metal electrostatic and charge-transfer interactions. Together, these interactions determine the stability and ordering of the water structures formed at the interface, and the interactions are a function of the surface free energy of solid surface materials and the water cluster surface tension.

In their study of molecular behaviour at the interface, Meng et al. (2004), found that isolated monomers and small clusters may form 1D chains, which can form dimers to hexamers of water molecules, that grow into multi 2D ordered layers of ice. Further research in this field led Verdaguer et al. (2006) and Hodgson and Haq (2009) to propose that these clusters existed on metal surfaces at cryogenic temperatures, based on experimental results obtained when using the Vibrational Spectroscopy and Scanning Tunnelling Microscopy. Alizadeh et al., 2012, hypothesised that these cryogenic temperatures increased the hydrogen bond lifetime, resulting in stable hydrogen-bonded clusters near the surface. This was indicative of the increase in viscosity of the solution in colder regions.

Verdaguer et al. (2006), stated that the hydrogen-bonded molecular clusters become kinetically stable and thermodynamically metastable. Once they reached a minimum of approximately 100 molecules, the molecular ice clusters became critical nuclei (Mullin, 2001; Yang and Dai, 2003). In a study using molecular simulations, Lupi and Molinero (2014) found that subcritical ice molecular clusters containing less than 100 water molecules formed throughout a droplet volume during the induction period. However, critical nuclei formed only at the graphite surface, which indicated that wetting by ice was consistent with a stabilization of the subcritical ice nuclei by the surface. Therefore, the study showed that the presence of a foreign surface promoted the heterogeneous nucleation of ice clusters that would otherwise be subcritical in the absence of the foreign surface.

Water in a bulk system tended to order itself into pre-ordered bilayers near this foreign HX surface. A study by Lupi et al. (2016), showed that within bulk water, wetting of a critical ice nucleus by the pre-ordered bilayer hexagons decreased the nucleation barrier, resulting in the increase in nucleation rates. This conclusion arose from observing the higher propensity of water to crystallize into ice at the surface, where the water became more organized than in bulk, as shown in *Figure 3.4*:

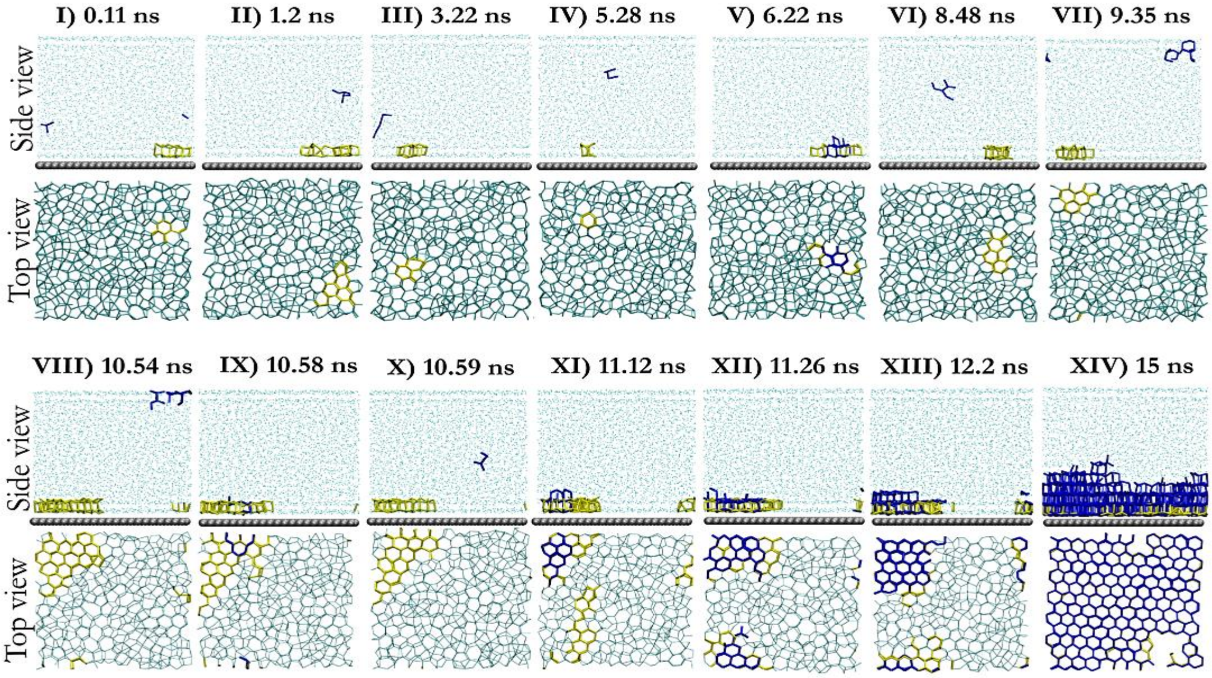

Figure 3.4: *Using molecular simulations with mW water model, snapshots along a crystallization trajectory of water in contact with a graphitic surface at 218 K and 1 bar show the formation of patches of bilayer hexagons preceding ice nucleation. Liquid water is represented in cyan, ice in blue, and bilayer hexagons in yellow. The side and top view of the cell are shown for each time along the trajectory. The top view displays only water within 8 Å from the carbon surface (i.e., the first two layers) Source:* Lupi et al. (2014).

Lupi et al. (2014), observed that the pre-ordering of the water bilayer near a surface increased with supersaturation. *Figure 3.4* indicates that the number and size of the pre-ordered bilayer clusters increase with time, even though they were continuously created and destroyed. Némethy and Scheeaga (1962), theorised that this happened because the clusters of bilayers arose from local energy fluctuations, which affected molecules that were near each other during the induction period. For this reason, Lupi et al. (2014), explained that crystallization was preceded by the formation of a large, long-lived patch of bilayer hexagons, where the crystalline nucleus was born. Using further Committor analysis, Lupi et al. (2016), indicated that changes in the size of the bilayer patches occurred too early to decide the transformation from liquid to ice. Therefore, the size of the hexagonal ice crystal nucleus was what described the transition state that separated the liquid from the ice, as presented by the critical radius (r_{crit}) of the classical nucleation theory.

Lupi et al. (2016) measured the size of the hexagonal ice crystal nucleus by using the radii of gyration. Within the pre-ordered bilayer, the size distribution of the radii of gyration R_g of critical ice nuclei was found to peak at 12 Å, close to R_g of 13 Å characteristic of a hemispherical ice cluster with the same number of water molecules. These formations are represented in *Figure 3.5 (a)* and *(b)*, where one transition state arrangement is more hemispherical, and the other is flatter, with better-defined faceting of crystallite.

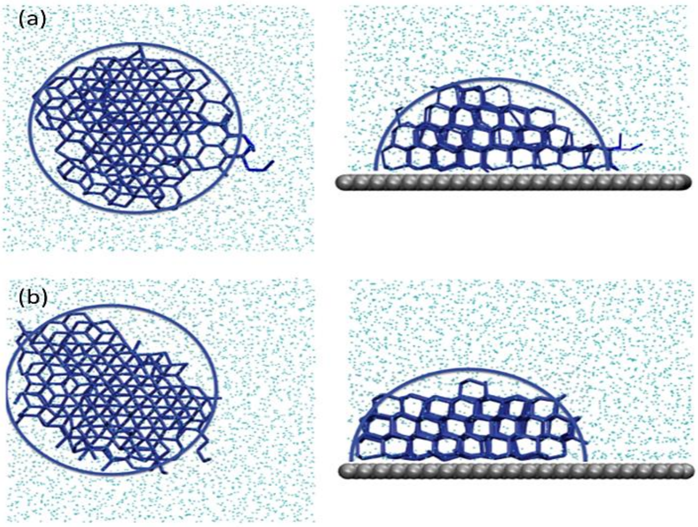

***Figure 3.5**: Top and lateral views of the radius of gyration R_g for the transition state arrangement of the critical crystalline nuclei, where (a) represents R_g =12 Å and (b) represents R_g =13 Å. Source:* Lupi et al. (2016).

The authors concluded that the shape represented in *Figure 3.5* indicated that the preferential pathway to crystallization passed through spherical cap nuclei, the shape proposed by classical nucleation theory. The wettability of these critical nuclei determined the growth mode of the islands that formed on the surface. Using atomistic molecular dynamics simulation analysis, Liu et al. (2017), attributed distinct ice growth phenomena to the presence or absence of the pre-ordered bilayer. Critical nuclei with a high contact angle *Figure 3.6 (a-b)* were found to undergo an off-surface growth mode, while the critical nucleus exhibited a low contact angle, *Figure 3.6 (c-d)*, underwent growth mode which occurred along the surface.

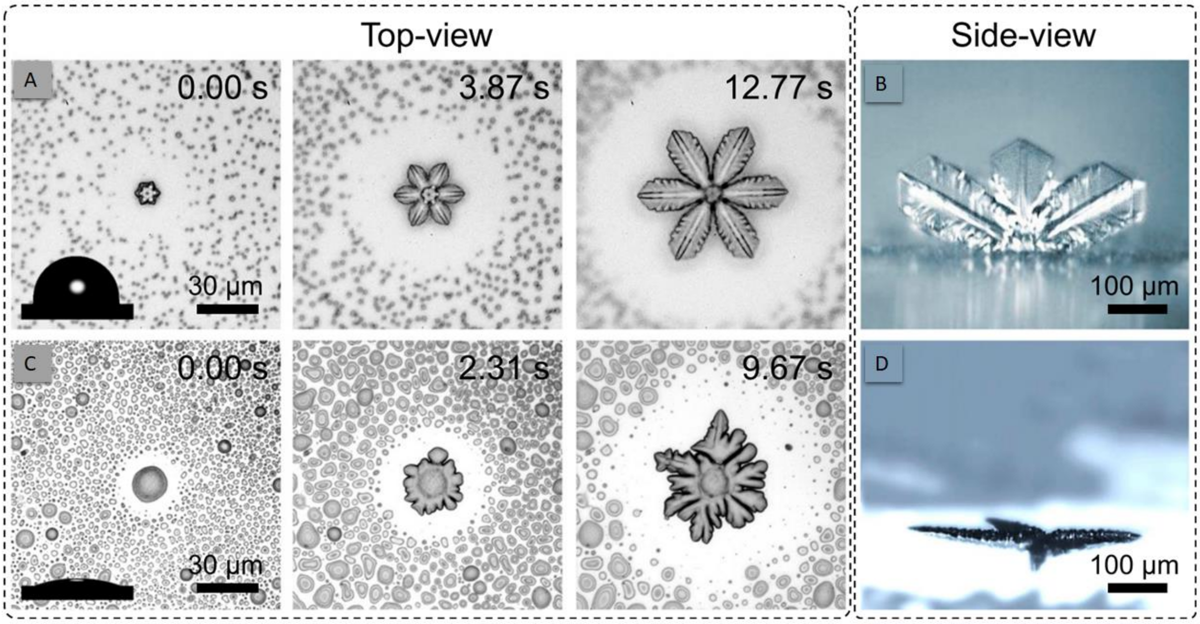

***Figure 3.6:** Two ice growth modes of a droplet with a contact angle ϑ=107.3° (A and B) and ϑ=14.5° (C and D), at a surface temperature -15°C. Source: Liu et al. (2017).*

Thürmer and Bartelt (2008), observed that these ice islands grew horizontally across the surface until they merged or encountered a substrate step *Figure 3.7 (a)*. The crystals merged if their bilayer staking matched *Figure 3.7 (b)*; otherwise, they formed a domain boundary (db) as indicated in *Figure 3.7 (c)*:

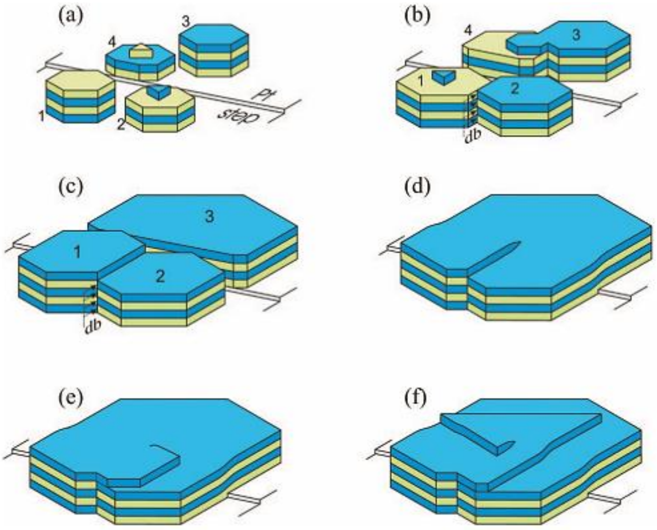

Figure 3.7: *Scenario summarising the key process leading to the growth of cubic ice. Source:* Thürmer and Bartelt (2008).

This study described how layers bent upwards or downwards to join layers of equal intralayer stacking across a substrate step, producing a screw dislocation *Figure 3.7 (d)*. After overgrowing the domain boundary, the top layer easily expanded and formed a growth spiral *Figure 3.7 (e-f)*. These domain boundaries might also occur because the topography of the surface provided a step, which could also produce screw dislocations. Ultimately, these screw dislocations expanded to form a spiral which determined the surface morphology of the growing ice layer.

Rahimi et al. (2015) investigated the growing ice layer and indicated that flat hydrophobic surfaces exhibited slower ice growth and denser ice layers. This investigation revealed the initial growth process normal to the HX surface. The finding was of paramount importance, as the observed structure and morphology of this layer determined the adhesion and cohesion strength of the ice-scale layer which ultimately served as a substrate for the adhesion of any other ice crystals, and thus enhanced the growth rate of the ice scale. Both Kapembwa et al. (2014) and Rahimi et al. (2015), reported that once the ice scale had completely covered the heat exchanger surface, the scaling was affected by the bulk supersaturation. It is therefore important to understand the effect of the HX surface free energy and topography on the nucleation and growth process before the ice scale reaches this point.

3.2.2. Effect of the surface free energy of a solid surface on crystallization

In their study of the effect of surface free energy on crystallization, Abdelmonem et al. (2015) found that surfaces with different properties influence the scaling process differently. They found that surfaces such as sapphire have no influence on the water structure at its surface as it cooled down to the point of freezing, while mica and graphite surfaces tended to induce local ordering of the water bilayer, which facilitated heterogeneous ice nucleation. Therefore, from these experimental observations, it may be possible to hypothesise that the surface chemistry of an HX surface plays a vital role in facilitating the initiation of heterogeneous nucleation of the scalant.

Researchers have found that the scalant also has unique surface chemistry which results in surface charges (electrostatic forces). Vaessen et al. (2002), considered the existence of these surface charges on the scaling agent to be an additional cause of scaling in EFC. These surface charges influence the wetting of ice nuclei on an HX surface, as did the environment created by the surface energy of the HX surface. The writers investigated the effect of surface free energy of materials on scale formation to reduce both ice and salt scaling. They concluded that this effect was due to the ability of materials of low surface energy to reduce the wetting of the crystallizing material on the HX surface, hence increasing the overall ΔG_{crit} to be overcome for heterogeneous nucleation.

Carpenter and Bahadur (2015) and Sojoudi et al. (2016) concluded from their investigations that the surface chemistry of a material of low surface free energy tended to increase the ΔG_{crit} for ice heterogeneous nucleation due to its icephobic (anti-icing) nature. Chemically, fluorine is known to be effective in lowering surface free energy, resulting in hydrophobic surfaces. Nishino et al. (1999), explained that this happened because fluorine had a small atomic radius and the largest electronegativity among atoms, forming a stable covalent bond with carbon. After conducting wettability studies, Hare et al. (1954), reported that the surface free energy decreased with an increase in the number of exposed *polytetrafluoroethylenes* (PTFE) $-CF_2-$ groups. In addition, Seo and Mani (2016), referred to these surfaces as superhydrophobic as they consisted of micro-scale roughness elements in addition to their hydrophobicity. These superhydrophobic surfaces presented a high icephobic potential in the initial stages of ice formation due to their ability to reduce hydrodynamic drag significantly. They found that drag reduction was achieved by accommodating large slip velocity near the surface due to entrapment of air bubbles, which reduced the fluid surface contact time.

Carpenter and Bahadur (2015) theorised that these low-surface energy materials could reduce ice scaling by delaying heterogeneous ice nucleation and by reducing ice-surface adhesion. However, Yin et al. (2010), argued that none of the surfaces could completely prevent the formation of ice scale, even though they had a high icephobic potential in the initial stage of ice scaling. These findings were based on the assumption that the solid-water and solid-ice interaction mechanisms were similar, as water and ice are both polar (Dotan et al., 2009). Therefore, it is important to review the effect of surface free energy on the supersaturation at nucleation, drag reduction, scaling induction time and adhesion, in order to establish the possibilities for reducing the formation of the initial ice scale layer, which has been one of the main issues faced in the industrial operation of the scraped EFC crystallizer.

3.2.2.1. Effect of surface free energy on the required supersaturation for nucleation

Studies have shown that a higher supersaturation is required for the onset of nucleation, as the surface free energy of the surface decreases. Qin et al. (2003) found that the probability of nucleation at the interface increased with the supersaturation as a result of the cooling rate. Yin et al. (2010) stated that this increase in probability occurred because the contact angle of ice nuclei decreased with the surface temperature, indicating that the wetting by a nucleus increased as the supersaturation level at the HX surface increased.

Using single water droplet impact studies, Alizadeh et al. (2012) investigated ice nucleation on surfaces of various surface energies. They found that the reduced wettability of superhydrophobic surfaces played a dual role in delaying ice nucleation by reducing both the heat transfer and drag. As a result of the reduced heat transfer, nucleation occurred at lower supersaturations. A similar finding, reported by Lv and Zhang (2016), was that the heat transfer rate was suppressed by the air cavities on superhydrophobic surfaces.

Using the similar droplet impact method, Carpenter and Bahadur (2015), compared the effect of the surface energy of materials on ice scaling in a brine solution using both a PTFE HX surface and a bare aluminium surface. They found that the brine solution was able to reach higher supersaturations prior to scaling with the PTFE HX surface than with the bare aluminium plate. The decrease in heterogenous nucleation temperature could have been due to the use of a brine solution instead of pure water, which resulted in a lower freeze point. However, the study by Yin et al. (2010), using deionised, water corroborated both studies, indicating that the attained supersaturation was lower on a hydrophobic surface than on a superhydrophobic surface, as shown in *Figure 3.8*.

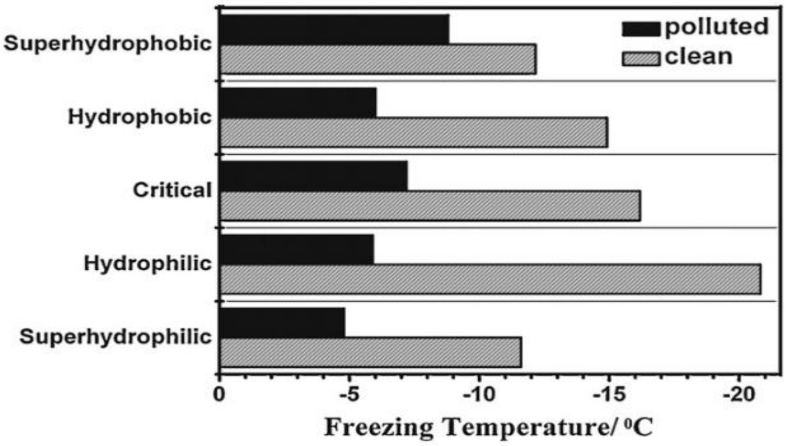

Figure 3.8*: Freezing temperature of supercooled deionised water on surfaces of differing surface free energies. Source: Yin et al. (2010).*

These findings showed that superhydrophobic surfaces might reduce heat transfer rates within the system. However, after the inception of ice scaling, the superhydrophobic surface retained the lowest supersaturations temperature of all samples used, indicating a delay in the formation of an insulating ice scale layer. The reduced interfacial tension by hydrophobic surfaces resulted in a reduction in the solution-surface drag, which in turn resulted in lower freezing temperatures than on superhydrophobic surfaces.

3.2.2.2. Effect of surface energy on drag reduction at the interface

Work conducted by Tourkine et al. (2009) used an inclined plane to investigate the nucleation of ice from a water droplet. The study found that droplets moved quickly from a cooled superhydrophobic copper surface without freezing, while the droplets moved slowly on the normal copper plate, leaving a thick trail which ultimately crystallized. This work indicated that using a modified surface with lower surface free energy decreased the contact between the HX material and solution at the interface, by reducing the frictional drag on the water droplet, which contributed to the delay in the onset of scaling when a fluid is in motion. The study by Alizadeh et al. (2012) corroborated these findings, by also using the single water droplet impact studies to investigate ice nucleation on surfaces of various surface energies. They found that the reduction of water-surface wettability on the superhydrophobic surfaces delayed the onset of ice nucleation, by reducing the drag at the interface.

The frictional drag of a surface was investigated comparing an aluminium disc with TiO_2 superhydrophobic nano-coating and one of smooth uncoated aluminium. This study by Moaven et al. (2013) indicated that the coated surface was able to reduce the viscous drag of a solution of ethanol, titanium butoxide, deionized water, and diethanolamine by 30% in laminar flows and 15% in turbulent flows respectively. They postulated that the result was due to the trapping of air pockets in between the micro/nano regions or the smaller contact area between the droplet solution and the solid surface. Although it was difficult to maintain the pockets of air trapped at the interface at highly turbulent interfaces, the shorter contact time between flowing bulk solution and the surface might still delay the onset of scaling on superhydrophobic surfaces.

The consequences of the drag reduction are illustrated in work conducted by Yang et al. (2002). They found that at fixed heat flux, low energy surfaces prolonged the induction period of scaling in cooling systems, unlike high surface energy material like copper. This was because the induction period increases with an increased in fluid velocity at the interface, which delayed the onset of heterogeneous nucleation. A later study by Lv and Zhang (2016) investigated drag reduction of water flowing through tubes with a superhydrophobic surface at a macro scale. The drag reduction ranged from 8.3% and 17.8% at Reynolds numbers ranging from 3000 to 11000. Thus, the interplay between fluid dynamics and HX surface properties at the interface played a crucial role in reducing the drag, which might increase the scaling induction time of a system.

3.2.2.3. Effect of surface properties of the scaling induction time

Anti-scaling surfaces are developed to increase the induction time of a process. In general, the scaling induction time is the time taken for water to freeze after attaining supersaturation, although various authors may define this period differently. In their study of scaling induction time, Alizadeh et al. (2012) found that at low temperatures, the water-substrate interfacial area varied by almost 2 orders of magnitude when comparing the hydrophilic and superhydrophobic surfaces. This difference resulted in extended scaling induction times when the hydrophobic and superhydrophobic surfaces were used, as shown by the temperature jumps in *Figure 3.9.*

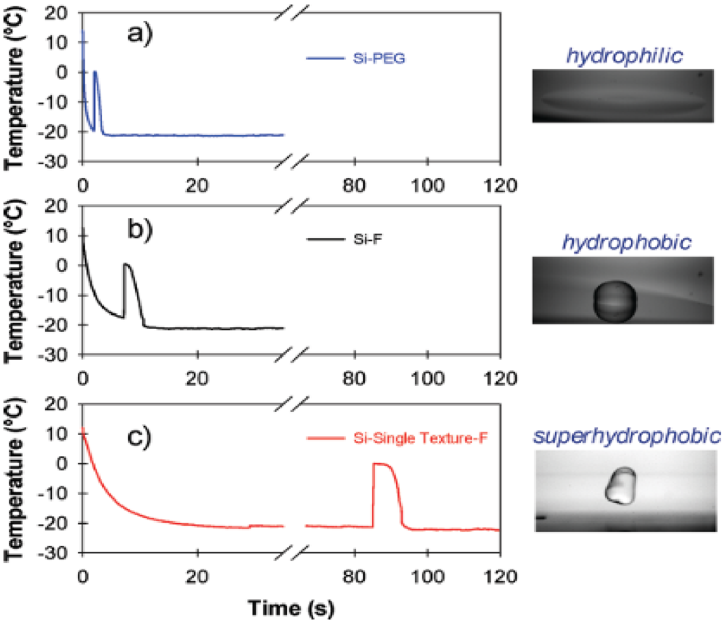

Figure 3.9: *Transient temperatures of 4μℓ deionised water droplet freezing on a hydrophilic, hydrophobic and superhydrophobic surface at a surface temperature of -20°C. Source: Alizadeh et al. (2012).*

Alizadeh et al. (2012) observed the time scale for both heat transfer and heterogenous nucleation was a function of the surface hydrophilicity, as indicated by *Figure 3.9.* Rapid cooling was observed when using a hydrophilic surface, resulting in the start of nucleation while the water droplet was still cooling. Cooling on a hydrophobic surface reduced heat transfer and the induction time was prolonged but freezing still occurred during the cooling stage. The nanostructured superhydrophobic surface produced the longest induction times. This result was attributed to the insulating properties of the surface, the reduction in liquid-solid interfacial area and the increased energy barrier to forming a critical nucleus at the interface.

Qin et al. (2003), further compared the effect of surface free energy on heterogeneous ice nucleation using a stainless-steel plate suspended in a jacketed crystallizer. The plate was submerged in a continuously mixed sugar 10 % (w/w) solution. The scaling induction time was defined as the time required to scale the entire cooling surface, thus indicating the scaling rate. They found that the Teflon coated cooling plate had a longer scaling induction time, a lower nucleation temperature, and delayed ice scaling. The investigators found that spontaneous ice nucleation occurred between -2.5 °C to -3.8 °C, and the onset of nucleation seemed to happen a random interval after entering the subcooling regions. Even though the researchers found that the probability of nucleation increases as the temperature decreases, they postulated further that the time and location of the occurrence of the first nucleus was also affected by multiple other factors. These factors include solid particle concentration, cooling rate, agitation strength, and the interface properties of the solid, e.g., its roughness, heat conductivity and surface tension.

Förster and Bohnet (1999), investigated the effect of surface free energy on induction time by using several types of metals with different surface free energies, as shown in *Table 3.1.* Aspenes et al. (2008), and Ozbay and Erbil (2016), found the aluminium surface to have a lower surface free energy than stainless steel unlike the findings by Förster and Bohnet (1999), although they agreed on the surface free energies of copper and brass surfaces.

Table 3.1: *Effect of surface free energy and roughness on induction time of calcium sulphate fouling. Source: Förster and Bohnet (1999)*

Material	Surface Free Energy ($mN.m^{-1}$)	Mean Roughness (µm)	Induction Time (h)
Copper	50	1	28.7
Aluminium	48	1	50.4
Steel	40	5	139
Brass	35	1	177
Polytetrafluoroethylene	18	11	89

The surface free energy values were found using the Drop Shape Analysis technique, and the harmonic mean method. The data *Table 3.1* indicates that the surface free energy of these materials influenced the inception of scale formation at a constant heat flux of 31.8 $kW.m^{-2}$. Förster and Bohnet (1999), found that the comparison of surface energy data with induction time yielded no correlation between interfacial solid-vapour interaction and scaling behaviour. The calcium sulphate induction time was shorter on PTFE than on brass and steel. They attributed these findings to the inherently rougher topography of PTFE. This result shows that a rougher surface increased that contact area between the crystallizing material and surface, and in turn, and it influenced the onset of heterogeneous nucleation.

Contrary to the opinions expressed in the studies above, Vaessen et al. (2002), held that materials did not affect the tendency for scaling but attributed the observed differences to the variation in supersaturation. However, as indicated by Yin et al. (2010), the level of supersaturation in the system may be influenced by the materials used. Therefore, the material may have influenced the tendency to scale, whether directly or indirectly. In addition to this argument, the use of HMPE scrapers by Vaessen et al. (2002), could have consistently influenced the environment at the interface, irrespective of the HX surface material. Therefore, this uncertainty about relative influences on scaling showed it was important to decouple the study of surface material from the influence of the scraper on the scaling process to understand how surface chemistry influenced ice scaling in the EFC process. The knowledge that scraper efficiency was dependent on the chemistry and topography of the HX surface material necessitated the separation of the two parameters.

3.2.2.4. Adhesion of ice at the interface

HX surfaces also influenced scaling through adhesion of the scaling agent at the interface. The adhesion strength is important as it determines the required force for ice scale removal. Matsumoto and Kobayashi (2007) investigated ice adhesion on to copper, vinyl chloride, and glass, all modified with plasma. They found that the shearing stress at the ice-solid interface was directly proportional to the solid surface energy, rather than to the cooling heat flux. Moreover, the adhesion energy was proportional to the material's surface energy. This finding showed that ice scaling on the material of lower surface free energy required reduced force to induce adhesive breaks from the HX surface. In a study conducted by Ozbay and Erbil (2016), ice adhesion on different materials of different surface free energies was studied by freezing water droplets at -30°C for 15 min, as seen in (*Figure 3.10*).

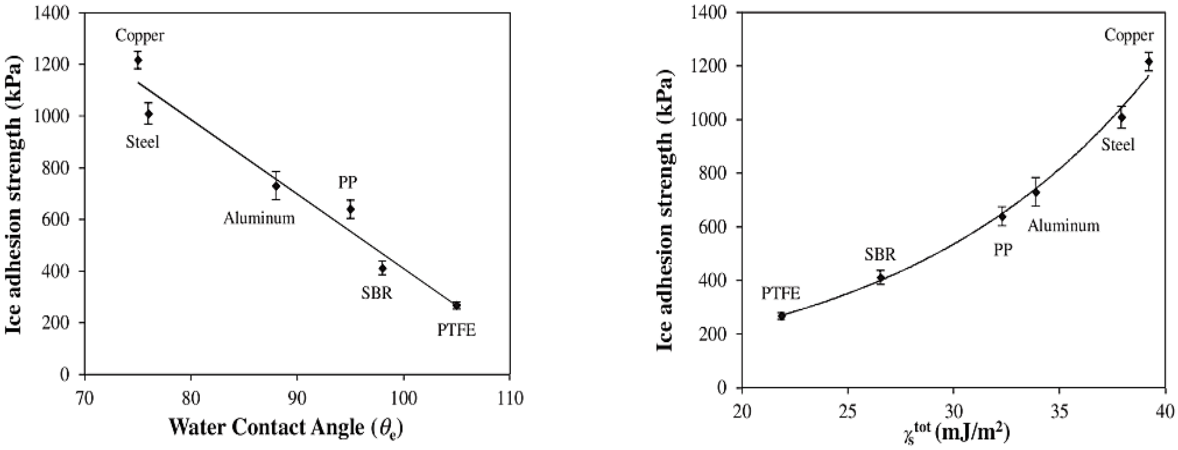

Figure 3.10: *Change of ice adhesion strength with the change in contact angle(a) and total surface free energies of the solid surfaces (b). Source:* Ozbay and Erbil (2016).

Figure 3.10 indicates that there is an inverse linear relationship between the contact angle and ice adhesion strength values, which decreased from 1217 to 268 kPa as the contact angle of the surfaces increased from 75° to 105°. In addition, the surface free energy has an important effect on the ice adhesion strength values, which increased from 268 to 1217 kPa with the increase of surface free energies from 21.8 to 39.2 $mJ.m^{-2}$ (Ozbay and Erbil, 2016). A study by Zou et al. (2011), confirmed that ice adhesion strength decreased with the increase in water contact angle, using the bare and modified aluminium samples. Therefore, these studies agree that using a material of lower surface free energy reduces the ice adhesion strength, with a hydrophobic material like PTFE showing the lowest adhesion strength.

Kulinich and Farzaneh (2009), found that ice adhesion strength on superhydrophobic surfaces was 5.7 times lower than that on the bare polished aluminium. In contrast, some researchers have reported that the use of superhydrophobic surfaces may not be beneficial in reducing the ice adhesion strength. However, the nanostructures on the superhydrophobic surfaces may be damaged during icing and removed during de-icing. Work conducted by Ensikat et al. (2009), found that this process can cause convex and concave regions on the surface, which increased the contact area of ice and the surface, which in turn increased ice adhesion. Bharathidasan et al. (2014), agreed with this hypothesis, as they observed adhesion reduction factors of 25-43 and 4.2-4.4 for hydrophobic and superhydrophobic surfaces, respectively, compared to bare aluminium.

In addition, Nosonovsky and Hejazi (2012), stated that the adhesion strength of the ice was dependent on the micro-cracks created at the solid-ice interface, making it a critical parameter governing the adhesion on to a low surface energy material. Therefore, if the low surface energy does not produce the microcracks, then the adhesion strength may be increased. Surface topography could be a contributing surface property to the formation of these microcracks, which might decrease the adhesion of the ice nuclei on the HX surface.

These findings indicated that ice adhesion was a function of both the surface chemistry and surface topography. Therefore, using smooth materials of low surface energy would be beneficial as a passive manner to reduce ice scale because, if ice scale occurred on an HX surface, its removal would require less force on a material of low surface free energy than on one of high surface free energy. Although the adhesion strength is not measured in this current work, it is important to know how it is affected by HX surfaces to assist in the interpretation of the results, and its potential influence in scraped crystallizers.

3.2.3. Effect of surface topography of the solid surface on crystallization

Material surface topography is important to ice scaling through heterogeneous nucleation and adhesion. Surface topography relates to the geometry of the HX surface. It may be composed of peaks (hills) or crevices (valleys), which describe the surface roughness, and waviness which describes the surface contour. All of these roughness parameters may affect the scaling process in different ways. Förster and Bohnet (1999), conducted a contour analysis on steel and PTFE surfaces (*Figure 3.11*).

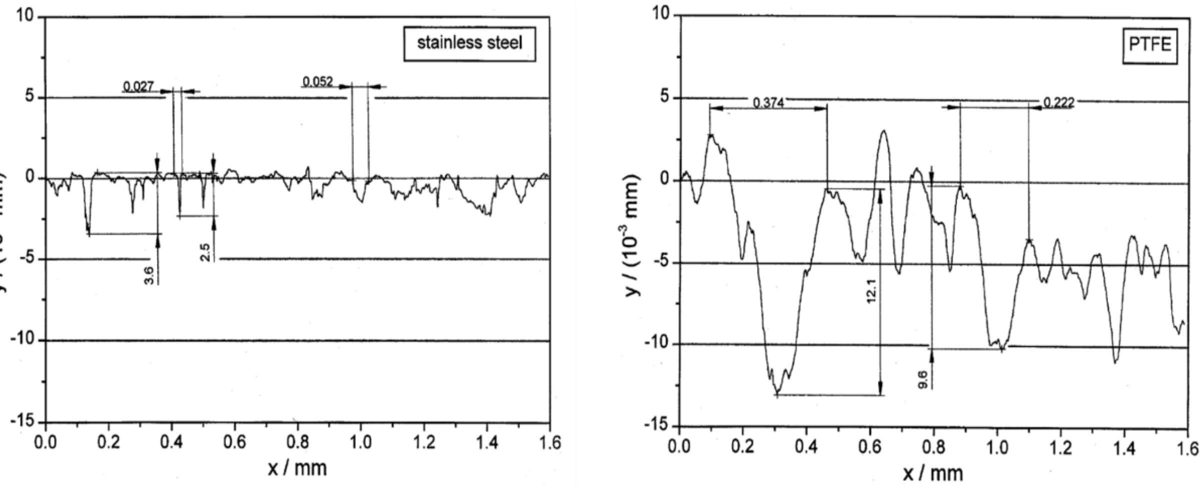

Figure 3.11: *Surface contour analysis of Stainless Steel and PTFE surfaces. Source: Förster and Bohnet (1999).*

They found that surface topography of steel decreased the adhesive strength at the crystal-HX surface because of the narrow crevices and flatter peaks (*Figure 3.11*). However, the PTFE surface increased the probability of attachment by crystals as it consists of greater depth and width of the valleys. These observations indicated that a wider crevice promoted scaling through adhesion while a narrow crevice could promote scaling through heterogeneous nucleation.

To understand why the difference in crevice width results in a difference in the scaling process, Bi et al. (2017), conducted a simulation study. The results indicated that an atomically sharp, concave crevice could promote ice nucleation. Enhancement of ice nucleation occurred when both the geometry of the crevice matched the ice lattice, and when there was no ice. This growth pattern could be due to the creation of areas of local supersaturation within the crevices which promoted the heterogeneous nucleation of ice in these crevices. Once heterogeneous nucleation started in the crevices, the water expanded. Hassan et al. (2010), posited that this expansion provided firm anchoring points for the ice, increasing the degree of adhesion through mechanical means. This increase of interfacial bonding strength with roughness was due to increased interfacial contact area, as shown in *Figure 3.12*.

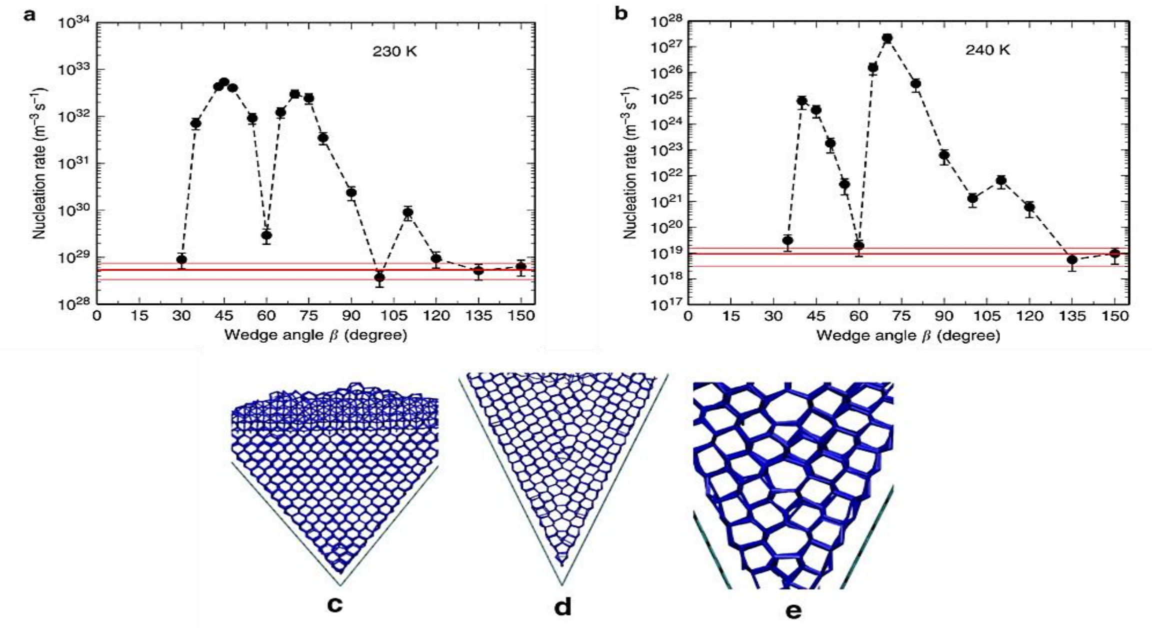

Figure 3.12: *Crystallization of mW water within the sharp crevice. The Redline indicates heterogeneous nucleation on the flat graphene surface. (c and d) are the side views of fully crystallized ice at 230K within the 70° and 45° crevice. (e) is (d) zoomed in. Source:* Bi et al. (2017)*.*

Figure 3.12 indicates that the simple reduction of the nucleation barrier, or the enhancement of the nucleation rate due to a decrease in the crevice angle, did not always hold (Bi et al., 2017). This variation is because the ice nucleation rate becomes indistinguishable from that on a flat surface, at some angles such as 30°, 60°, and 135° (Bi et al., 2017). At crevice angles 70° and 110°, ice nucleation was promoted due to structural lattice compatibility. In a 45° crevice, however, no structural lattice was observed, indicating that reduction of the entropic part of the Gibbs free energy barriers could be the reason for the enhanced nucleation (Bi et al., 2017). The Gibbs free energy barrier increased on flat surfaces. As Heydari et al. (2016) indicated, flat surfaces were more efficient in delaying freezing than rougher surfaces, as flat surfaces had a higher energy barrier to be overcome. This indicated that rougher surfaces increased wettability by providing an increased surface area in contact with the scalant, hence reducing the energy barrier for nucleation.

The presence of peaks on a surface may also contribute to reducing the Gibbs free energy barrier, because peaks contribute to the scaling process mainly by providing adhesion sites for the crystallizing material. Investigations have been conducted to quantify the adhesion strength of crystallizing material because of surface roughness using shear force testing. Zou et al. (2011), indicated that the smoother aluminium surfaces had a lower ice adhesion strength than rougher sandblasted aluminium surfaces. The enhanced nucleation on a rough substrate surface resulted in the formation of a stronger adhesive bond, due to the creation of more numerous crystallites.

Investigations by Keysar et al. (1994) corroborated these findings as disbanding stress of a deposit adhering to the roughest surface of R_a = 18 to 24 µm, was thirty times higher than that required to disband a deposit adhering to the smoothest surface of R_a = 0.1 µm. This was in agreement with data from MacAdam and Parsons (2004), where a 30% increase in adhesion strength was reported when the roughness increased from 0.2 to 0.8 µm. The increase in adhesion strength was attributed by Keysar et al. (1994), to the increase in the contact area between the crystallizing material and solid surface as roughness increases in their study of the effect of surface roughness on the scaling through its effects on the crystal nucleation and adhesion characteristics.

A study was conducted by Doyle et al. (2002) to identify the impact that supersaturation and material had on scaling rates of struvite. In this study, it was concluded that the low scaling propensity of struvite on a very smooth material was because it offered few sites for crystal growth and adhesion. This study indicates the required balance between surface free energy and roughness to combat scaling on a surface, as shown in *Figure 3.13*.

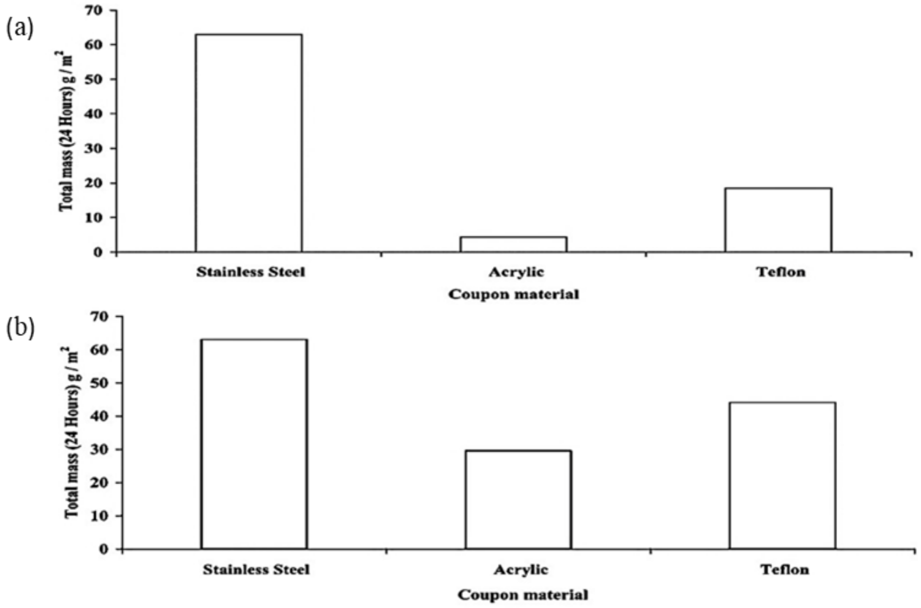

***Figure 3.13**: Comparison of mass formed on (a) smooth and (b) roughened stainless steel, acrylic, and Teflon Coupons. Source: Doyle et al. (2002).*

Figure 3.13 shows how surface roughness and chemistry combine to generate a surface that can combat scaling. Doyle et al. (2002), recorded that stainless steel had the highest deposit with the lowest change in the amount of deposit when comparing the smooth and rougher surface. However, the acrylic and Teflon finish reduced the scale forming on their surfaces by approximately 83% and 55%, respectively when smoothened. The authors concluded that the surface free energy could reduce scaling but, this influence diminished when they increased the surface roughness. Therefore, these results indicated that lower surface free energy of an HX material, as well as smoother topography, might increase the Gibbs free energy for heterogeneous nucleation, resulting in a delay in the scaling process.

In addition to delaying the onset of scaling, the crystallization process to rehabilitate waste brines requires that the heterogeneously nucleated and adhered crystals be easily removed from the HX surface of the crystallizing unit. It is an advantage if this can be done without an external influence within a continuous process like EFC. In this continuous process, the deposition of a crystallizing material is attracted by adhesive interfacial forces to the HX surface. Förster and Bohnet (1999), observed that adhesion is minimized with higher velocities due to the higher removals which are caused by higher shear stress between fluid and crystals. Zou et al. (2011), predicted that the adhesive interfacial forces would have to exceed the removal of ice by shear force within the continuous process to make fluid velocity counteract the effect of surface roughness. If this prediction is accurate, it indicates that surface topography balanced with the surface free energy of the HX surface plus the fluid velocity at the interface might minimize the scaling processes in the crystallizing unit.

3.3. Gap analysis

The industrial treatment of brine solutions using EFC has experienced major drawbacks due to difficulty in controlling scaling on the HX surface. The control of ice scaling in EFC has been done mainly through active methods such as mechanical scraping. Numerous studies have been conducted to see whether changes in scraper design and efficiency improve scale control (Vaessen, Janse, et al., 2003; Crespí-Llorens et al., 2013). Scrapers, however, as an active form of scale prevention, are prone to mechanical breakdowns which result in additional operational costs and increased downtime.

Minimal attention has been given to the effect of the HX surface properties to reduce ice scaling in EFC. Vaessen et al. (2002), stated that the HX material choice did not affect the probability of scaling, and that differences in scaling patterns occurred due to the variation in the supersaturation levels. That study was conducted using scrapers, which may have influenced the results. This means that the influence of the HX surface was not considered independently as a contributing factor to scaling, and the extent to which the HX surface properties influence ice scaling in EFC is currently unclear.

Numerous studies have investigated the effect of surface properties on ice scaling. Surfaces can be modified to alter properties such as surface free energy and topography. Such properties have been shown to play a crucial role in the scaling of HX surfaces. Materials of low surface free energy have been found to delay the onset of scaling (Yang et al., 2002; Tourkine et al., 2009), reduce the drag at the interface (Moaven et al., 2013; Lv and Zhang, 2016) and reduce adhesion strength of crystalline material (Matsumoto and Kobayashi, 2007; Zou et al., 2011). These studies have further indicated that, when using a material of low surface free energy or hydrophobic material, it is possible to attain lower freezing temperatures when cooling a brine solution (Yin et al., 2010; Carpenter and Bahadur, 2015). Applying this knowledge to the EFC process and investigating how HX surfaces affect scaling in flow systems operated at cryogenic temperatures, may make it possible to control the scaling issue passively.

It is currently unknown how this passive approach could influence the process efficiency of EFC as it has not yet been explored. It is, therefore, important to investigate how surface modification could assist in the mitigation of scaling in EFC. This includes investigating the effect of surface characteristics like surface free energy and topography on the scaling process during EFC. This kind of knowledge could complement the currently used active remedy, scraping, to achieve the highest reduction in the scaling of HX surfaces.

The effect of HX surface properties in an EFC system without the use of scrapers has not yet been investigated. With the untapped potential for delaying the onset of scaling, reduction of drag at the interface and minimising crystal adhesion, research into surface properties could build an understanding of the passive option for reducing scaling in EFC. Hence, this study decouples the HX surface from the use of scrapers to make two focus areas to study the effect of the HX surface properties on ice scaling without the influence of mechanical scraping. Modified HX surfaces could increase the efficiency of scraping. Kreder et al. (2016), say that this could be achieved by reducing the required scraper rotational speeds and force used to prevent ice from scaling, thus contributing to possible energy savings, reduction in operational downtime and operations safety during the removal of ice during EFC.

The ice scale layer forms through heterogeneous nucleation and growth. Kapembwa et al. (2014), measured the growth of the ice on the HX surface only normal to the HX plate. The nucleation and horizontal growth of the initial ice layer on the HX plate have not yet been observed in-situ and in real-time. Therefore, this study shows how scaling modes of the initial ice scale layer differ on the different HX surfaces, providing insight into the scaling rates and morphology of the initial ice scale layer, which has been found to persist after scraping.

3.4. Hypotheses and key questions

1) **The decrease in surface free energy of heat exchanger materials results in an increase in the ice scaling induction time and a decrease in the ice scaling rate**. This is because materials of low surface free energy have reduced wettability, therefore reducing the solution-solid material interaction. The reduction in the solution-solid interaction reduces the viscous drag at the interface, delaying the onset of freezing and decreasing subsequent scaling rate.

   a) Does decreasing the surface energy of a material increase the ice scaling induction time?
   b) Does changing the material affect the ice scaling mode?
   c) Is the ice scaling rate affected by different HX materials?

2) Surface topography affects scaling on the crystallizer wall because crevices create regions of high local supersaturation for nucleation and provide sites for adhesion of crystalline material. **Therefore, a surface with an increased roughness as a result of valleys, crevices and peaks leads to shorter ice scaling induction times and higher ice scaling rates.**

   a) Does increasing the surface roughness of a material decrease the ice scaling induction time?
   b) Does changing the material roughness change the ice scaling mode?
   c) Does increasing surface roughness increase the ice scaling rate on the HX surface?

4. Materials and Methods

This section gives details, including explanations, of the two-part experimental plan to observe and understand the effect of surface free energy and topography on scaling. The solution used and its preparation are described, as are the equipment and how it was used in the overall experimental set-up. The measurement techniques used to analyse the data obtained from the experiments are detailed. Lastly, the experimental procedure is explained.

4.1. Experimental plan

The following table provides a summary of the experimental plan. The experiments were conducted in two sections, the first to study the effect of surface free energy on scaling, and the second to study the effect of surface topography on scaling.

***Table 4.1**: Summary of the experimental plan*

Aim		**Control Variables**	**Measured Variables**
1.	This experiment is aimed at investigating the effect of the surface free energy of construction material on the scaling on the HX surface. This is done by varying the materials of construction and using a hydrophobic coating on SS316.	Primary-SS316 (as received)	Bulk and surface temperatures at nucleation Induction time, t_{in} Nucleation rates Growth rates
		Brass	
		Copper	
		Aluminium	
		PTFE Coated-SS316	
2.	This test is aimed at providing insight into how the surface topography affects scaling at the HX surface at different cooling temperatures. SS316 is used as a case study, due to its widespread use in industry.	Primary-SS316 (as received)	Bulk and surface temperatures at nucleation Induction time, t_{in} Nucleation rates Growth rates
		Micro-blasted-SS316	

4.2. Synthetic solution

An approximately eutectic 4 wt.% Na_2SO_4 – H_2O binary synthetic solution was used in these experiments. This was chosen because the sodium sulphate is one of the predominant salts found in industrial brine solutions. The eutectic temperature for this solution is -1.14 °C (Reddy et al., 2010). Therefore, the scaling induction time for this solution was measured from the eutectic temperature until the scaling temperature is reached. The metastable zone width of the sodium sulphate system has been determined by Lewis et al. (2010) and is indicated in *Table 4.2*.

***Table 4.2**: Metastable zone width (MSZW) for the Na_2SO_4-H_2O system. Source:* Lewis et al. (2010)

Cooling rate (°C)	**MSZW, H_2O (°C)**	**MSZW, $Na_2SO_4\cdot10H_2O$ (°C)**
1.5	4.1	2.9
4	4.5	2.1
6	5.5	3.4

4.3. Experimental set-up

4.3.1. Crystallizer test cell

The crystallization test cell was designed to mimic the region near the crystallizer wall. The Perspex glass allowed for the observation of the initial scale layer on the heat exchanger (HX) surface, as it is transparent. The dimensions of the test cell can be found in *Appendix A.1*, which shows the cross-section front view, the top view, and the side view of the test cell. *Figure 4.1* indicates the 3D view of the test cell.

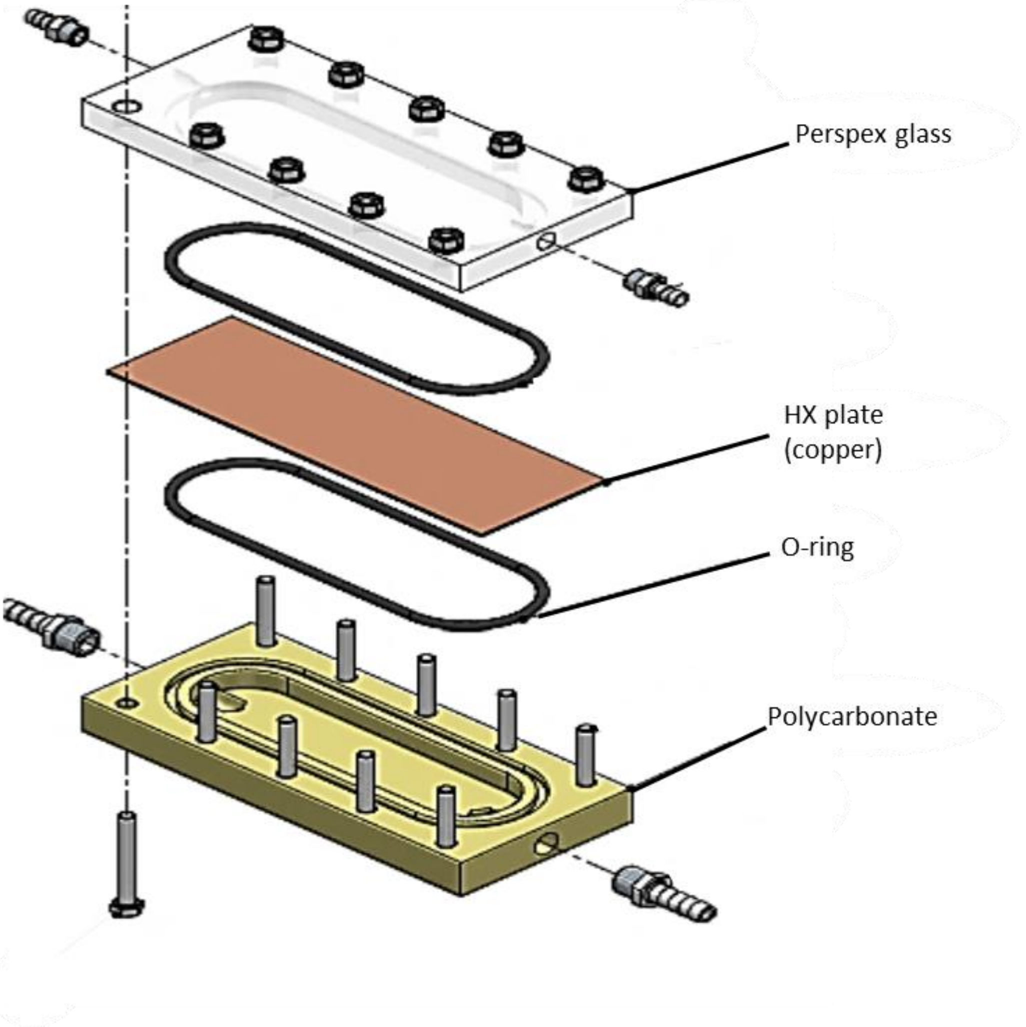

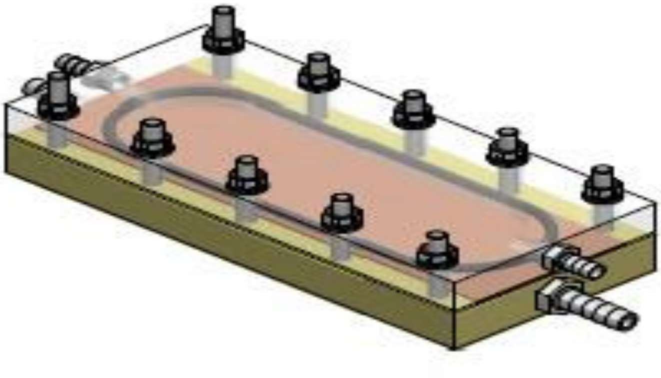

Figure 4.1: *3D Image of the Crystallizer test cell.*

The cell consisted of two chambers, the coolant part (bottom) and the solution part (top). These chambers were separated by the material of construction, which served as the heat exchanger plate, which was the focus of the investigation. The coolant chamber was made from polycarbonate to minimise heat transfer from the surroundings, and the top chamber was made from Perspex to minimise heat transfer from the surroundings and allow viewing of the contents in the test cell. The top and bottom chambers of the test cell were sealed with O-rings, to avoid mixing of the fluids. The design parameters are detailed in *Appendix A.1* The test cell formed the main unit of the experimental set-up, indicated in *Figure 4.2*.

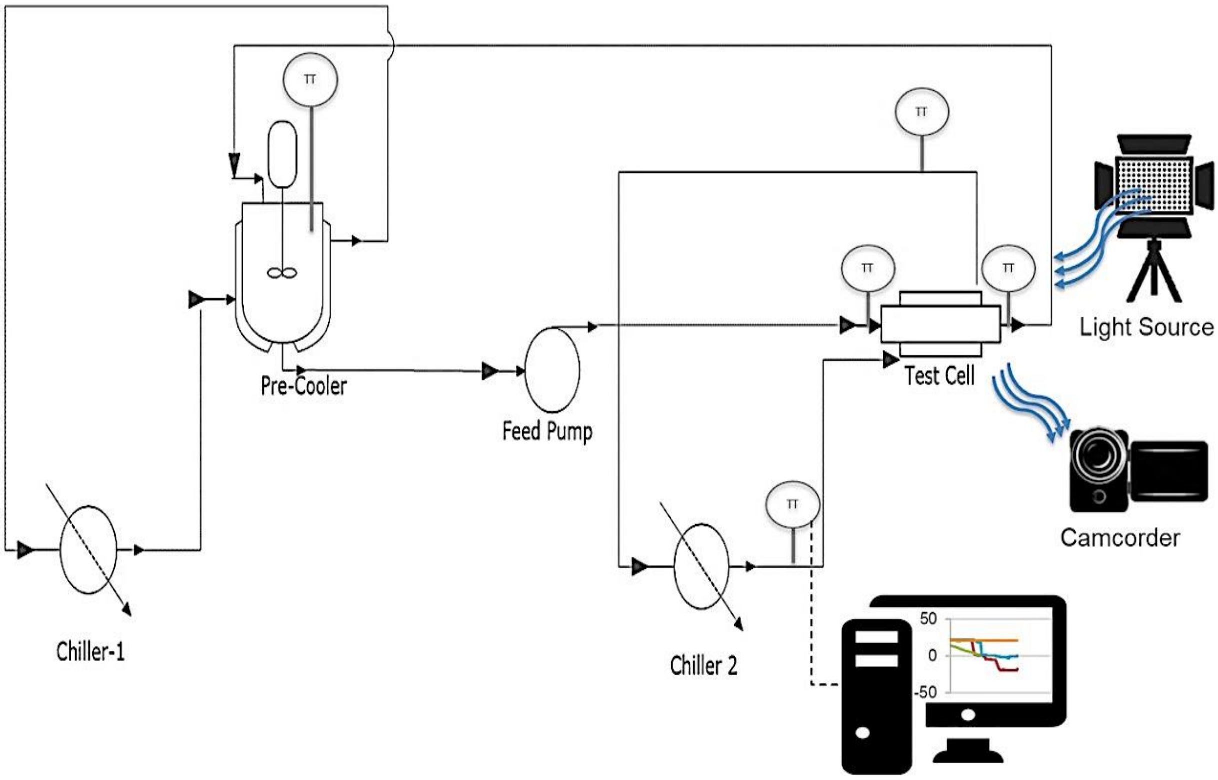

Figure 4.2: *Experimental setup*

A 2 ℓ borosilicate jacketed glass vessel, connected to the Lauda E 200 chiller, was used for pre-cooling the brine solution. The chiller circulated Kryo-51 (*polydimethylphenylsiloxane*) as the coolant. A Lauda Proline RP855 chiller using Kryo-51 coolant was used for cooling the brine solution flowing through the test cell. The tubes from the chiller were connected to the bottom chamber of the test cell. The coolant was circulated in and out of the bottom chamber of the test cell to cool the contents in the top part of the test cell. The coolant flowrate into the crystallizer test cell was kept at the chiller's maximum flow rate, to minimise heat transfer resistance by the equipment.

The pre-cooler outlet pipe was connected to a Watson Maslow peristaltic pump. This pump fed the pre-cooled solution into the test cell top chamber. The solution flowed out of the test cell and back into the pre-cooler. PT-1000 temperature probes (TT) were connected to measure the temperatures of the environment, pre-cooler contents, the coolant and brine solution inlet, and the outlet. These temperature probes were connected to an ASL F250/300 precision thermometer with an accuracy of ± 0.01 °C. The data was recorded using ASL U-log software and analysed using Excel.

A Canon HD Legria HF S21 camera, fixed at a 45° angle, was used to acquire digital images. The camera lens was fitted with a Hoya Pro01 digital filter polarising lens. A Godox LED 500C light source was used to shine a light on to the cell. A polarizing filter was fitted in front of the light source to allow the light of one plane to reach the cell. The light source was positioned at a 45° angle opposite the camera. This enabled the camera to detect polarised light from the test cell.

4.4. Measurement Techniques

4.4.1. Heat Exchanger (HX) material properties

The five metal plates used in this investigation were one of each of stainless steel 316, aluminium, brass, and copper, PTFE-coated and micro-blasted SS316 surfaces. These metals were chosen as they are widely used in HX studies. The surfaces were washed thoroughly with detergent, soaked in distilled water, and air-dried. The composition of the metals was provided by the supplier and confirmed using the Scanning Electron Microscope-Energy Dispersive Spectroscopy (SEM-EDS) by Oxford Instruments from the United Kingdom *(Appendix A.2*). The surface energies of the metals were obtained from literature are summarised in *Table A.1*.

The surface topography for the metals was determined using a Tuscan Micra3 scanning electron microscope from the Czech Republic. Scanning Probe Microscopy (SPM) was used to measure the material's surface roughness. PeakForce Tapping™, a Brucker-exclusive Atomic Force Microscopy (AFM) mode was used to analyse the surface topography. NanoScope Analysis software 6.13 was used to obtain the Rq and Ra values and to analyse the topographical images of the metal surfaces.

4.4.2. Qualitative observations of the scaling modes

Qualitative observations of the initial ice scale layer were obtained using the Differential Interference Contrast (DIC) method. This method allows for transparent samples, like ice, to be observed when forming surfaces, where otherwise that ice formation would be undetectable. When using DIC, light waves are emitted from the source and linearly polarised using a polariser. The linearly polarised light enters through the Perspex glass at the top of the test cell and water flowing within the test cell, causing a split in the incident light. The Perspex glass and water act as a prism that splits the light beam into two rays vibrating perpendicular to each other.

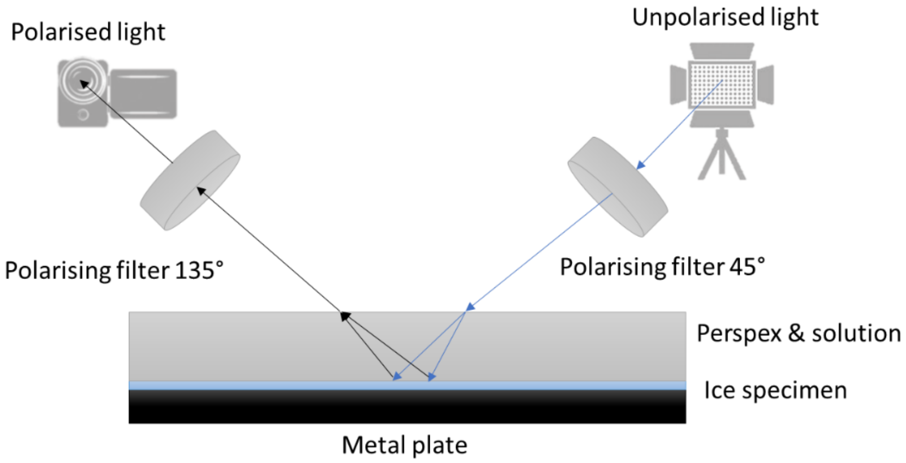

Figure 4.3: *Simplified adaptation of the DIC Set up for observation of ice formation on the HX surface*

The split beams hit the surface of the metal plate where the ice scale layer formed. This ice layer had varying thicknesses, which altered the wave paths of the beams. These beams had different lengths due to the phase shift of light, caused by the retardation resulting from the forming ice scale layer. This light was captured by the camera fitted with a polarizer. The polarizer brought the vibrations of the beams into the same plane and axis, causing constructive and destructive interference to occur between these two wavefronts. The light then travelled to the camera, where the DIC image with differences in amplitude and colour, was captured, creating a pseudo-3D effect, with different interference colours. The light source and the camera were placed at a 45° angle to allow maximum brightness from the sample, as indicated in *Figure 4.3* (Murphy et al., 2020).

4.4.3. Scaling induction times, nucleation, and growth rates

Crystallization in the test cell was observed through the change in temperature of the solution recorded on the ASL U-log software. A sudden increase in temperature indicated the point of nucleation. The scaling induction times were obtained from the recorded ASL U-log data, which indicated the time taken for scaling to occur after the eutectic point of the system had been reached.

Nucleation rates were found by manually observing and counting the number of nucleation islands that formed on the HX surface with time. The horizontal growth rates on the surface of the HX material were found by measuring the rate at which the ice nuclei islands grew parallel to the HX surface. Frames were extracted at 25 frames per second from the video, captured using the method described above, using VideoProc digiarty software. These frames were processed using ImageJ to obtain the pixel coordinates of the growing nucleation centres. The pixels were converted into length from calibrations conducted for all videos.

4.5. Experimental procedure

4.5.1. Start-up

A fresh solution of 4 wt.% sodium sulphate was prepared at room temperature, for every experiment, to avoid the effects of solution memory in the experiment. 1 ℓ of the solution was poured into the pre-cooler, and the chiller for the pre-cooler was set to a constant -4 °C. This pre-cooling temperature was chosen as it was the lowest temperature that could be used without causing bulk nucleation or scaling in the pre-cooling system. The solution was pre-cooled to remove the sensible heat until the solution reached 5 °C before circulating the solution. This precaution was necessary to avoid pre-cooling the solution to sub-zero temperatures, to avoid crystallization in the pre-cooling unit. During this pre-cooling time, heat losses were determined co-currently for every experiment.

The heat loss was obtained experimentally by insulating the inside of the test cell. The coolant flowed through the test cell coolant chamber without any solution flowing in the test cell. The temperature difference between the inlet and outlet of the coolant was measured. The difference in the coolant temperature at the inlet and outlet provided the heat loss for the system, as all the heat gained by the coolant was assumed to be that from the surroundings.

Once the pre-cooled solution had reached approximately 5 °C in the pre-cooler, the heat loss measurements were stopped, and the test cell coolant was at its operational temperature of -20 °C. This was to remove the insulation material from the test cell before the pre-cooling decreased the temperature below 5 °C. As these experiments have not been conducted previously, a trial and error method had to be used to find a coolant temperature that would allow scaling onto all material. From this exercise, the coolant temperature was initially set to -20 °C. Therefore, this temperature was used as an initial set point to ensure that the Na_2SO_4 - H_2O solution reached its nucleation temperatures for all materials of construction.

The solution was circulated through the system at 43 mℓ.s^{-1}, through the test cell, and back to the pre-cooler. At this point, the solution was cooled by the coolant which flowed through the bottom chamber of the test cell at 86.9 mℓ.s^{-1}. The solution and coolant flow rates were the maximum the system could achieve. When the solution reached a temperature below 0 °C, the camcorder was switched on, and frames were captured until ice scaling occurred.

4.5.2. Investigating the effect of surface free energy and roughness on ice scaling in EFC

A sodium sulphate solution was subjected to indirect cooling, with metals of different properties used as Heat Exchanger (HX) plates. The coolant temperature was kept at a constant at -20 °C, as a basis point, as this was the temperature where it was initially expected that ice scale would occur in the system. After obtaining experimental data from experiments conducted at -20 °C, the data was used to adjust the coolant temperature, to enable operations at similar heat fluxes for all materials. Further experiments were conducted at the same heat flux for all the HX plates, to reduce the influence of the thermal conductivity on the scaling process. This was achieved by adjusting the coolant inlet temperature, based on the thermal conductivity of the material, to match the heat flux reached by SS316 at -20 °C. SS316 was used as the reference material because it has the lowest thermal conductivity of all the metals used in the investigation. The coolant temperatures required to achieve heat fluxes similar to that achieved using the SS316 plate were calculated, using the heat transfer equations. Therefore, the different thermal conductivities were expected to have minimal influence on the resulting induction times. The scaling induction times, scaling modes and crystallization kinetics were obtained using the methods stated above.

A PTFE-coated SS316 HX plate and a micro-blasted SS316 were used to study the effect of surface free energy and topography on scaling. These experiments were conducted at a coolant set temperatures of -15 °C, -20 °C and -25 °C. The scaling induction times, scaling mode and crystallization kinetics were compared to those of the primary SS316.

5. Results and Discussion

This chapter discusses the findings for the investigations on the effect of surface energy and topography on the scaling phenomenon. The results presented in this section include the scaling induction time and the corresponding bulk and near-surface supersaturations at nucleation, the qualitative data observed using Differential Interference Contrast (DIC), the nucleation and horizontal growth rates and the overall scaling rates. It was crucial to investigate how these variables can be affected by the HX materials used, which showed in the scaling process during EFC. The data obtained originated from the temperature profile graph produced for every crystallization experiment conducted.

5.1. Experimental temperature profile

A temperature profile graph was obtained directly from the readings of the temperature probes during each experiment. Figure 5.1 shows the temperature profile of the crystallization experiment for SS316 at a coolant temperature of -20 °C.

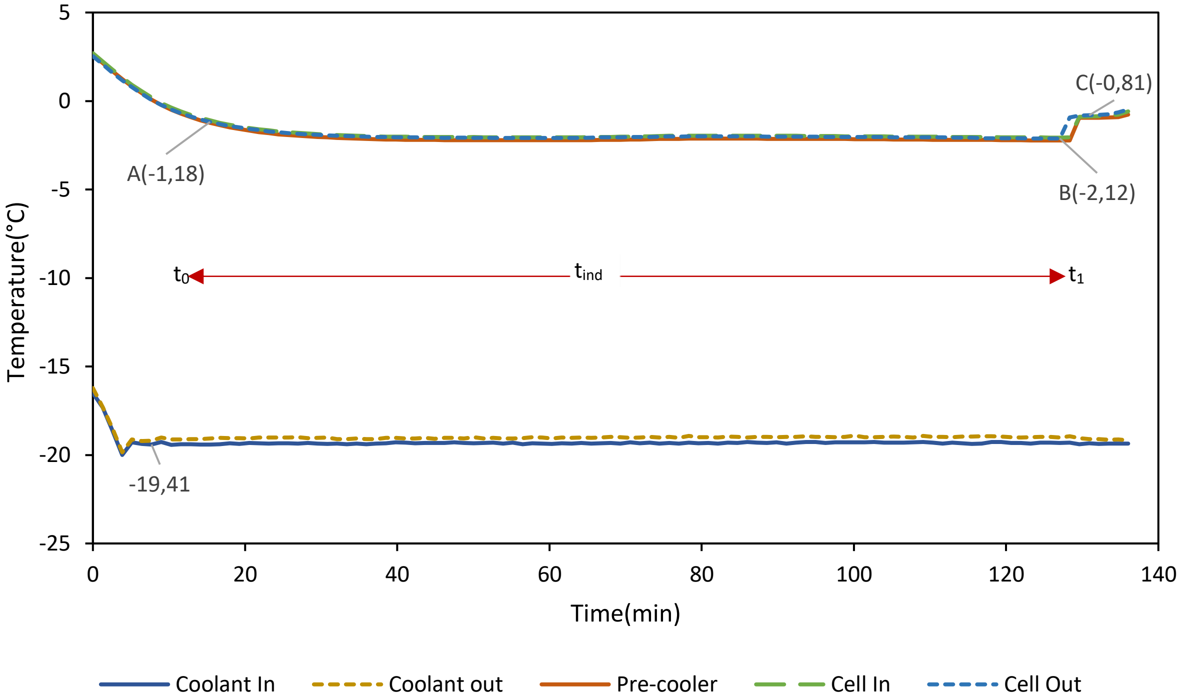

Figure 5.1: *Temperature profile of scaling test on SS316 using $Na_2SO_4 \cdot H_2O$ binary solution of near eutectic composition.*

The chiller temperature was set to -20 °C, while the coolant temperature at the cell inlet was measured as -19.41 °C. The increase in coolant temperature was due to heat loss through the tubing to the test cell. The coolant indirectly cooled the flowing bulk solution in the solution chamber through the heat exchange (HX) plate resulting in an increase in its temperature to -19.05 °C as it exited the test cell. Once scaling occurred, the recorded coolant exit temperature dropped and became similar to the inlet temperature, indicating that less heat dissipated from the system. This trend was observed in all the experiments conducted.

The temperature of the bulk solution in the test cell was assumed to be similar to the temperature of the product solution ("Cell Out"). Tracking this temperature profile enabled the identification of the time when the solution reached the eutectic temperature in addition to the occurrence of surface nucleation. The solution reached the eutectic temperature (-1.1 °C) within 20 min, as indicated by the data point A, in *Figure 5.1*, where the recorded bulk temperature was -1.18 °C.

From point A, the bulk solution was in the metastable zone, and this indicated that the solution was supersaturated. In this zone, nucleation occurs through either heterogeneous primary nucleation or secondary nucleation (Mullin, 2001). The system plateaued for a specific period from point A, to point B. Lupi, Peters and Molinero (2016) indicated that during this period, the water molecules aggregated and formed clusters that grew until they reached the critical size for nucleation or re-integrated back into solution. These clusters formed as part of the initiation of nucleation in a solution (Myerson, 2002). Therefore, it can be deduced that clusters reached a critical size at point B.

At point B, ice nucleated heterogeneously on to the HX plates or in the suspension. The heterogeneous nucleation and growth of the ice on the HX surface were observed using DIC. Since the scale formation was captured using a digital camcorder, it is acknowledged that the actual nucleation step occurred earlier than the point of detection. This is because the formation of a stable ice nucleus may contain approximately 100 molecules, which is only a few nanometres in size. The equipment used could not detect to the nanometre scale. Therefore, crystals that were observed on the HX surfaces had to have already grown into a detectable macroscopic size to be detected.

A rapid increase in the temperature of the bulk solution, from -2.12 °C to -0.81 °C, was observed from point B to C. The increase in temperature was due to the release of the heat of crystallization upon nucleation because the crystallization of ice is exothermic. The solution reached the maximum supersaturation level at point B, which represented the metastable limit of the system. The time between the attainment of eutectic temperature, at point A, and the nucleation temperature at point B was defined as the scaling induction time ($t_{ind} = t_1 - t_0$). The scaling induction time for this specific experiment was 110 min. This scaling induction time (t_{ind}) was used as a measure of the scaling process on the different materials of construction, together with the resulting temperatures at nucleation.

5.2. Ice scaling on metals of different properties

The first hypothesis was tested by using metals of different surface properties, to observe the effect of surface free energy on the; scaling induction times, scaling mode and on the crystallization kinetics. This section evaluates and discusses the observed effects of using materials, each with a different surface free energy, on the scaling of ice in EFC. To further understand the effect of surface free energy, a hydrophobic PTFE coated surface was used to investigate the effect of lowering the HX surface free energy on ice scaling in EFC, and the extent of its efficacy at different cooling rates.

5.2.1. Effect of surface properties on the ice scaling induction time

The ice scaling induction time was defined as the time that elapsed between the attainment of eutectic temperature (-1.1°C), for a 4 wt.% Na_2SO_4 aqueous solution, and the inception of detectable ice scale on the surface of the HX plates, as observed by using the DIC method. The SS316, Brass, Aluminium and Copper HX plates were used, as received from the manufacturer without any modification. For the precise measurement of the scaling induction times, strictly controlled experimental conditions were required, because the measurement of these induction times was highly susceptible to the rate of pre-cooling, solution memory, and other external disturbances such as vibrations on the countertop.

5.2.1.1. Ice scaling induction time when operating at a coolant temperature -20°C

Preliminary ice scaling experiments were conducted at a constant coolant temperature of -20 °C for all HX metals used in the study. These experiments provided data that enabled the appropriate adjustments to the coolant operating temperature in order to achieve similar heat fluxes when using different HX materials. The scaling induction times were recorded for experiments conducted at a constant coolant temperature of -20°C (*Figure 5.2*). The T^* is the eutectic temperature, $T_{HX\text{-}surface}$ and T_{bulk} are the HX surface and bulk solution temperatures at the point of nucleation. The supersaturations in bulk ($\Delta T_{bulk} = T^* - T_{bulk}$ (°C)) and near the HX surface ($\Delta T_{HX\text{-}surface} = T^* - T_{HX\text{-}surface}$ (°C)), at the point of nucleation, are illustrated by the open markers, and the scaling induction times by the solid markers. The near-surface supersaturation is important for the scaling process in the system, as it provides the driving force for heterogeneous nucleation at the HX surface.

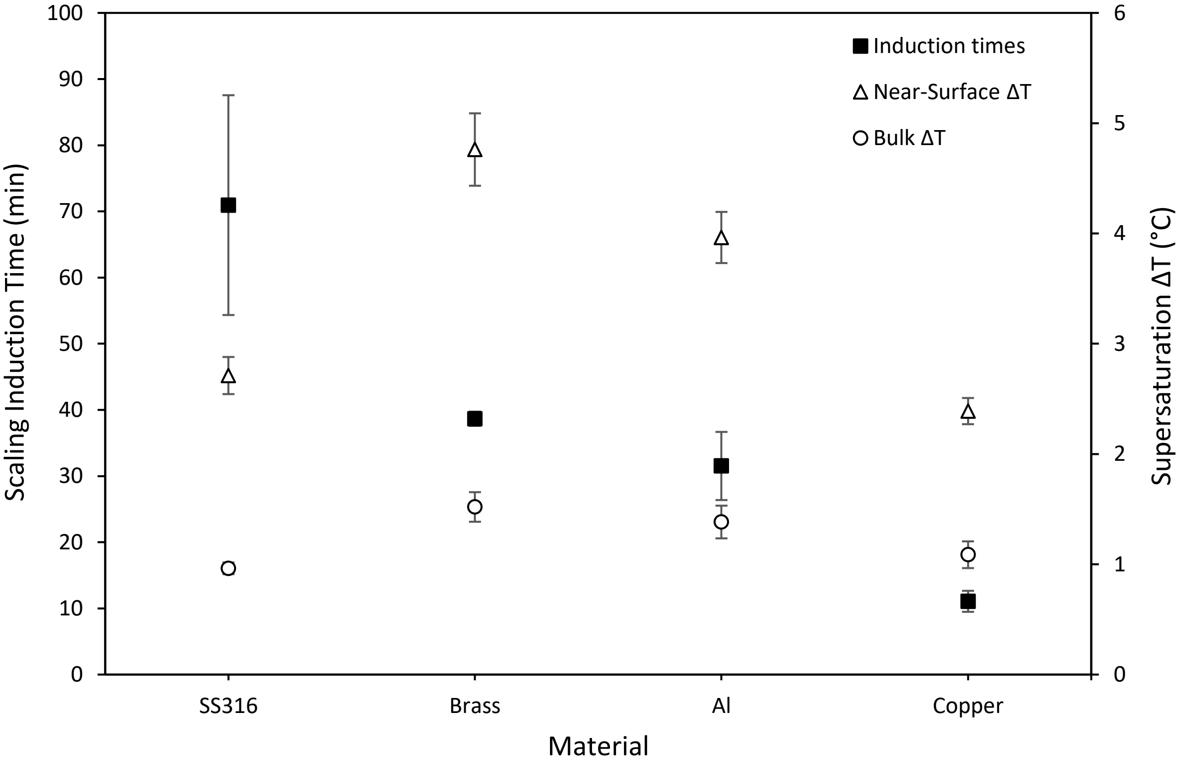

***Figure 5.2**: Ice scaling induction times (solid markers) obtained when using different HX materials, at a coolant temperature of -20°C, and the respective bulk and near-surface supersaturations (open markers).*

Figure 5.2 shows the relationship between the different HX materials and the required scaling induction time to reach the required level of supersaturation for nucleation to occur. The research data indicate that there is an inverse linear relationship between the scaling induction time and the different properties of the HX materials. It is acknowledged that this relationship is a consequence of material properties such as surface roughness, surface free energy and thermal conductivity.

Therefore, these material properties played a significant role in obtaining the data in *Figure 5.2*. However, the degree of influence of each property is unknown.

The solution was cooled using similar coolant temperatures, and the resulting cooling rates were dependent on the HX materials thermal conductivities. The thermal conductivities of these materials rank as follows: SS316 < Brass < Aluminium << Copper. Thus, the ice scaling induction time was affected by the thermal conductivities to some degree, as they influenced the cooling rates.

The ice scaling induction times recorded when using the SS316, Brass and Aluminium HX plates were 6.41, 3.45 and 2.85 times higher than that of the Copper HX plate. These were the times taken for the ice to nucleate spontaneously after exceeding the eutectic temperature. Beckmann (2013) states that during this period, the system is metastable, and the time between crossing the solubility line and spontaneous nucleation decreases with the increase in the cooling rate. Therefore, the increase in the material thermal conductivity accelerated the cooling rates. Consequently, shortening the duration that the solution remained metastable.

Although the coolant temperature was kept constant at -20°C, *Figure 5.2* shows that the thermal conductivities of the different materials influenced the cooling rates of the system, and possibly the supersaturation levels at nucleation. The level of supersaturation reached in the system decreased in direct relation to the material thermal conductivities, except for SS316. According to Mullin (2001), the difference in cooling rates affects the maximum allowable supersaturation, thus influences the resulting near-surface supersaturation at the point of nucleation. The near-surface supersaturations at nucleation increased as follows: Brass > Aluminium > SS316 >> Copper. These findings suggested that the increase in the thermal conductivity, i.e., a faster cooling rate, resulted in a subsequent drop in the maximum attained supersaturation. This observation was unexpected because the work by Gutwald and Mersmann (1990) showed that for higher cooling rates, the supersaturation maxima results in higher values.

For a Na_2SO_4-H_2O system, Lewis et al. (2010) showed that a faster cooling rate increases the average metastable zone width (MSZW) for the region where ice forms. Therefore, the near-surface supersaturations were expected to increase with the thermal conductivity due to faster cooling rates. However, the opposite result was obtained in this study, which can be attributed to nucleation occurring heterogeneously on the HX surface, as opposed to the bulk solution. The findings by Lewis et al. (2010) were based on nucleation occurring in the bulk solution, as opposed to heterogeneous nucleation on an HX surface. In addition to material thermal conductivity influencing the cooling rates, it is evident that the material surface properties also affected the supersaturation required for heterogeneous nucleation. The results showed a reduction in the required level of near-surface supersaturation for heterogeneous nucleation in the following order: Brass > Aluminium > SS316 >> Copper.

The system reached the highest near-surface and bulk supersaturations when the Brass HX surface was used. In comparison, the bulk supersaturation near the Aluminium HX were 10.0 % and 16.8 % lower than those near the Brass HX plate. The higher levels of supersaturations observed could be because of the lower surface free energy in the case of Brass, and the smooth topography in the case of Aluminium. Therefore, the higher supersaturations levels reached when using Brass and

Aluminium HX plates indicated that a higher driving force was required for nucleation to initiate on both these materials than on Copper and SS316 HX plates.

The bulk and near-surface supersaturations for SS316 (39.95 % and 43.1 %) and Copper (28.2 % and 49.7 %) were lower than that of the Brass plate. These results indicated that the supersaturation required for nucleation on these surfaces was reduced. These levels of supersaturation recorded when using the Copper and SS316 HX plates were comparable. However, the time taken to reach this supersaturation level was 6.4 times longer for SS316 relative to Copper. These results indicated that the high surface free energy of the Copper HX plate and the rough surface topography of SS316 might have increased the probability for heterogeneous nucleation by reducing the Gibbs free energy needed for nucleation.

The driving force for ice scale formation was determined by the supersaturation generated near the HX surface. According to Langham and Mason (1958), the maximum attainable degree of supersaturation was dependent on the volume of the solution, the solution purity and the cooling rate of the system. The cooling rate was altered by the thermal conductivities of the materials, even though the coolant temperature was kept constant at -20°C. Therefore, the cooling rate may have altered the maximum attainable degree of supersaturation of the system, resulting in different scaling induction times. Thus, it was essential to conduct the experiments at similar heat fluxes to reduce the effect of thermal conductivity of the resulting scaling induction times. By reducing the effect of thermal conductivity, the resulting scaling induction time became a function of the surface free energy and topography of the materials.

5.2.1.2. Ice scaling induction time using different metals at similar heat fluxes

For this set of experiments, cooling was conducted at similar heat fluxes using the different HX materials, to eliminate the effect of the different thermal conductivities on the cooling rate of the system. When the system was operating at similar heat fluxes, the influence of surface free energy on the scaling induction times was observed. The coolant temperatures required to achieve heat fluxes similar to those of SS316 were calculated using heat transfer equations and data obtained from the previous set of experiments. The resulting scaling induction times are presented in *Figure 5.3*.

The heat fluxes were adjusted to match those of SS316 because it had the lowest thermal conductivity. The resulting scaling induction times were assumed to have been minimally influenced by the thermal conductivities of the different HX materials. Thus, the solution was subjected to similar cooling rates, while the surface properties such as surface free energy and roughness remained different. Accordingly, the scaling induction times were increased by 142%, 201%, and 388% for Brass, Aluminium, and Copper, respectively, compared to the results obtained when operating at -20°C (*Figure 5.2*).

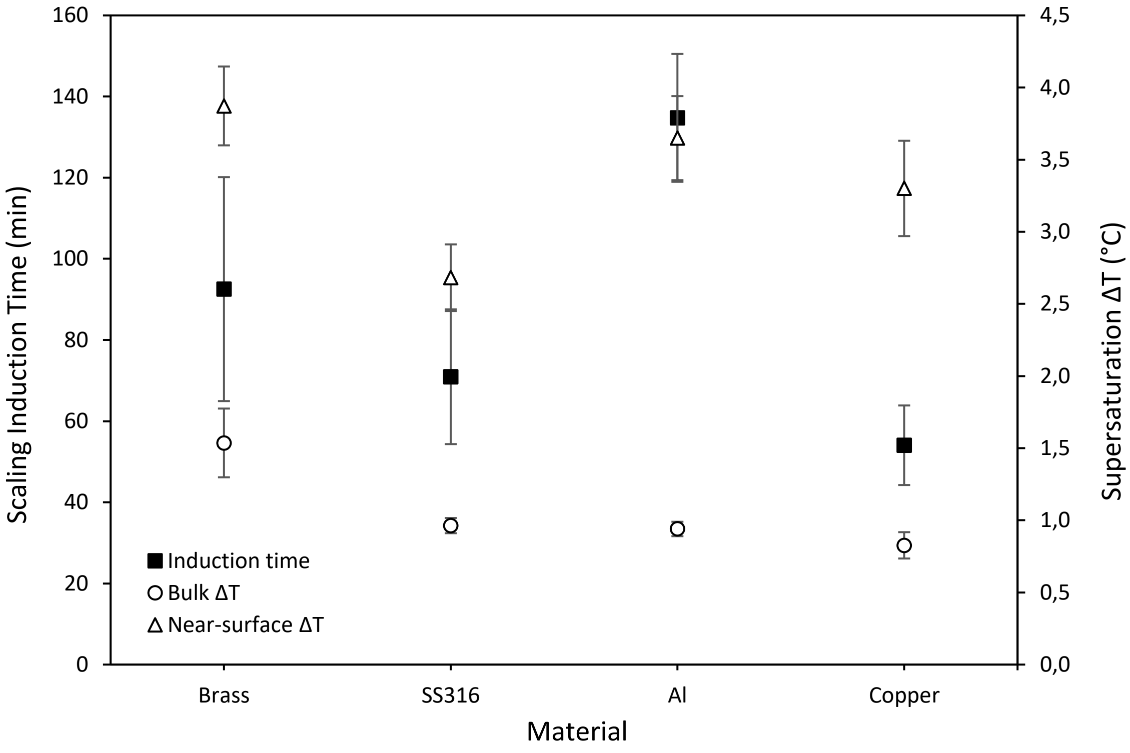

Figure 5.3: *Effect of surface properties on the ice scaling induction time (solid markers) and the bulk and near-surface supersaturations at nucleation (open markers), when operating at similar heat fluxes.*

Figure 5.3 shows the scaling induction times, and the supersaturation at nucleation, when operating at similar heat fluxes, using different HX materials. These HX materials are presented in ascending order of their surface free energies, where Brass < SS316 < Aluminium << Copper (Förster and Bohnet, 1999). The recorded scaling induction times decreased with an increase in the surface free energy of the material with Aluminium as an outlier. The scaling induction time for Aluminium was 1.4, 2.0, and 2.5 times higher than those recorded for Brass, SS316 and Copper, respectively. The near-surface supersaturation at nucleation indicated the required driving force for heterogeneous nucleation at the liquid-HX surface interface. These near-surface supersaturations followed this order: Brass > Aluminium > Copper >> SS316. The length of the scaling induction times, together with the levels of supersaturation, both indicated the resistance of the material to heterogeneous nucleation.

The scaling induction times that were reached when operating at similar heat fluxes differed for all the materials used. The observed differences were attributed to properties such as the surface free energy and surface topography. Since these materials were used as received or without any modifications, the material's properties simultaneously contributed to affect the scaling induction times and supersaturations. Therefore, it was essential to take into account the effect of both these material properties on the obtained results.

Förster and Bohnet (1999) noted that to accurately compare the effect of surface free energy on the scaling induction time, the surface topographies needed to be as similar as possible. In this study, the Brass and Copper plates were the only materials which displayed similar topographies (*Appendix A.2*). Therefore, the scaling induction time for Brass (1.7 times longer than that recorded for Copper) can be mainly associated with the difference in their surface free energies. The near-surface supersaturations reached on the Brass HX plate was 1.2 times higher than that of the Copper HX plate. This result indicates that the Gibbs free energy for nucleation was higher on the Brass plate when compared to the Copper HX plate. Therefore, the higher near-surface supersaturation was required for heterogenous nucleation to occur on the Brass HX plate relative to the Copper HX material. This comparison clearly shows that the material of higher surface energy (Copper) reduced the scaling induction time, as well as the required level of supersaturation for nucleation.

Due to its high surface free energy, the shortest induction times were recorded when the Copper HX plate was used. According to Xu et al. (2015), nucleation preferentially initiates on the high surface free energy material, and the clusters that are formed on the surface are trapped around their original positions instead of migrating around due to higher interfacial tensions. The results in *Figure 5.3* suggests that, when clusters form on an HX surface, a higher cluster-surface interfacial tension exists as the surface free energy rises. The high surface energy increases the wetting by the forming clusters, hence reducing the ΔG_{crit} for heterogeneous nucleation. The reduction in ΔG_{crit} as the surface free energy of a material increases resulted in shorter scaling induction times. However, this deduction is inconclusive, as there was no way of observing nucleation clusters in this study. However, theoretically, the observation supports the hypothesis that the increased wettability due to high surface free energy, results in shorter induction times.

When the Brass plate was used, the second longest induction time was recorded. This induction time can be associated with the low surface free energy of the material. In addition, the low surface free energy decreased the wettability of the HX surface, thereby increasing the Gibbs free energy for nucleation. The decrease in wettability might have reduced the viscous drag at the liquid-HX surface interface. In support of this deduction, the Brass HX plate attained the highest bulk and near-surface supersaturations. The longer scaling induction times and higher supersaturations attained when using the Brass HX plate may have resulted in a higher number of stable critical nuclei in both the bulk solution and at the liquid-HX surface interface. The occurrence of both bulk and heterogenous nucleation supports this postulation. Therefore, with the Brass HX plate, the combination of higher bulk supersaturation and the low surface energy of the material increased the probability of bulk crystallization prior to scaling and lengthened the scaling induction time, which supports the hypothesis regarding the effect of surface free energy.

The longest scaling induction time was recorded when using the Aluminium plate. However, Aluminium has a higher surface free energy than SS316 and Brass HX plates. Therefore, it became evident that another material property, apart from surface energy, was the cause of the extended scaling induction time. An analysis of the surface topography of all the materials used in this study showed the Aluminium plate to have the smoothest topography (R_q of 18.5 nm). The Aluminium surface topography did not exhibit any crevices which could have created the regions of local supersaturations, nor peaks for sites for adhesion (*Appendix A.2*). A study conducted by Heydari et al. (2016) reported that smoother surfaces were more efficient in increasing the scaling induction time than rougher surfaces. Smoother surfaces minimised the area available for contact with the solution, which in turn reduces the wettability of the HX surface. The near-surface supersaturation supported this deduction as it was the highest after that recorded on the Brass HX plate. Therefore, a smoother surface increases the free energy barrier for nucleation to occur, by minimising the contact area that it provides to the crystallizing material.

The SS316 HX plate resulted in the second-shortest scaling induction time and the lowest level of supersaturation. This result emphasised the effect of surface topography on scaling since the SS316 exhibited the roughest topography of all the materials. The inherent crevices on the SS316 surface allowed the development of high levels of local supersaturation, which allowed nucleation to initiate at lower supersaturations. Overall, the experimental results showed that surface free energy on its own did not alter the wettability of the HX surface. The surface topography also played a crucial role in increasing the HX surface wettability of the materials, by providing an increased solution-HX surface area, which in turn, shortened the scaling induction time.

Therefore, it was deduced that materials of lower surface energies delayed scaling in an EFC process, as indicated by the longer scaling induction time. The higher supersaturations attained when using low surface energy materials resulted in increased probabilities for bulk nucleation. A smooth surface delayed heterogeneous nucleation of ice, due to reduced sites that enhance the initiation of nucleation. Consequently, smooth HX surfaces with low surface free energy have the potential to increase the scaling induction time in the EFC system and hence delay the onset of scaling.

To further decouple the effect of surface energy from topography, SS316 (which is the most widely used material in the industry) was coated with *polytetrafluoroethylene* (PTFE). This coating has the lowest surface free energy, meaning it is hydrophobic. The effect of surface energy was investigated at different coolant temperatures, to investigate the extent to which the hydrophobic surface remained efficient at delaying heterogeneous nucleation (*Figure 5.4*).

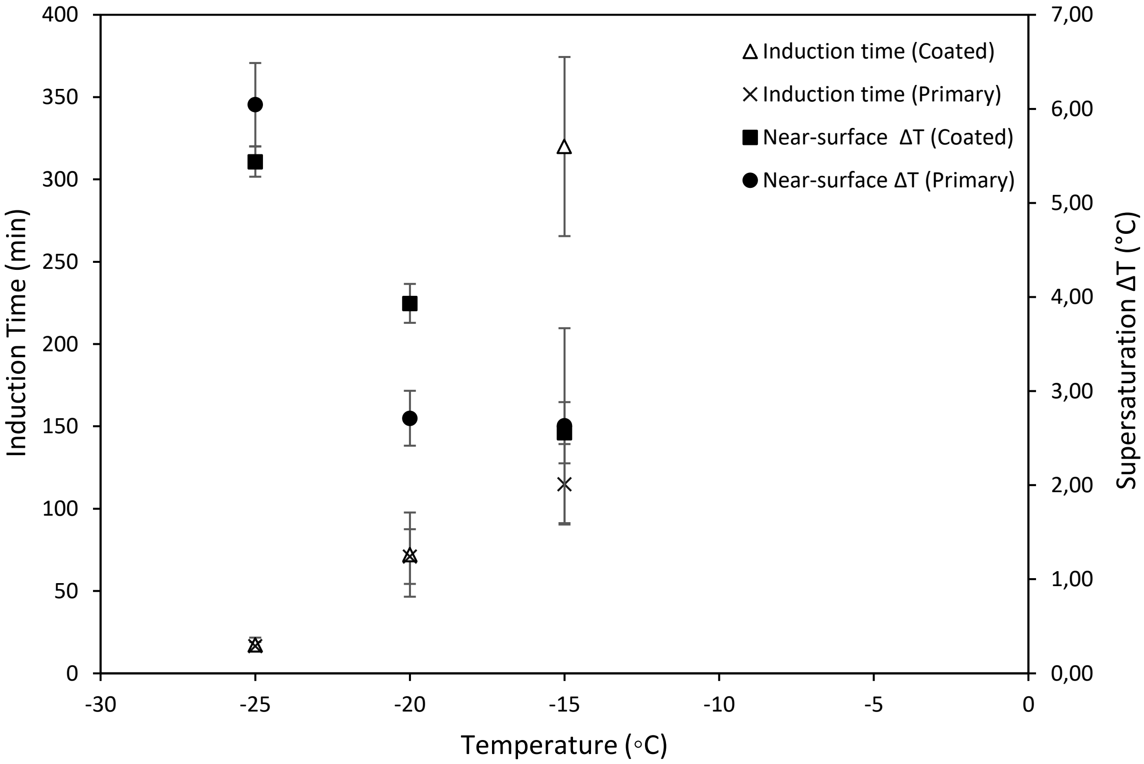

Figure 5.4*: Effect of surface free energy on the scaling induction times (open markers) and the near-surface supersaturation (solid markers) for primary and PTFE coated-SS316, at different coolant temperatures.*

Figure 5.4 shows the differences in the scaling induction times for the primary-SS316 and PTFE coated-SS316 materials, at different coolant temperatures. Overall, the scaling induction time increased with an increase in the coolant set temperature when operating with either HX surface. The only difference in the recorded induction times between the coated surface and the primary surface was observed when operating at -15°C. As the system cooling rate decreased, differences in the recorded scaling induction times were not observed for both surfaces.

Overall, the supersaturations attained, increased with an increase in the cooling rate on both HX surfaces. Yet again, the results in this set of experiments were contrary to the work by Gutwald and Mersmann (1990), who showed that for higher cooling rates, the supersaturation maxima results in higher values within the bulk. According to Lewis et al. (2010), this is due to an increase in the the average metastable zone width (MSZW) for the region where ice forms when the cooling rate is faster. However, these deductions were not based on crystallization on the HX surface, which indicated that the cooled HX surface provides a template which decreases the Gibbs free energy for nucleation. Therefore, in the presence of the cooled HX surface, a faster cooling rate has been found to reduce the required level of supersaturation for scaling to occur.

At -15°C, the ice scaling induction time recorded when using the coated-SS316 was 2.79 times longer than that of the primary HX plate, even though the supersaturations levels reached were similar. This result indicated that the PTFE coated HX plate delayed the onset of scaling at lower cooling rates, while still achieving the supersaturations similar to that of the primary-SS316. A hydrophobic surface is known to reduce the frictional drag at the interface. Although the fluid dynamics were not in the scope of this study, it is important to highlight the possible influence of the reduced drag on the scaling induction time. Yang et al. (2002) and Tourkine et al. (2009) demonstrated that the frictional drag at the interface was reduced on a low surface free energy material, which increased the scaling induction time. Therefore, the lower frictional drag on the PTFE coated surface could have contributed to the prolonged scaling induction time at -15°C.

When the coolant temperature was operated at -25°C, there was no observable difference in the scaling induction times for either the primary or the coated-SS316 surface, although the supersaturations levels attained differed. According to Yin et al. (2010), the wettability at the interface increased with a lower cooling temperature. Therefore, the efficiency of hydrophobic surfaces in delaying the onset of heterogenous nucleation declined at higher levels of supersaturation. This drop implied that there was a limitation to the extent in which a hydrophobic surface could increase the scaling induction time.

In addition, the higher supersaturation attained with the PTFE coated-SS316 surface showed that there was a higher energy barrier for heterogenous nucleation to occur. This finding corroborated well with the work by Carpenter and Bahadur (2015), where a brine solution reached lower temperatures when cooled using a PTFE coated plate than with an Aluminium plate. Furthermore, similar findings were reported Qin et al. (2003), who reported that heterogeneous ice nucleation on a PTFE coated-SS316 occurred at lower nucleation temperatures than with the bare Stainless Steel, at similar operating conditions. This difference might have been caused by the drag reduction on the coated surface. Therefore, with less drag at the interface, the low surface free energy material minimised the contact time between the solution and HX surface, thereby enhancing the heat transfer within the system.

However, at -20°C, the ice scaling induction times for both the primary and PTFE coated HX plates were similar. This finding was contrary to what Qin et al. (2003) found, as they recorded longer induction times with the PTFE coated HX surface. The reason for this contradictory result was not apparent, but a possible explanation would be warmer cooling temperatures used by Qin et al. (2003). For instance, the cooling plate was kept at -5°C when cooling the whole milk solution. Therefore, it could be possible that when operating at lower cooling temperatures, the benefit of using a hydrophobic HX plate diminishes.

At a coolant temperature of -25°C, the ice scaling induction times decreased and were similar for both surfaces. This observation indicated that as the cooling rates increased, a point was reached where there was no apparent difference in the scaling induction times as a function of surface properties. The surface properties appeared to affect the supersaturations at nucleation, but not the time that was taken to reach the supersaturation. The supersaturations attained at this coolant temperature were higher for the primary surface than for the PTFE coated surface. The only significant difference observed at this coolant temperature was the evolution of needle salt crystals when the primary material was used. Needle-type morphology indicated environments of high supersaturation.

In conclusion, the results obtained indicated that using a low surface energy HX surface increased the scaling induction time only at -15 °C, which indicated that it depended on the cooling rate of the system. In addition, using a low surface energy material resulted in higher supersaturations at lower cooling rates. It was therefore beneficial to use a low surface energy material at low cooling rates in order to realise its benefits.

5.2.2. Ice scaling modes on different HX materials

Heterogenous nucleation was characterised by the random appearance of ice islands on the HX plate, indicating areas where nucleation started. The images below show the scaling process at the macroscopic level, and thus the actual birth of the crystal was not visible. The microscopic nuclei grew into macroscopic crystal structures which were referred to as “ice islands”. The predominance of either heterogeneous nucleation or growth indicated the ice scaling mode on the particular surface. The scaling mode later affected the crystallization kinetics on the HX surfaces.

5.2.2.1. Ice scaling modes on different metal plates at a coolant temperature of -20°C

In these experiments, heterogenous nucleation started on the HX plates, except for Brass and Aluminium where cases of bulk nucleation were observed. In general, heterogeneous nucleation on all the HX materials occurred randomly, with no specific region initiating the nucleation process. The modes of scaling on the HX surfaces differed, and they are shown in *Figure 5.5* to *Figure 5.8.*

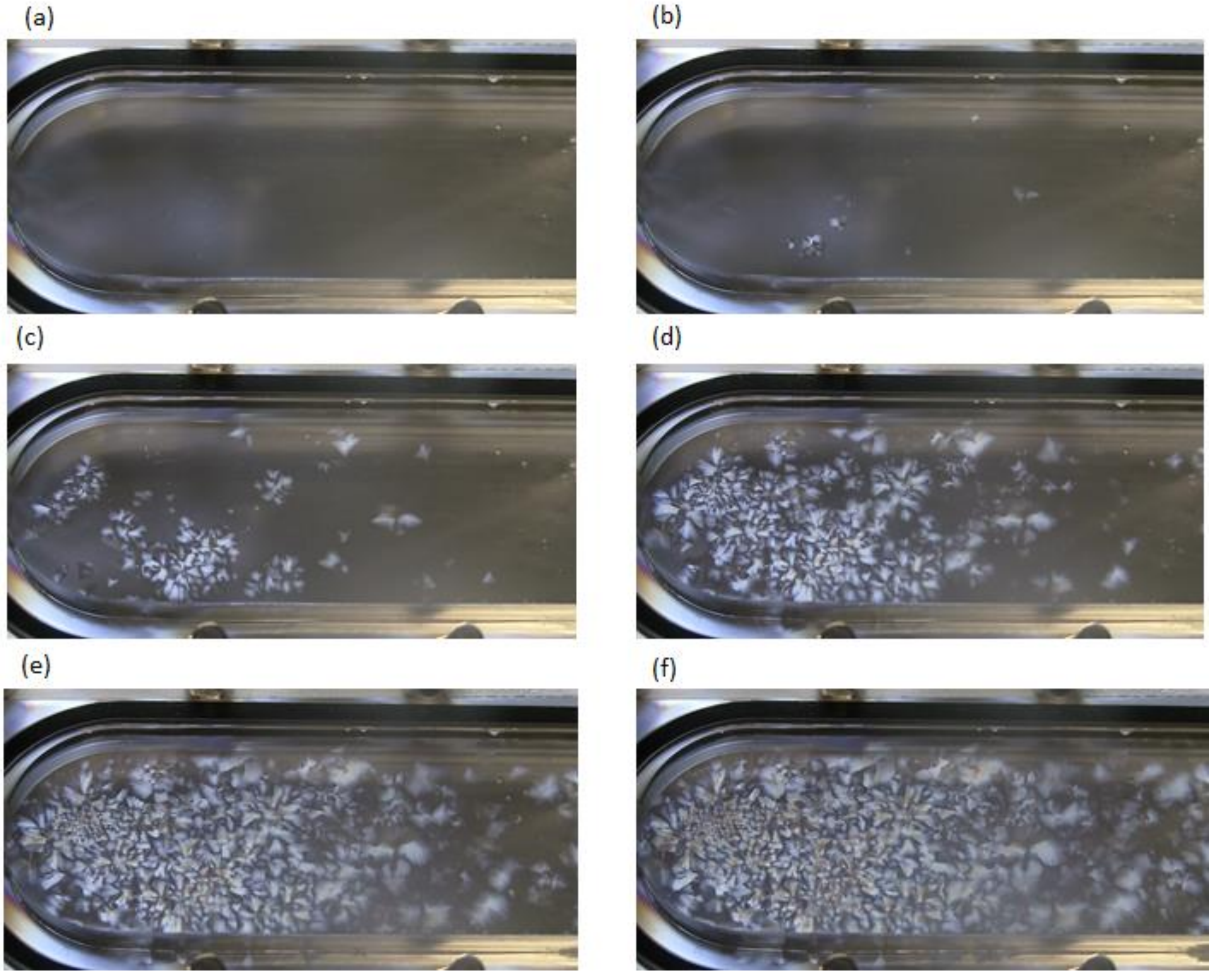

Figure 5.5: *DIC photographs of ice scale formation on primary-SS316 where (a) is the frame before a first visible nucleation site is detected at 0s and frames (b) to (f) are 0.4s, 0.8s, 1,2s, 1.6s and 2s after detectable nucleation sites were observed.*

Figure 5.5 (a) shows the SS316 surface before nucleation, where the fluid was in constant flow and continuously cooled down. In frame (b), grey-white islands indicated the growing ice which nucleated heterogeneously. The subsequent frames show the continued crystallization on the SS316 surface, through nucleation with minimal horizontal and vertical growth. Of all the metals used, the SS316 surface was the most densely populated with ice nucleation islands. The crevices (which increased the quiescent regions of high local supersaturation) contributed to the high number of nucleation sites observed on the SS316 plate.

The morphology of ice scale was poorly defined because of the thin ice, which had a maximum thickness of approximately 125 nm according to the Michael-Lévy plot (Delly, 2012). The thinner ice layer can be attributed to the lower level of supersaturation (2.68 °C), compared to those reached by the other HX materials. Kapembwa et al. (2014) reported that vertical growth rate was relatively low at these supersaturations, this occurring predominantly through layered growth. Li et al. (2016) showed that at low supersaturations, the spiral growth was the primary growth mechanism. Therefore, each nucleation island may have grown through the spiral growth mechanism, and this resulted in a slower vertical growth rate of the ice islands.

With continued horizontal growth, the ice islands either retained the initial shape or became irregular. The change in shape was as a result of horizontal growth, as the ice consumes the available supersaturation and the nucleation of new sites near the already growing nucleation site. These nucleation islands merged; however, the domain boundaries formed between the ice islands were not distinct because the ice layer was very thin. The observations confirmed the hypothesis by Vaessen et al. (2002) stating that the inefficiency of scraping may have been due to the presence of a thin persisting ice layer on the SS316 HX surface, which was not reached by rigid scrapers as revealed by (Martínez et al., 2014). The presence of the domain boundaries suggested that the initial ice layer formed on the SS316 might be easily subjected to a cohesive fracture when scraping. Therefore, scraping ice from SS316 always results in a higher number of residual ice crystals on the HX surface, which may serve as sites for continued growth as observed in the study by Matsumoto et al. (2010).

Figure 5.6 shows scaling on a Brass HX surface. The horizontal growth occurred uniformly from the centre of the island, spreading out radially. All the sites displayed similar surface morphologies, with a radial, dendritic outgrowth which merged to cover the entire surface (frames d and e). The visible black areas between the ice islands indicated regions of the thinner ice layer (Delly, 2012). The consumption of supersaturation could have caused these regions, and the released heat of crystallization may have limited vertical growth of the ice layer in these areas.

Frame (d) shows a change in the ice scale layer. This colour change started at the ice islands that formed earlier in the scaling process. Delly (2012) mentioned that the retardation, i.e., the difference in the distance travelled by the n^O and n^E rays as they pass through the ice, increases linearly with the thickness of the specimen. Therefore, change in colour from white to deep orange indicated a change in retardation was due to vertical growth of the ice scale layer. The thickness of the ice layer was nonuniform across the HX plate. However, the maximum thickness was approximately 190-200 nm (Delly, 2012). The colour changes suggested the co-existence of horizontal and vertical growth of the ice layer.

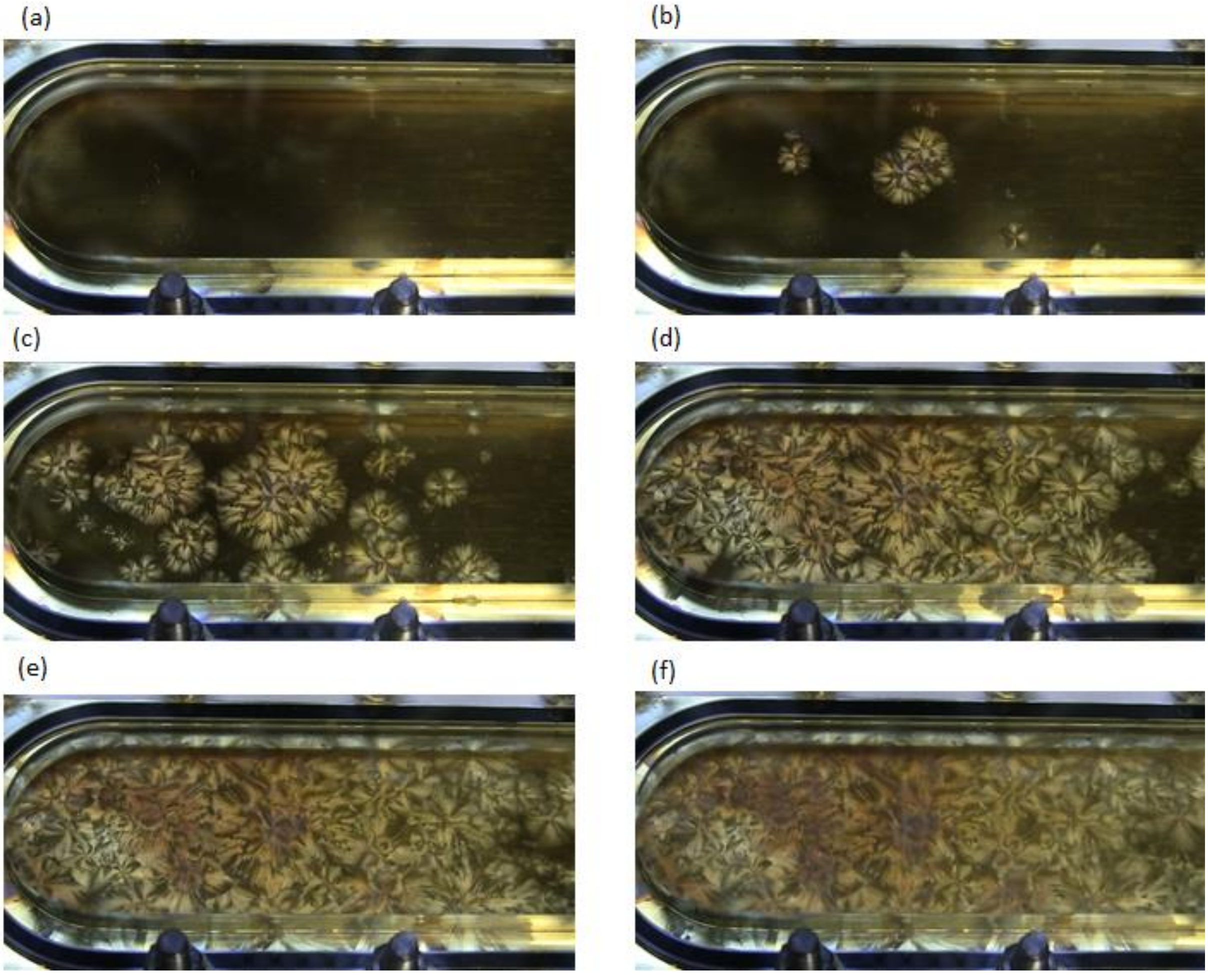

***Figure 5.6**: DIC photographs of ice scale formation on Brass where (a) is the frame before a first visible nucleation site is detected and frames (b) to (f) are 0.4s, 0.8s, 1,2s, 1.6s and 2s after detectable nucleation sites were observed.*

The highest level of bulk and near-surface supersaturations (ΔT_{bulk} of 1.52°C and $\Delta T_{HX\text{-}surface}$ of 4.76°C), was reached with the Brass HX plate. According to Kapembwa et al. (2014), the supersaturations approximating 2.8 °C, resulted in higher vertical ice scale growth with a dominant dendritic-like growth mechanism. The rapid, vertical dendritic growth may have resulted in a sparse ice scale structure at the ice-solution interface, as indicated by Matsumoto et al. (2010). Lewis et al. (2015) stated such a sparse structure was highly susceptible to shearing by the flowing bulk fluid, resulting in the detachment of weak dendritic or polycrystalline outgrowths. The outgrowths are introduced into the bulk, resulting in dendritic or polycrystalline breeding. This process reduced the activation energy for nucleation, resulting in the observed bulk ice crystallization when using the Brass HX plate.

The cloudiness indicated secondary bulk nucleation in the bulk solution (frame f). Simultaneously, the cloudy region became denser (indicated by the developing white patches) at the deep orange regions (areas of greatest ice scale thickness). The white patches developing on the orange regions of the ice scale indicated that the vertically growing ice scale layer provided sites for bulk ice adhesion, which began at the highest point of the scale layer (frames d, e and f). This growth pattern indicated the tendency for ice to adhere to available peaks at the surface.

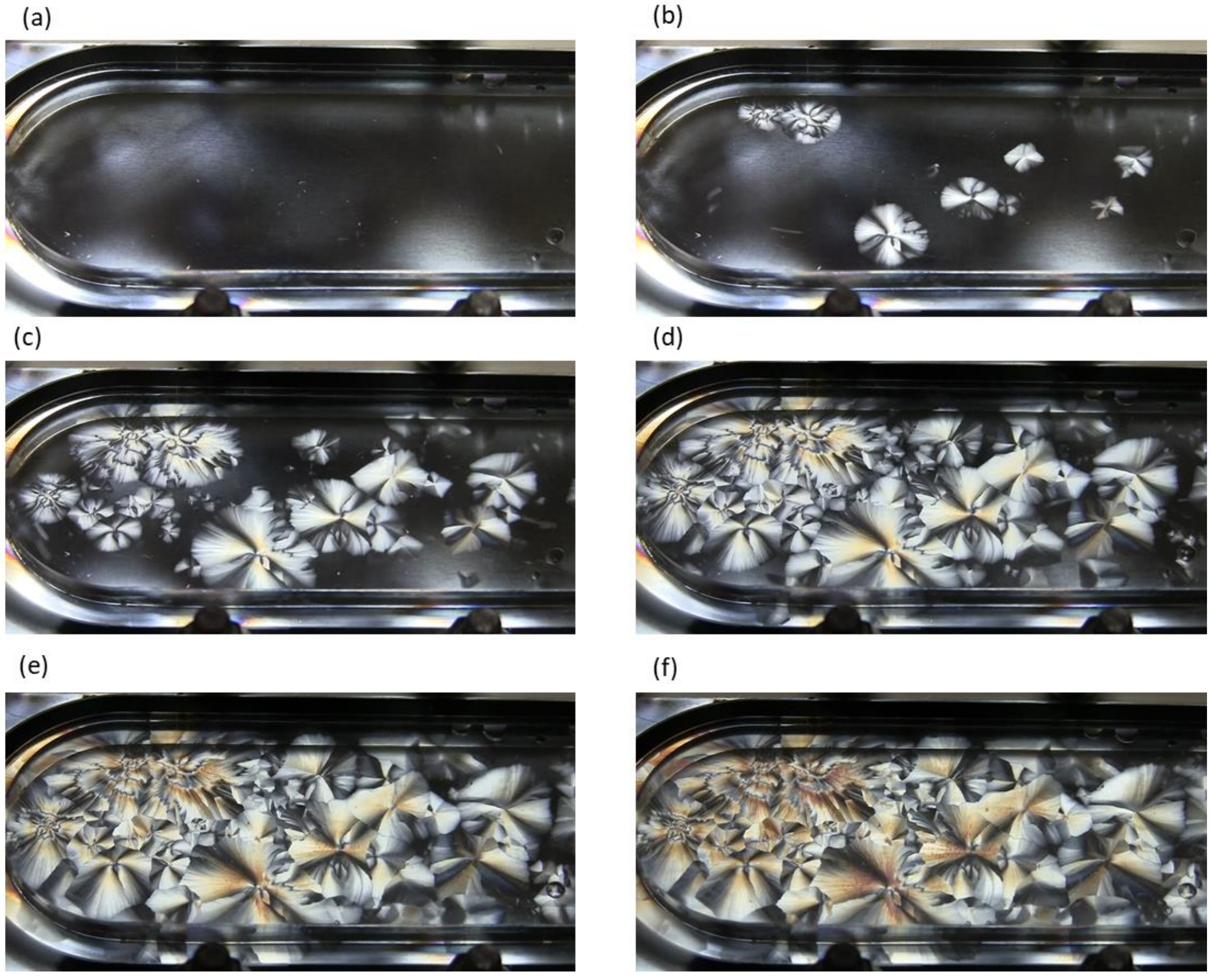

***Figure 5.7**: DIC photographs of ice scale formation on Aluminium where (a) is the frame before the first visible nucleation site is detected and frames (b) to (f) are 0.4s, 0.8s, 1,2s, 1.6s and 2s after detectable nucleation sites were observed.*

Figure 5.7 shows the formation of the initial ice scale layer on the Aluminium plate. In frame (a), small particles were already observed in the bulk solution. These were bulk salt crystals as there was no significant temperature increase in the system, which would have indicated the heat of crystallization of ice. After the heterogeneous nucleation of ice, there was an immediate increase in the presence of bulk crystals. According to Kapembwa et al. (2014), ice scale growth at a $\Delta T_{HX\text{-surface}}$ of 3.96°C occurred through dendritic growth mechanism. The dendritically growing scale ice layer was sheared, resulting in bulk crystals, as happened the with the Brass HX plate. However, the shearing of the islands occurred earlier in the scaling process than when Brass was used.

The early shearing of the ice islands resulted in the secondary contact nucleation, which was indicated by the newly formed nucleation sites in the vicinity of the larger ice islands. These new smaller sites are visible from frame (c). The growth of these newly formed islands was limited by the presence of larger ice islands in their vicinity, which created an environment of "competition" for supersaturation among the growing crystals. With more crystals in the vicinity, the available supersaturation for growth was reduced.

In frame (d), the larger and smaller ice islands merged. Once the ice islands merged, a distinct merger line formed, indicating the domain boundaries within the newly formed ice scale layer (Thürmer and Bartelt, 2008). In frames (c) to (f), a brown-yellow colour was observed on the growing ice scale layer. The change in the colour pattern indicated the change in thickness of the growing ice scale layer, growing normal to the HX plate (Delly, 2012). This colour intensified with time into a deep orange to red, with a maximum thickness of approximately 190-200 nm, while the black-grey-white regions indicated a thickness ranging between 25 and 80 nm (Delly, 2012).

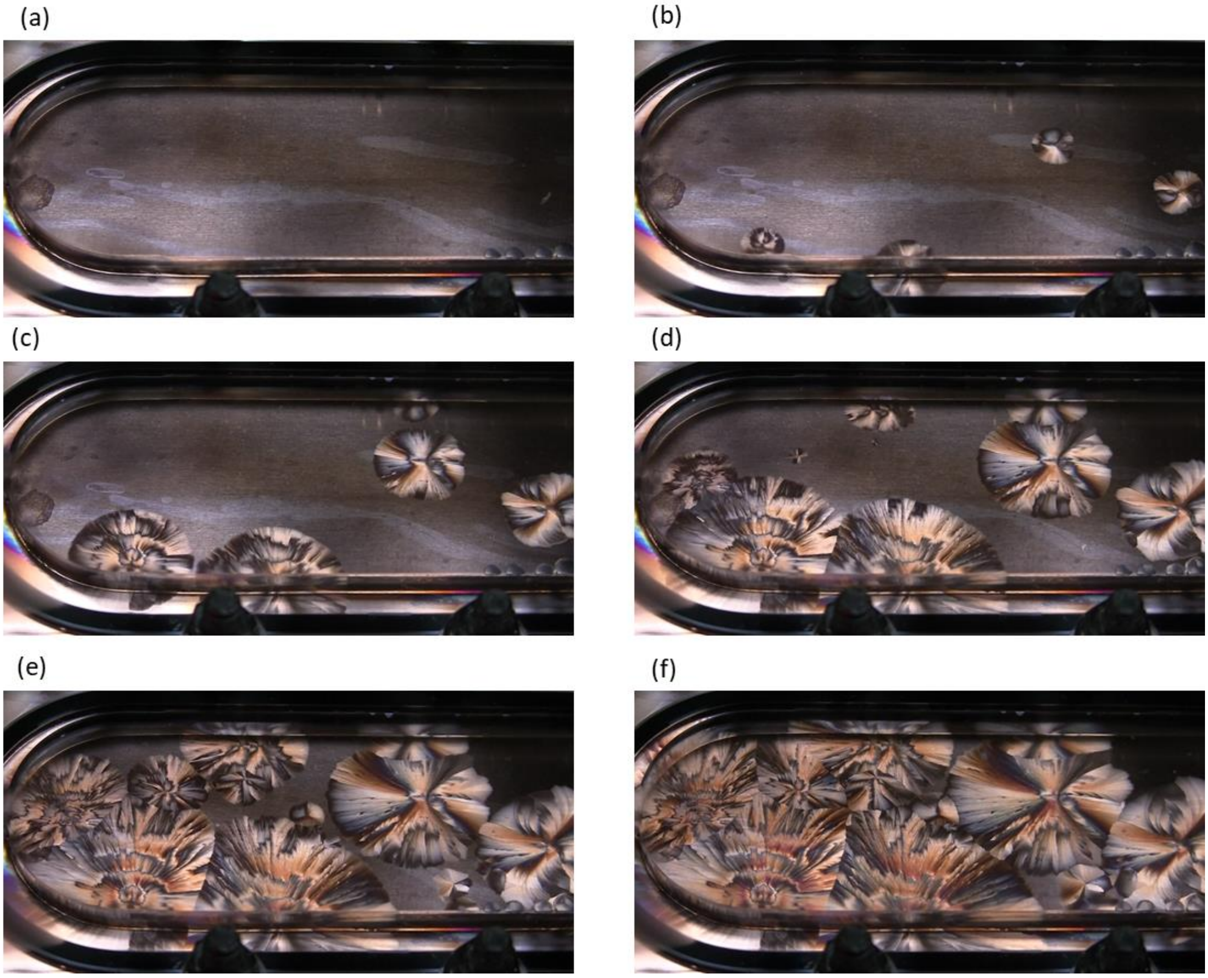

Figure 5.8: *DIC photographs of ice scale formation on Copper where (a) is the frame before the first visible nucleation site is detected and frames (b) to (f) are 0.4s, 0.8s, 1,2s, 1.6s and 2s after detectable nucleation sites were observed.*

Figure 5.8 shows the progression of nucleation on the Copper surface. Frame (a) indicates the test cell prior to nucleation, followed by frame (b) where four nucleation islands had developed. Copper exhibited the fewest heterogeneously formed nucleation sites of all the surfaces tested. Nucleation was primarily on the surface throughout the 6 frames, and no bulk nucleation was observed during the two seconds indicated by the extracted frames.

After two seconds, the Copper HX surface still had regions which were unscaled. This result was attributed to the short scaling induction times, in addition to the low level of supersaturation reached when the Copper HX plate was used (*Figure 5.2*). The nucleation sites were the least densely populated compared to those which occurred on the SS316, Brass and Aluminium HX surfaces. Sparser nucleation sites may indicate that the use of a higher surface free energy material like Copper, minimised the free energy for nucleation. Therefore, the unstable nuclei of a subcritical size may have nucleated at lower supersaturations. The short scaling induction times possibly resulted in fewer nuclei with a size which encouraged heterogeneous nucleation on the Copper HX plate.

A reduced number of nucleation sites on the Copper HX enhanced horizontal growth due to the minimal competition for the available supersaturation. The growing ice layer consisted of clustered needles radiating from the nucleation centres, forming steps and terraces on the surface of the growing ice layer. As growth continued, the colours changed from black to grey, white, orange, and finally deep red. This suggested growth of the ice nucleation sites normal to the surface, while simultaneously growing parallel to the surface.

The red colour only appeared during cooling the solution with the Copper HX plate, indicating that it had the highest vertical growth of a nucleation site of all metals used. This vertical growth occurred as a result of the efficient removal of the heat of crystallization as the ice layer continued to grow. Kapembwa et al. (2014) showed that the heat of crystallization diffused into both the bulk solution (3-16 %) and the solid ice layer (84-97 %). Therefore, the enhanced vertical growth occurring on the Copper HX plate was correlated with its higher thermal conductivity, resulting in an increased transfer of the heat of crystallization from the developing ice layer.

Overall, the ice scaling modes showed the nucleation and growth patterns of the initial ice scale layer that has been problematic in scraped crystallizers. The different HX surface properties influence whether scaling is nucleation or growth dominated, which affects the number of domain boundaries, and thus, the cohesive strength of this ice layer. The influence of the HX surface on the structure of the ice scale layer could indicate whether the ice scale results in cohesive or adhesive breaks when subjected to scraping. Therefore, this study has shown that the use of different HX materials may also impact the behaviour of ice upon scraping, in addition to the effect of temperature and supersaturation, as indicated by Matsumoto et al. (2010).

From the domain boundaries formed within the structure of initial ice scale layer, it can be postulated that cohesive breaks of the ice scale layer were more likely to occur on the HX surfaces in the following order SS316, Aluminium, Brass and lastly Copper. The higher nucleation sites formed on the HX plate resulted in an increased density of domain boundaries as observed on SS316. The domain boundaries created imperfections on the growing ice layer, which may reduce the force required for cohesive breaks. For ice scale forming in the Copper HX plate, the scaling mode was predominantly through growth with minimal nucleation. Therefore, the cohesive strength of the growing ice layer would be higher than the ice layer strength on the other metals used in this investigation. The low number of domain boundaries formed on this surface may result in an adhesive fracture. However, the adhesive strength is higher on a surface of higher surface free energy due to the increased interfacial tension at the solution-HX surface interface.

Therefore, it is crucial to consider the adhesive bonds which strengthen with the increase in surface free energy of the material. Ozbay and Erbil (2016) indicated that the adhesion strength of ice on metal surfaces decreases in the following order Copper > SS316 > Aluminium >> PTFE. Although Brass was not included in their study, the adhesion strength dropped with the decrease in surface free energy. Based on this trend, the Brass plate would be ranked between Aluminium and PTFE materials. This order shows that when using the Copper HX plate, adhesive bonds would be higher than those for the other metals, because of its higher surface free energy. Therefore, the use of the material with high surface free energy may result in an initial ice scale layer dominated by high cohesive and adhesive strength and this would require greater force for ice scale removal during scraping.

5.2.2.2. Ice scaling modes on different metal plates at similar heat fluxes

Scaling at similar heat fluxes occurred predominantly through heterogeneous nucleation or growth, and in some cases through a balance of both scaling modes. The difference observed when the system was operated at similar heat fluxes with different metals, was the presence of a substantial volume of salt crystals. These $Na_2SO_4{\cdot}H_2O$ crystals nucleated in the bulk, prior to the crystallization of ice. The salt crystals are the small shiny particles seen in *Figure 5.9*. These bulk salt crystals caused a noticeable blur in the images not seen in the previous *Figure 5.6* to *Figure 5.8,* where no significant salt particles were observed before heterogeneous nucleation. According to Lewis et al. (2010), the metastable zone width of $Na_2SO_4{\cdot}10H_2O$ salt is smaller than that of ice at a similar cooling rate. Therefore, the salt was likely to crystalize before the ice at warmer coolant temperatures.

The shiny particles observed in all the frames were due to the light reflected by the salt crystals growing in the flowing bulk solution, and near the HX plate. The salt crystals that were closer to the surface of the HX plate moved slowly in random directions, resembling Brownian motion. The salt crystals in the bulk fluid moved faster in the direction of the bulk fluid motion, as indicated by the cloudiness of the bulk. This difference in salt crystal movement suggests that there could have been two distinct regions within the solution in the test cell. Although it was not analysed in this study, the region where the salt crystals showed slow Brownian motion could have been caused by the existence of the velocity boundary layer.

The salt particles near the HX wall grew into large solid plate-like crystals and some agglomerated to form larger crystals. When these crystals became too large to remain in the slower-moving region, they were swept out into the fast-flowing bulk solution. This observation corroborates the study by Förster and Bohnet, (1999), who showed that ions entered the laminar boundary layer and left as crystals into the flowing bulk. In this set of experiments, the salt crystals did not result in any scaling of the HX surface, as they remained in Brownian motion until heterogeneous ice nucleation started on the HX surface. The salt crystals were incorporated into the ice scale layer as it grew across the HX surface.

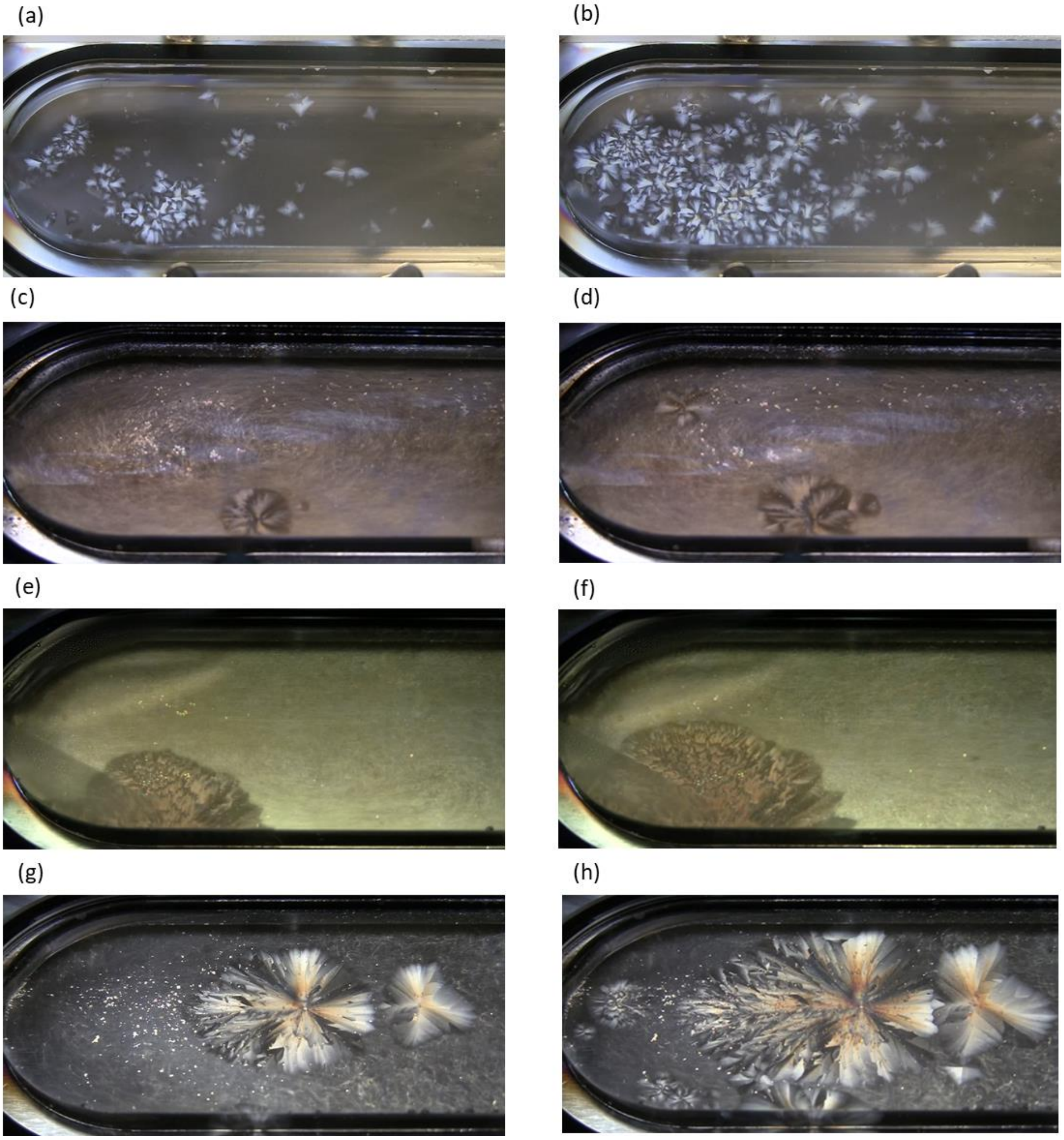

Figure 5.9: *DIC photographs of ice scale formation on SS316 (a-b), Copper (b-c), Brass (e-f), and Aluminium (g-h) at similar heat fluxes, at 0.8s and 1.2s after heterogeneous nucleation of ice occurred.*

The different materials showed a difference in ice scaling, even though the cooling rate was the same. Scaling on the Copper HX plate remained growth dominated with minimal nucleation, similar to when cooling at -20 °C. With the Brass HX plate, instances of bulk nucleation were observed (*Figure A.15*). The lower surface energy of the Brass plate decreased the probability of 2D nucleation onto the surface of this material. After the formation of the bulk ice crystals, the formation of a white layer was observed on the surface. This white layer was attributed to the adhesion of the bulk ice particles which accumulated, which resulted in scaling by adhesion of ice. A white layer grew radially from one point, covering the entire surface.

In the instances when ice nucleation occurred on the Brass HX surface, it started where the Perspex glass was in contact with the metal plate. Any solution which entered this area became stagnant, which increased the contact time at the liquid-solid interface. The increased contact time resulted in high local supersaturation, which led to the early heterogeneous nucleation of ice. If such stagnant regions could be avoided in a crystallizer, longer induction times could be reached in addition to increased probabilities for bulk ice nucleation.

Scaling on the Aluminium HX plate was initially growth dominated, with an increase in nucleation later in the scaling process. These observations indicated that the scaling modes did not significantly change when operating at similar heat fluxes, which may suggest that crystallization of ice to form a scale layer was, to some degree, affected by the HX surface properties.

5.2.2.3. Ice scaling modes on the Primary-SS316 and PTFE coated-SS316

The scaling modes on the PTFE coated-SS316 (low surface free energy) and the primary-SS316 materials (higher surface free energy) were investigated. The differences in the scaling modes are indicated in *Figure 5.10*.

(a- Primary SS316 at -15°)

(b- Coated-SS316 at -15°)

(c Primary SS316 at -20°)

(d- Coated-SS316 at -20°)

(e- Primary-SS316 at -25°)

(f- Coated-SS316 at -25°)

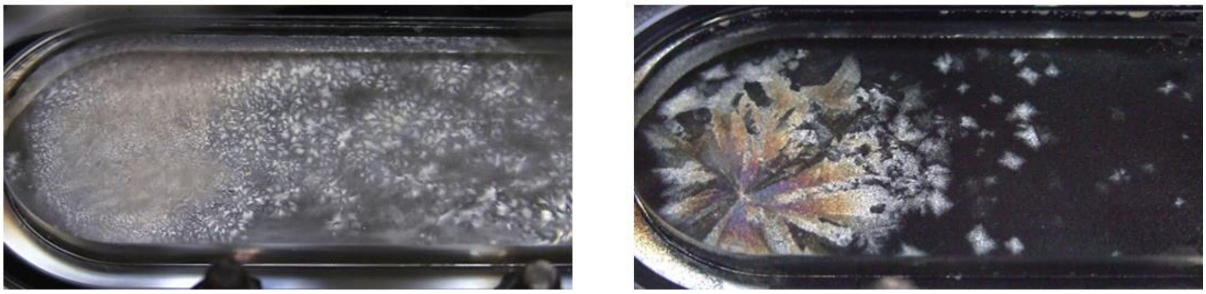

Figure 5.10: *Comparison between the ice scaling modes on the Primary (a, c, and e) and PTFE coated-SS316 (b, d, and f) 2s after the commencement of heterogeneous nucleation. Frames (a and b) show the process at -15°C, frames (c and d) show the process at -20°C and frames (e and f) show the process at -25°C.*

Figure 5.10 shows the difference in the scaling modes on the primary-SS316 and the PTFE coated-SS316 when operating at coolant temperatures of -15 °C, -20 °C and -25 °C. When operating at a constant coolant temperature of -15 °C, there was a high mass of salt present when using both the primary and coated-SS316 HX plates. The increased bulk salt crystallization was prevalent when operating at lower cooling rates.

Therefore, despite the increase in the scaling induction time (*Figure 5.4*), the inherently high surface roughness of the PTFE coated-SS316 promoted adhesion of the crystallized salt crystals, leading to severe salt scaling despite its low surface free energy. This observation is similar to the work by Förster and Bohnet (1999), who showed that salt scaling through adhesion was more pronounced on PTFE than on the Stainless Steel surface. Adhesion of bulk crystals on to the PTFE coated HX plate was attributed to the larger roughness height and width of the PTFE surface (*Figure A.5*).

Despite the unexpected high $Na_2SO_4 \cdot 10H_2O$ deposition on the PTFE coated-SS316, the adhered salt crystals were at times dislodged from the surface by the flowing bulk fluid. Therefore, the force required to remove the salt scale that formed on the PTFE coated surface would be lower than that required to do so from the primary-SS316 surface of similar topography. The dislodging of the salt scale from the surface is supported by MacAdam and Parsons (2004), who found that the lower surface energy of the HX material resulted in lower adhesion strength of $CaCO_3$ salt scale. They and other researchers reported that more force was required to remove ice or salt scale deposit from a rough surface than from a smoother or low surface free energy HX surface (Keysar et al., 1994; Förster & Bohnet, 1999; Zou et al., 2011; Sojoudi et al., 2019).

The ice scaling mode on the PTFE coated-SS316 surface resulted predominantly from growth within the salt scaled regions. The ice scale was only visible on the areas where salt adhered (*Figure 5.10* (*b*)). If there was ice scale on the HX surface in *Figure 5.10 (b)*, then the resultant retardation produced a black interference colour. According to the Michael-Lévy plot, the black interference colour indicated the ice layer thickness of 20 nm or less. That is, the growth of the ice layer on the PTFE coated surface was less compared to the other surfaces.

At the operating temperature of -20 °C, numerous nucleation sites initiated on both the primary and PTFE coated HX surfaces. However, the ice had not completely covered the PTFE coated HX plate when bulk nucleation occurred (*Figure 5.10* (*d*)). This may be an indication that when nucleation took place, growth predominated vertically on the already formed ice islands. The flowing bulk solution may have sheared the dendritically growing ice faces, which in turn initiated bulk ice nucleation before scaling over the entire surface.

When operating at -25 °C and using the coated surface, the ice scaling became slower in comparison to the primary surface. The change in retardation, indicated by the resultant interference colours, was observed as the thickness of the ice scale increased on both surfaces. As the ice scale layer grew on the coated-SS316 surface, its colour changed from grey, then to white, orange, to the deep reds, which ultimately became indigo *Figure 5.10* (*f*). When using the primary-SS316, the predominant interference colour observed was white. The analysis of the colour changes on the ice scale growing on the PTFE coated- SS316 surface showed that the vertical ice scale growth was enhanced on the pre-existing ice islands, as opposed to the observations on the primary-SS316.

The observed colour changes indicated that the thickness of the ice scale increased faster on the PTFE coated-SS316 than on the primary-SS316. These colour changes may be an indication of the tendency of the ice layer to continuously grow on the pre-existing ice islands as opposed to on the PTFE coated-SS316. In addition, the ice scale growth mode on the PTFE coated-SS316 could have undergone an "off-surface" growth mode as opposed to "along-surface" growth mode, as illustrated by Liu et al. (2017). The "off-surface" growth mode occurred on low surface free energy HX surface (PTFE coated-SS316), whereas the "along-surface" growth evolved as a result of the higher free energy HX surface (primary-SS316). This growth pattern may be the reason why some areas of the coated–SS316 surface depicted in *Figure 5.10* (*f*), remained unscaled before bulk crystallization, while the larger surface area was scaled at the point of bulk nucleation with the primary-SS316 (*Figure 5.10* (*e*)).

The observed scaling modes indicated that the inherent rougher topography limited the efficiency of the PTFE coated surface in reducing scaling of both ice and salt. However, there was less horizontal growth of ice scale on the PTFE coated HX plate relative to the primary-SS316. The reduced horizontal scaling rate may be beneficial when scraping. Lower scraping rates would be required, in addition to reduced scraping force, in order to remove the ice scale layer.

5.2.3. Effect of surface free energy on the crystallization kinetics of the ice scale layer

The qualitative data above allowed the evaluation of the scaling modes, which evolved with the different HX plates. Quantitative data was extracted from these frames with time, in order to obtain the overall scaling rates. The following section provides the analysis and interpretation of the quantitative data to understand the effect of different materials on the scaling rate when operating at similar heat flux.

5.2.3.1. Nucleation and growth rates on different metals at similar heat fluxes

Real-time analysis of the developing ice scale allowed the tracking of the coverage over the metal surface through both heterogeneous nucleation and horizontal growth rates at similar heat fluxes *(Figure 5.11*). The average in growth rates in *Figure 5.11* represents the growth for the heterogeneously nucleated 2D ice, which was measured in terms of the surface area covered per second. The measured growth rate was that of the growth normal to the smallest crystal growth face, thus the face growing parallel to the HX plate.

Figure 5.11 shows the relationship between nucleation and subsequent growth rates of ice scale on different HX materials when operating at similar heat flux. The HX materials are listed in ascending order of their surface free energies. The nucleation and growth rates differed when using different HX materials and operating at similar heat fluxes. The interdependency of the rates of nucleation and growth is evident in *Figure 5.11.* The general observation was that a higher nucleation rate resulted in lower subsequent growth rate, and vice versa. The nucleation rate was highest on the SS316, followed by Aluminium, then Brass, and lastly, the lowest nucleation rate was observed on the Copper HX plate. Interestingly, nucleation rates were reduced when using HX material of higher surface free energy, such as the Copper HX plate. This result can be explained by the shorter scaling induction times and low levels of supersaturation. The subsequent growth rates were highest for Copper, followed by Brass, then Aluminium and lastly SS316. These rates could have been caused by the diminishing available supersaturation when there were more ice islands on the HX surface.

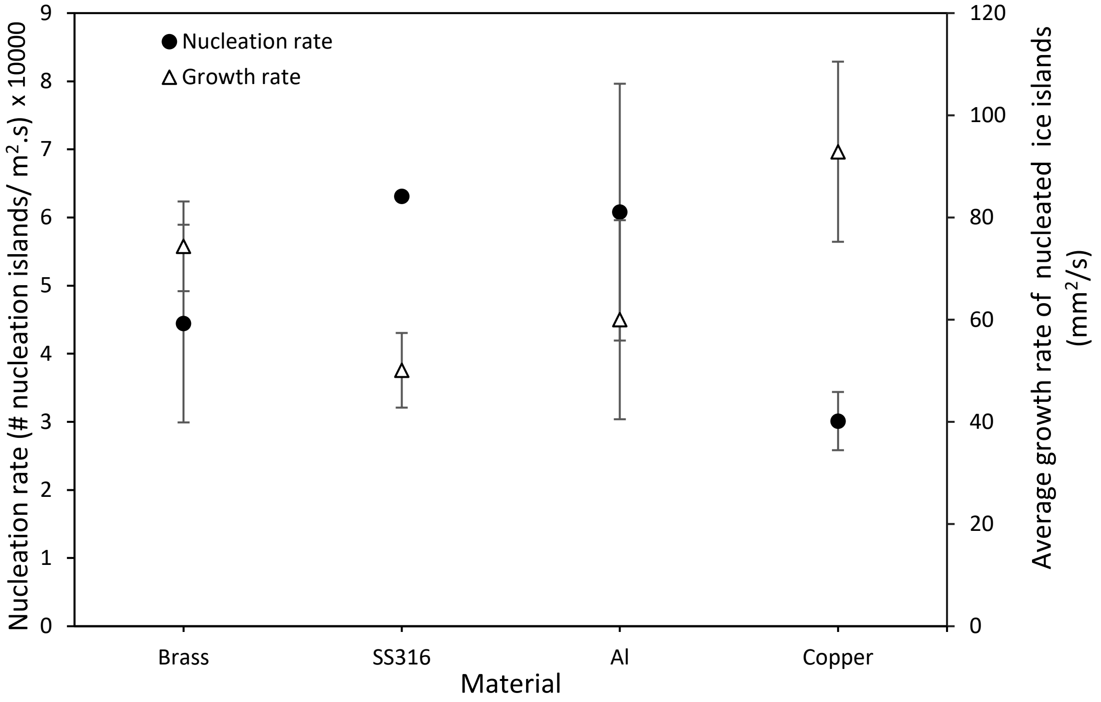

Figure 5.11: *Nucleation and growth rates of ice on the different HX materials at similar heat fluxes.*

However, the nucleation rate occurring on the Brass HX plate did not fit this trend. This unique result can be attributed to the instances of bulk ice nucleation, which resulted from the low surface free energy of the Brass plate. In addition, when heterogeneous nucleation occurred on the Brass plate, it started in the quiescent regions between the Perspex and HX surface of the test cell. This was because, at times, the solution seeped into this area, and a stagnant region was created. According to Fitzner et al. (2015), nucleation started in low mobility regions. In this study, the low mobility regions were created due to the limitation in the design of the test cell. These low mobility regions increased the local supersaturation, resulting in a reduced nucleation rate and higher growth rate (*Figure 5.9* (*d, e*)). The combination of bulk nucleation, and nucleation in the quiescent regions, indicated that a higher ΔG_{crit} was required to be overcome when using the Brass HX plate.

Overall, the nucleation and growth of the ice scale layer were affected by numerous convoluted variables which are difficult to isolate. It is clear, though, from the scaling data with the support of the scaling modes *Figure 5.18*, that the combination of a higher surface free energy material and rough topography resulted in scaling predominantly through nucleation (SS316). When an HX material was smooth but had slightly higher surface free energy, the nucleation rate decreased slightly, and the growth rate increased (Aluminium). When comparing two materials of similar topography, the material of high surface free energy had lower nucleation rates and higher growth rate (Copper). In contrast, the material of lower surface free energy, Brass, had higher nucleation and lower growth rates than the Copper. The overall scaling rates were affected by both nucleation and growth rates.

5.2.3.2. Overall scaling rates on different metals at similar heat fluxes

The combination of both the nucleation and growth rates resulted in the overall scaling rate shown by the initial ice layer forming on the different materials. The scale coverage vs time is depicted in *Figure 5.12:*

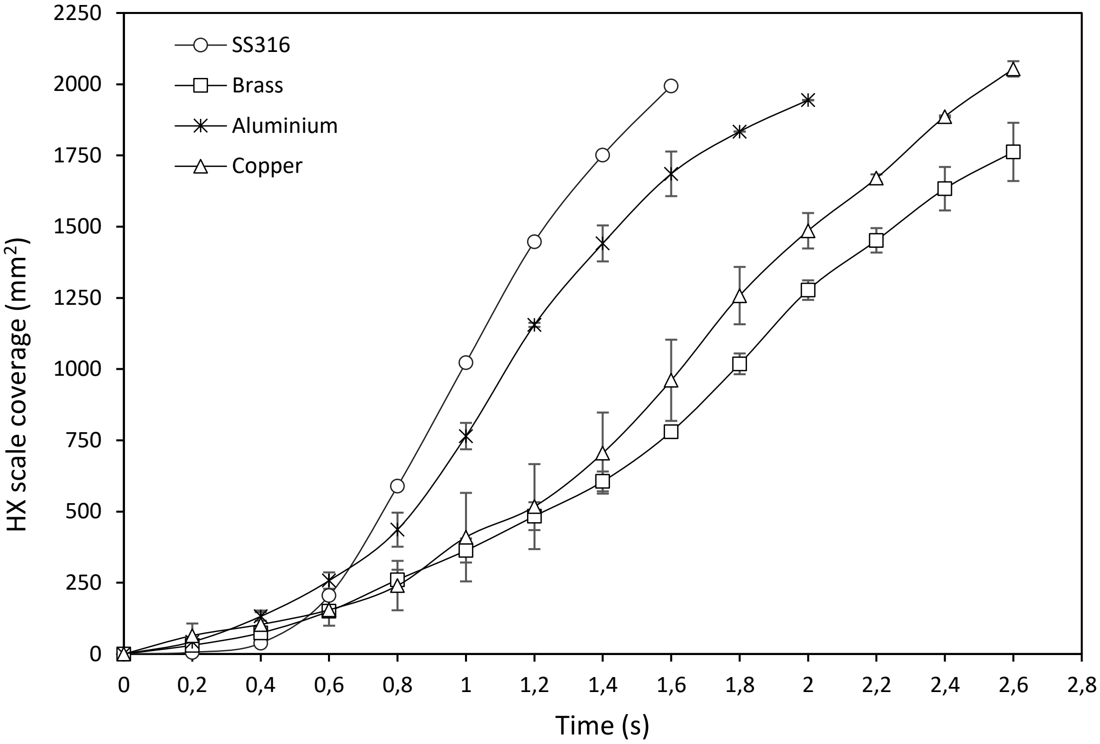

Figure 5.12*: The cumulative ice scale layer coverage on different HX plates, at similar heat fluxes.*

Figure 5.12 shows the rate of coverage of the HX surfaces by the ice scale layer as a result of the combination of nucleation and growth. Although the heterogeneous nucleation of ice occurred randomly on the HX plate, the overall scaling rates did not vary significantly with each experiment for the different materials. However, extreme caution was exercised in keeping all elements of the system constant, as slight changes significantly altered the results, because of the high sensitivity of the system.

When the systems were operated at similar heat fluxes, the scaling mode that resulted in the quickest HX coverage was the nucleation dominated scaling mode. This scaling pattern was emphasised when using the SS316 HX plate. From 0s to 0.4s, the initial heterogeneous nucleation occurred with minimal growth. After 0.4s, the nucleation rate increased, resulting in a steep increase in the scaling rate, peaking between 0.6s and 0.8s at 1086.13 $mm^2.s^{-1}$.

With the Aluminium plate, the initially formed ice nuclei grew to cover a large surface area of the HX plate. After that, more ice crystals nucleated in between the larger ice islands which had nucleated earlier. This development indicated a possibility of scaling that was initiated through secondary contact nucleation, the result of sheared ice crystals from the growing ice layer. This phenomenon was confirmed by the sharp rise in the scaling rate after 0.8s, due to secondary contact nucleation, which resulted in the fastest scaling rate between 0.8s and 1s at 750.37 $mm^2.s^{-1}$.

Growth dominated scaling mode was observed with the Brass and Copper plates at similar heat fluxes. In the case of Brass, the growth domination was because of the growth of the initial ice layer, which originated from the stagnant region of the test cell. The scaling rate of this initially formed ice layer peaked at 153.70 $mm^2.s^{-1}$ and decreased to 63.34 $mm^2.s^{-1}$. The overall scaling rate peaked at 170.23 $mm^2.s^{-1}$ as heterogeneous nucleation initiated in the cooled region of the plate. The increase in scaling rate further affirmed that the scaling mode by heterogeneous nucleation resulted in an accelerated scaling rate than with the growth dominated scaling mode. In the case where Copper was used, the scaling mode was predominantly attributed to growth, as the heterogeneous nucleation rate was the lowest. The scaling rate on the Copper HX plate was highest between 0.8s to 1s, which peaked at 423 $mm^2.s^{-1}$, because of a higher nucleation rate during this period.

Overall, it was seen that materials with a lower surface free energy scaled at a slower rate than materials of higher surface energy. Moreover, what was highlighted was that materials which enhanced heterogeneous nucleation, i.e., those with rough topographies, resulted in the quickest scale coverage. Therefore, to remove the influence of surface roughness on the scaling process, primary-SS316 was compared to a PTFE coated-SS316 plate, to observe the differences in the scaling phenomenon caused solely by the difference in surface free energy.

5.2.3.3. Effect of surface free energy on the nucleation and growth rates

The previous results indicated that scaling through nucleation and growth were affected by numerous variables that are inherent material properties. In this section, the surface free energy of the SS316 material was reduced by coating the surface with *polytetrafluoroethylene* (PTFE), and it was then subjected to different coolant temperatures. It is important to note that the primary-SS316 and the PTFE coated-SS316 had comparable surface roughness rates (R_q) of 120.50 nm and 87.45 nm, respectively. The resulting nucleation and growth rates are shown in *Figure 5.13*, and the overall scaling rates as a result of nucleation and growth are indicated in *Figure 5.14*.

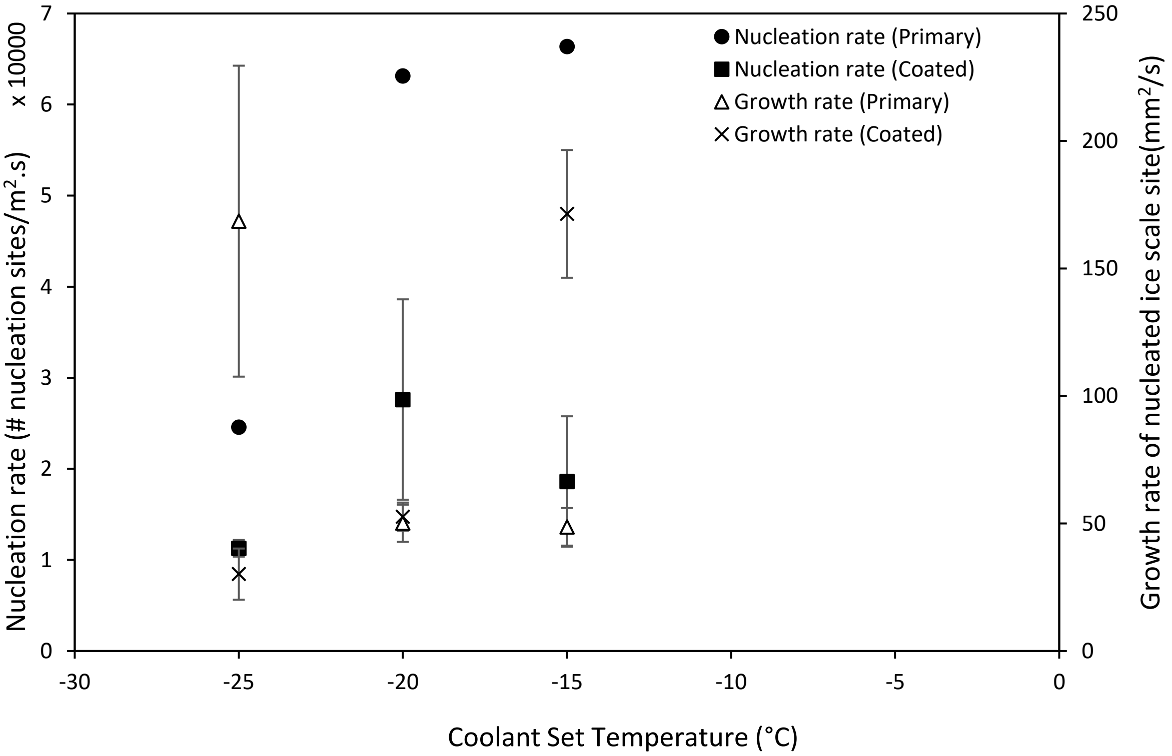

Figure 5.13: *Nucleation (solid markers) and growth (open markers) rates of the ice on the primary and coated-SS316, at different coolant set temperatures.*

The primary and PTFE coated-SS316 were subjected to coolant temperatures of -15 °C, -20 °C, and -25 °C. Each material showed different responses at similar coolant temperatures. The nucleation rates on the primary-SS316 surface increased, with the coolant set temperature. The nucleation rate seemed to plateau with an increase in coolant temperature, which may suggest that the nucleation rate became independent of the cooling rate as it decreased. In contrast, the nucleation rates on the PTFE coated-SS316 HX plate were found to be highest at -20 °C and lowest at -25 °C. The nucleation rate at -15 °C was slightly below the rate at -20 °C. The salt that adhered on to the HX plate reduced the number of ice islands that formed on the HX plate, resulting in the lower nucleation rate.

However, the nucleation rate trends both confirmed that the number of nucleation islands that formed on a surface was higher at a slower cooling rate, independent of the low or high surface free energies. As established by Lewis et al. (2010), faster cooling rates decreased the MSZW of the sodium sulphate system, even though it reached high supersaturations. In turn, this may have resulted in fewer stable nuclei upon nucleation, leading to low heterogeneous nucleation rates at the onset of scaling at higher cooling rates.

The nucleation rates were higher on the primary-SS316 than on the PTFE coated-SS316, at all the coolant operating temperatures. The nucleation rates on the primary-SS316 were 2.18, 2.29 and 3.56 times higher than the nucleation rates on the coated-SS316, at-15 °C, -20 °C, and -25° C respectively, which indicated the anti-wetting property of the low surface free energy material. The findings by Yin et al. (2010) asserted that hydrophobic surfaces did not entirely prevent ice scaling, but had an icephobic potential in the initial stages of ice scaling. The results in *Figure 5.13* agree with that study, as the nucleation rates, which represent the initial stages of scaling, were approximately 2 times higher on the primary-SS316 surface than on the PTFE coated-SS316.

As previous scale coverage data showed, nucleation, not growth, accounted for high scaling rates. The surface of low surface free energy (coated-SS316) reduced the nucleation rate approximately twice as much as the surface of higher surface free energy (primary-SS316). Thus, the coated-SS316 reduce the scaling rate, by reducing the liquid-solid contact time by and by increasing the energy barrier for nucleation (Moaven et al., 2013). Therefore, this result supported the hypothesis that lower surface energy reduced the scaling rate on the HX surface.

It is equally important to consider the growth rates, as they contribute to the overall scaling rates. The general trend observed was that with a rise in nucleation rates, there was a subsequent slowing in the growth rate. This trend was observed on the primary-SS316, but not on the PTFE coated-surface. The changes in the growth rates with the different coolant temperatures were not as significant as those observed on the primary-SS316. This difference indicated that growth occurring normal to the HX surface was enhanced when using a material of lower surface energy, such as the PTFE coated-SS316, while scaling parallel to the HX surface was faster when using the primary-SS316. Studies by Qin et al. (2003) showed that Teflon-coated Stainless Steel took longer to scale the HX surface completely than the primary Stainless Steel. Rahimi et al. (2015) demonstrated that flat hydrophobic surfaces showed slower ice growth and denser ice layers. Therefore, growth parallel to the HX surface seemed to be delayed on the PTFE coated-SS316, increasing the time required to scale the HX surface completely.

5.2.3.4. Overall scaling rates for surfaces of different surface free energies

Overall, the heterogeneous nucleation and growth rates were both reduced by using a material of lower surface energy, and this finding agreed with the work conducted by Alizadeh et al. (2012). Both the nucleation and growth rates contributed to the overall scaling rates, as indicated in *Figure 5.14*. It is therefore important to analyse the combined contributions to the overall scaling rates.

Figure 5.14 shows the coverage of the HX surface with ice scale over time. The area covered by ice scale was analysed until the point where the image became blurred due to bulk crystallization, which occurred three minutes after heterogeneous nucleation. Overall, there was an increase in the scaled surface area with time, although the rate of scaling differed for the two materials. The scaled HX surface area, before bulk ice nucleation, was larger when the primary-SS316 was used than with the PTFE coated-SS316. The time elapsed to scale the HX surface was reduced as the coolant set temperatures were lowered.

The scaling rate on the primary-SS316 increased by 73.7 % and 99.33 % when the coolant temperature was reduced from -15 °C to -20 °C and -25 °C, respectively. In comparison, the scaling rate on the PTFE coated-SS316 only increased by 54.6 % and 47.86 % when the coolant temperature was lowered from -15 °C to -20 °C and -25 °C, respectively. It is therefore evident that the scaling rate was higher when using the primary-SS316 than on the PTFE coated-SS316.

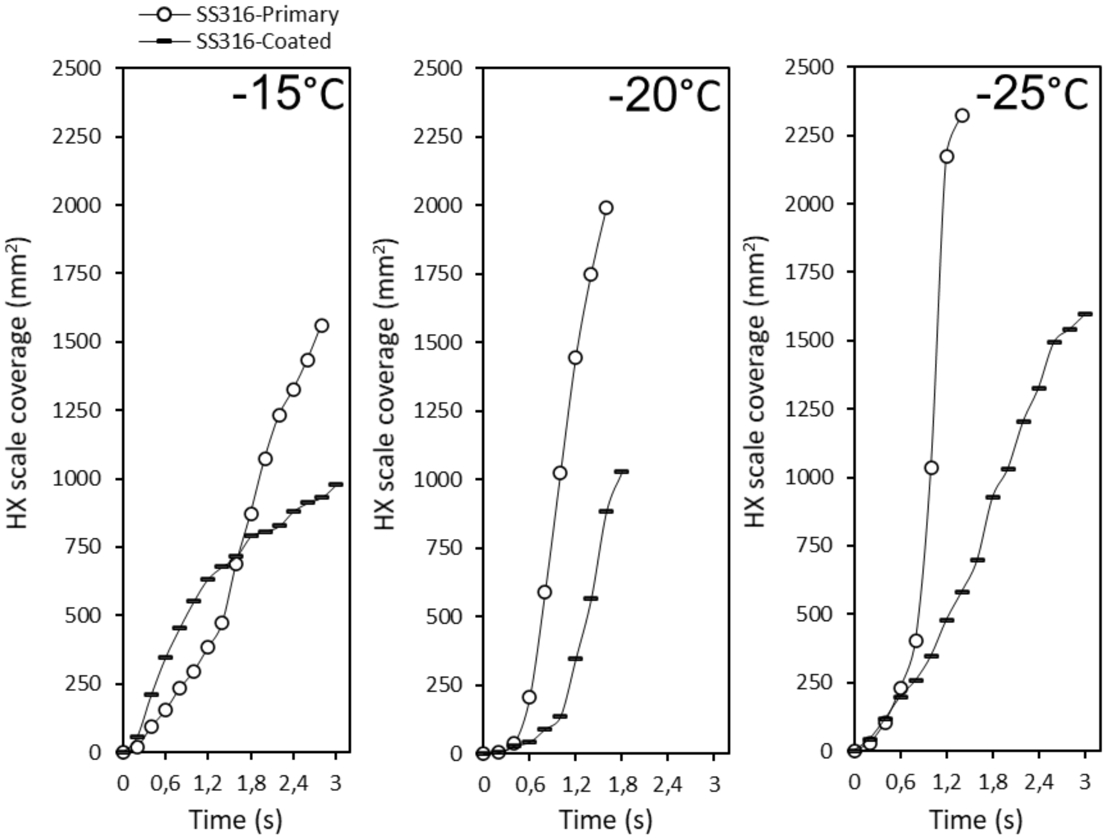

***Figure 5.14**: The cumulative ice scale coverage with time on Primary and PTFE Coated-SS316 at coolant temperatures of -15°C, -20°C, and -25°C.*

When the system was operated at -15 °C, the scaling rate on the PTFE coated-SS316 surface was high in the initial 0.4s, peaking at 492.45 mm^{2}s^{-1}. This initial peak was because of the extremely high growth rate of the ice scale in the vicinity of the scaled salt. This fast growth ceased once the growing ice layer reached the perimeter of the salt scale. Ice scaling occurred by crystallization in the vicinity of the salt scale layer, which was indicated by the spread of bright white colour originating from the centre of the salt scale. Therefore, the nucleation sites that may have occurred in these experiments were not visible. From 0 to 1.4s, the nucleation and growth of ice islands occurred, with a scaling rate of 336.47

mm^2s^{-1}. After 1.4s, nucleation proliferated and resulted in a sharp increase in the scaling rate, which peaked at 551.98 mm^2s^{-1} at 2.2s.

The scaling rates observed at -20 °C started slowly for both HX surfaces. The coated-SS316 had the slowest scaling rate of 168.40 mm^2s^{-1} between 0s and 1s. Similarly, the primary-SS316 surface had an initial slow scaling rate of 95.27 mm^2s^{-1}. Although the scaling exhibited a slow start, a steep rise in heterogenous nucleation was observed both materials. The peak scaling rates for both materials were 1629.55 mm^2s^{-1} for the primary-SS316 and 1117.61 mm^2s^{-1} and coated-SS316 HX plates.

At -25 °C, the scaling rate on the coated-SS316 indicated a constant scaling rate. The growth on this surface occurred mainly on the formed ice scaled sites, and horizontal growth was less than that observed on the primary-SS316 plate, resulting in a peak in the scaling rate of 574.68 mm^2s^{-1} between 1.6s and 1.8s. The scaling rate on the primary-SS316 HX plate was initially 502.86 mm^2s^{-1} between 0 and 0.8s and peaked at 3195.58 mm^2s^{-1} between 0.8s and 1.4s. The scaling rate was 5.5 times faster when using the material of higher surface energy, which corroborated work done by Rahimi et al. (2015), who observed that hydrophobic surfaces exhibited slower ice scaling rate.

5.3. Effect of surface topography on scaling

This section discusses the effects of topography on the scaling process through heterogeneous nucleation and growth. SS316 was selected for this investigation as it is widely used in the industry. The SS316 surface roughness was measured using atomic force microscopy (AFM). The following roughness values were assessed from three randomly selected areas on the HX surfaces. Surface roughness has mainly been studied in the context of its influence on ice scaling by adhesion (Zou et al., 2011; Matsumoto et al., 2012). In this study, the influence of roughness on the heterogeneous nucleation of ice was investigated

5.3.1. Surface topography of Primary-SS316 and Rough-SS316

Surface topography encompasses the contour shape, roughness, waviness and finish of a solid surface. Surface topography can be a result of the manufacturing process and surface modification. In this section, the effect of surface topography on the scaling induction time and the scaling rate is discussed. Therefore, the surfaces of the primary-SS316 (*Figure 5.15*) and roughened-SS316 (*Figure 5.16*) were analysed by using atomic force microscopy (AFM).

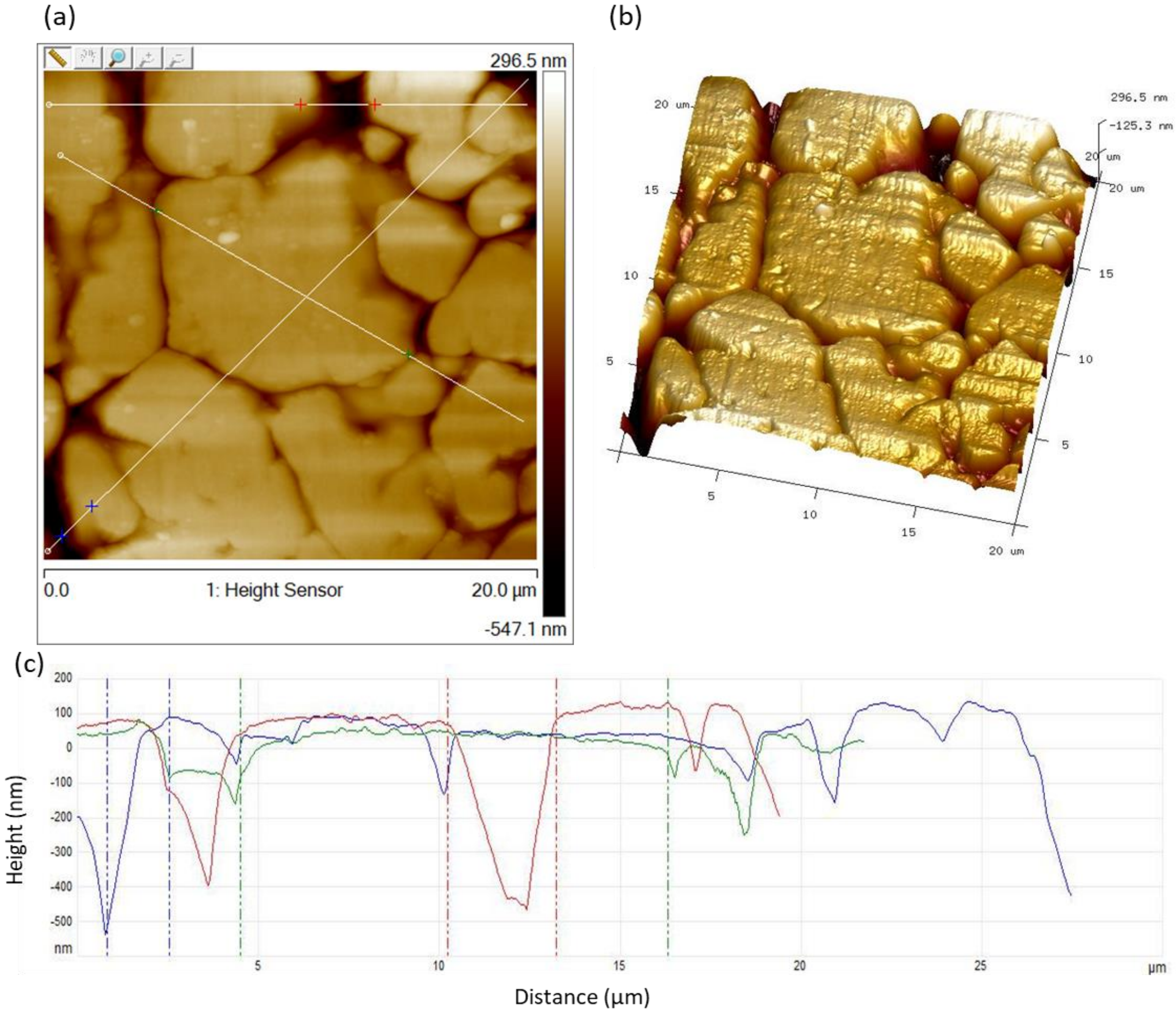

Figure 5.15: *Atomic Force Microscopy topography images of the Primary-SS316 surface, from the manufacturer, on a 400µm^2 area. Image (a) shows the top view and (b) is the three-dimensional (3D) view, and (c) is the height variations along with the white line segments indicated in(a).*

A sample of the SS316 plate was analysed on three randomly selected 400 µm^2 areas, indicated in *Figure 5.15* (*a*) and (*b*). The average root-mean-square roughness (Rq) of the area above, was found to be, on average 108.5 nm. The primary-SS316 (as received from the manufacturer) consisted of peaks of small to large surface areas which appeared like ordered boulders packed tightly together. The spaces between these peaks are crevices that occur across the entire plate. The amplitude of the highest peak in this area was 296.5 nm while the deepest crevice was 547.1 nm. The crevice was 84.5% deeper in the vertical distance to the highest peak measured, and the roughness width ranged from approximately 0.71 nm to 2.86 nm. These measurements indicated that these crevices were also very narrow relative to the broad flat peaks. The approximate surface area of the broader peaks ranged from 19.2 µm^2 to 0.64 µm^2. These values showed the general non-uniformity of the SS316 surface topography post-manufacturing. *Figure 5.15*(*c*) graphically presents the topography of the surface, indicating the roughness and waviness the material. The micro-blasted-SS316 was analysed using AFM, and *Figure 5.16* (*a* to *c*) indicates its change in topography.

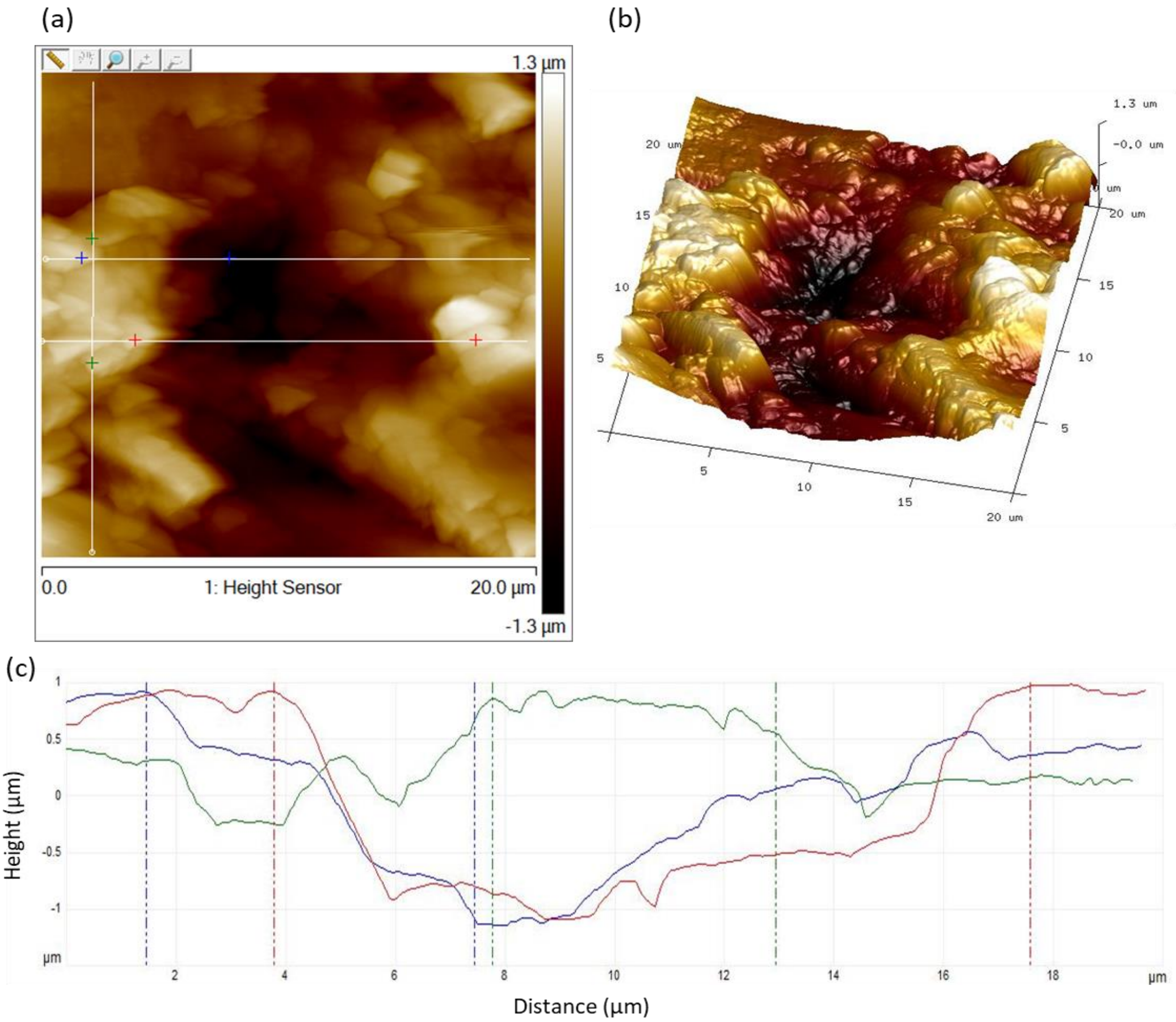

Figure 5.16: *Atomic Force Microscopy topography images of micro-blasted-SS316 on a 400μm^2 area. Image (a) is the top view, (b) is the 3D view, and (c) is the height variations along with the line segments in the image (a).*

The micro-blasted-SS316 surface was analysed on three randomly selected, 400 µm^2 areas, as indicated in *Figure 5.16* (*a*) and (*b*). The average root-mean-square roughness (Rq) of the analysed areas was 446.5 nm, which is a 311.5 % increase in average roughness over the primary-SS316 surface. The surface was characterised by continuous peaks and valleys and had no narrow crevices. The two-dimensional 2D height image shows the highest peak and deepest valley in the analysed area both had a roughness height of 1.3 µm. Therefore, micro-blasting equalised the amplitude of the peaks and the valleys from the reference plane.

Figure 5.16 (*c*) indicates the increase in the roughness width (peak to peak distance) as compared to *Figure 5.15* (*c*). This change is significant as it eliminated the narrow crevices and created broader valleys. These broad valleys may minimise the presence of quiescent regions on the HX surface and increase the flow of the solution over the surface through turbulence, thereby affecting the heat flux of the system. The surface roughness affects the scaling probability on the surface since it increases the density of nucleation sites and promotes adhesion of crystalline particles. Therefore, it is essential to assess the effect of the different topographies on the scaling induction time, in order to compare the influence of surface topography on the overall scaling process.

5.3.2. Scaling induction times for ice scale formation on Primary and Rough-SS316

Surface roughness has been studied to understand its effect on adhesion strength of scalants. It is, however, equally important to understand the effect of surface roughness on the inception of the scaling process. Therefore, in this section, two SS316 surfaces of different degrees of roughness's were used to study the effect of surface roughness on the scaling induction times.

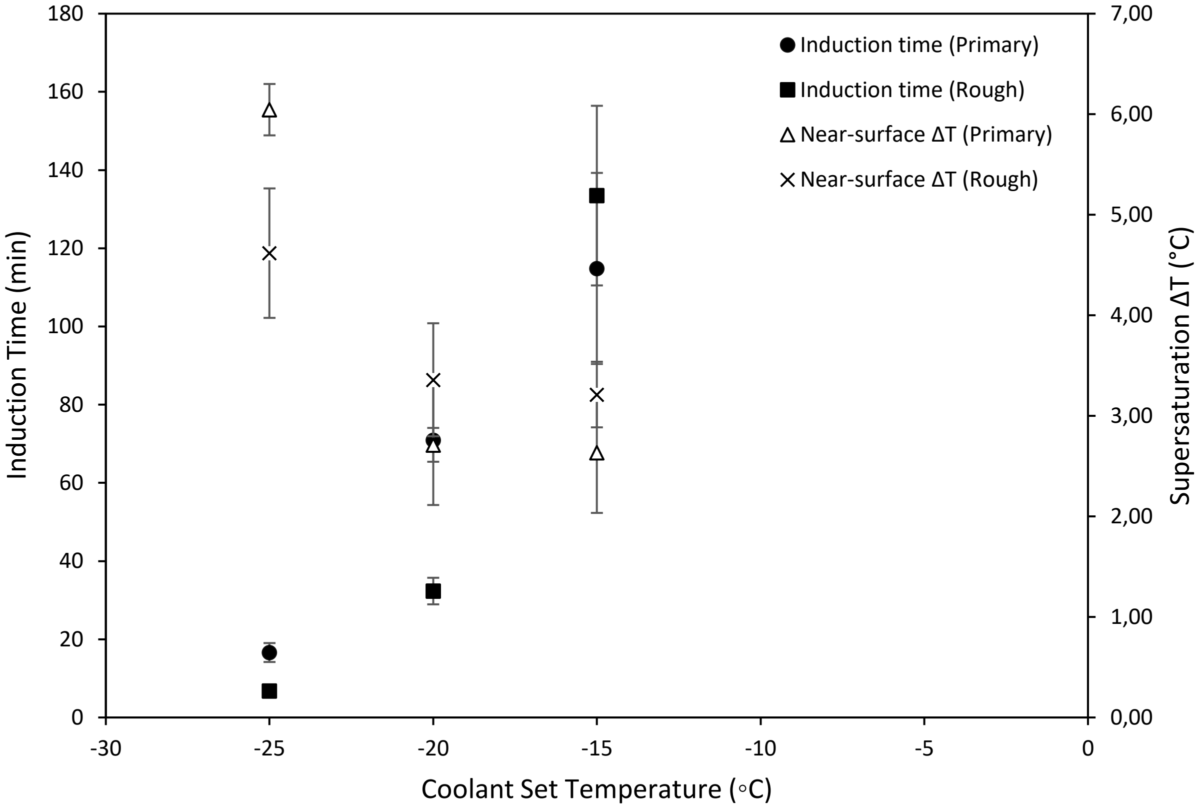

***Figure 5.17**: Effect of surface roughness on the scaling induction times (open markers) and the near-surface supersaturation (solid markers) for primary and micro-blasted-SS316, at different coolant temperatures.*

Figure 5.17 shows the differences in the scaling induction time and supersaturations for the primary and roughened-SS316 plates, at different coolant temperatures. There was an overall increase in the scaling induction times with the coolant temperature for both types of HX materials. At the same time, the level of supersaturation was reduced for both when operating at higher coolant temperatures. Therefore, the effect of the coolant temperature was similar for both HX plates.

Although the general trends of the two topographies were similar, there were differences between the recorded scaling induction times at each coolant temperature. These differences were an indicator of the influence of the surface roughness on the probability of scaling. At the coolant temperature of -15 °C, the rough-SS316 surface was more effective in lengthening the induction time than the primary-SS316 surface. The scaling induction time for the rough-SS316 surface was 1.16 times longer than that of the primary-SS316 surface. This result contradicts the findings by Budair et al. (1998), who indicated that smoother surfaces resulted in longer induction times. However, when the coolant temperatures were decreased to -20 °C and -25 °C, the scaling induction times for the primary-SS316 surface became 2.19 and 2.43 times longer than those recorded for the rough-SS316 surface at the respective coolant temperatures. Consequently, the rough-SS316 surface lengthened scaling induction times up to some point higher than -20 °C, beyond which they start to decline. This observation was attributed to the waviness of the roughened surface, which increased the turbulence at the surface. The increased turbulence, at lower supersaturations, allowed uniform distribution of the supersaturation across the HX plate, hence extending the scaling induction time.

These scaling induction time results indicated that the extent of roughness alone is not a determining factor in the scaling induction time. The type of surface topography that results in roughness plays a vital role. The longer scaling induction time, at -15 °C, was be attributed to the increase in the degree of turbulence near the surface. This agrees with, Albert et al. (2011), who reported that the enhancement of turbulent convective heat transfer caused by roughening increased the overall heat transfer, thereby lengthening the induction time. The supersaturation attained when using the rough-SS316 surface was 1.22-fold and 1.24-fold greater than that on the primary-SS316 surface, when operating at -15 °C and -20 °C respectively. However, at -25 °C, the primary-SS316 reached a supersaturation level that was 1.3-fold higher than that of the rough-SS316. These results indicated that deep crevices on the HX surface results in quicker scaling when operating at lower coolant temperatures.

Therefore topography, not just roughness, is important to consider. A surface had smoother, large area peaks, with deep sharp crevices, as observed for the primary-SS316 surface. These crevices result in the faster development of quiescent zones of high local supersaturation, resulting in the shorter scaling induction times for the primary-SS316, at a coolant temperature of -15 °C (Bi et al., 2017). Although the primary-SS316 was smoother than the rough (micro-blasted) SS316, these crevices made it more prone to scaling at a higher coolant temperature.

When the coolant temperatures were decreased to -20 °C and -25 °C, the benefits of using a rougher surface were no longer observed. The roughness height of the roughed surface was approximately 13 µm, whereas the primary surface measured about 0.55 µm. The roughness height on the rough-SS316 surface, coupled with the faster cooling rates, may have accelerated the crystallization of ice near the HX surface. Overall, these results indicate that the effect of the surface topography changed with the cooling rates of the system.

5.3.3. Ice scaling modes on the primary and rough-SS316 HX surfaces

Surface topography plays an important role in ice scaling through heterogeneous nucleation and adhesion. The main scaling mode on the rough HX material was first through adhesion of salt crystals, followed by heterogeneous nucleation of ice. *Figure 5.18* compared the images of ice scaling modes on the primary (a, c and e) and rough (b, d and f), two seconds after heterogeneous ice nucleation. *Appendix A.5* shows the sequence of the scaling phenomenon from the onset of ice scaling until bulk crystallization occurred, while *Figure 5.18* shows the heterogeneous nucleation of ice, two seconds after it had initiated.

(a- Primary SS316 at -15°)

(b- Rough-SS316 at -15°)

(c Primary SS316 at -20°)

(d- Rough-SS316 at -20°)

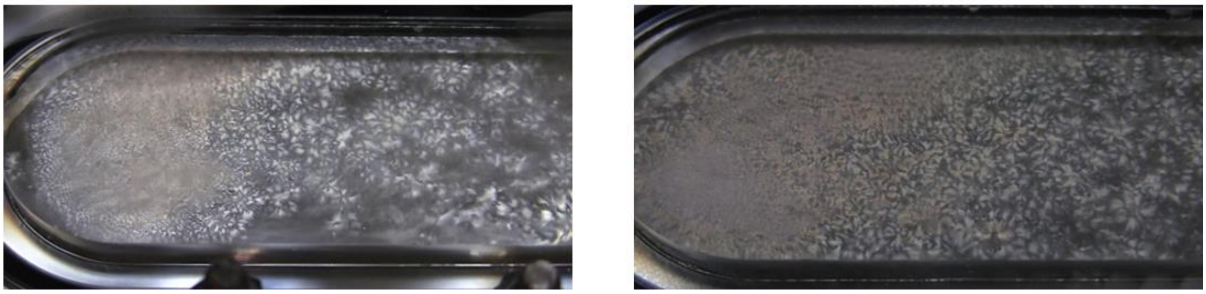

(e- Primary-SS316 at -25°)

(f- Rough-SS316 at -25°)

Figure 5.18: *Comparison between the scaling modes on the Primary (a, c and e) and Rough-SS316 (b, d and f) two seconds after the start of heterogeneous nucleation. Frames a and b represent scaling mode at -15°C, frames (c) and (d) are at -25°C and frames (e) and (f) at -25°C.*

The ice scaling modes on the primary-SS316 and micro-blasted-SS316 HX plates, at -15 °C, at -20 °C and -25 °C, to investigate the effect of different cooling rates on the scaling phenomena on both surfaces. Cuboidal salt crystals that crystallized in the bulk solution adhered on to the rough HX surface at coolant temperatures of -15 °C and -20 °C. Cuboidal salt crystals were not observed in the bulk solution at -25 °C. However, salt crystals seem to have nucleated on the HX surface and continued to grow into needles. It was unclear if heterogeneous nucleation of the salt occurred at -25 °C, or if the growth observed resulted from adhered salt crystals of undetectable size.

There was an evident enhancement of bulk salt crystallization when cooling at -15 °C, but the salt crystals did not adhere to the surface of the primary-SS316 HX plate (*Figure 5.18 (a)*). Crystals that nucleated in the bulk solution flowed at higher velocities; therefore, it was impossible to observe their morphologies with the equipment used in these experiments. However, the salt crystals forming near the HX surface could be observed as they moved in a slower Brownian motion. The salt crystals near the primary-HX plate grew into large cuboidal platelet morphologies. Once these crystals became large enough, they were sheared from the HX surface by the bulk flowing solution. In addition, these salt crystals near the HX surface did not adhere to the primary-SS316 surface, nor did they initiate ice scaling. Ice scaling initiated through heterogeneous nucleation. At a coolant temperature of -15 °C, growth was pronounced whereas operating at lower coolant temperatures resulted in enhanced nucleation. Therefore, smaller roughness width of the crevices, on the primary-SS316, are less likely to induce scale formation by adhesion of bulk crystals.

However, the larger roughness width of the rough-SS316 promoted the adhesion of the bulk salt crystals onto its surface. In *Figure 5.18* (*b*), fewer bulk salt crystals were observed compared to the primary surface *Figure 5.18* (*a*). The reduction of the bulk crystals was due to the deposition of bulk salt crystals on to the rough HX surface. The scaling phenomenon observed in these experiments substantiates the work by Förster and Bohnet (1999), where broad valleys enhanced crystal adhesion. The deposit concentrated in one region as the salt scale layer continued to grow. The growth of this layer occurred through adhesion of individual and agglomerated salt crystals. In this region of salt scale, a bright white colour appeared and spread from the centre of the salt scale, indicating ice scaling. This phenomenon can be induced by the scaled salt, which created regions of water stagnation among the salt crystals. These quiescent regions may have resulted in high local supersaturation with respect to water, which induced heterogeneous ice nucleation. In addition to the quiescent regions, the lower salt ion concentration of the solution in this region might have also contributed to the increased supersaturation for ice crystallization.

The appearance of more ice nucleation occurred only once the ice scale layer had spread across the entire area that was covered by salt scale mass. The reason for this is unclear, although it occurred consistently in all experiments where the salt had scaled prior to ice scaling. This observation further supports the possibility of a higher supersaturation for ice in the region where salt crystals had scaled. Therefore, surface roughness, defined by peaks and broader valleys both enhanced the adhesion of bulk salt crystals, as seen in *Figure 5.18* (*b*), and influenced the mode of ice scaling.

At a coolant temperature of -20 °C, the bulk salt crystals were minimal or not observable on the primary surface, and the crystal mass deposited was less than at -15 °C on the rough surface. The salt crystals adhered to the surface at the coldest region of the rough HX surface, with more bulk salt crystals present than at -15 °C. This change indicated that the shorter scaling induction times recorded for this experiment reduced the time for salt adhesion. It also confirmed that salt scaling occurred through adhesion of bulk crystals and not heterogeneous nucleation on the HX surface.

An intriguing change in salt crystal morphology was observed for the first time when cooling at -25 °C. The crystal morphology was no longer the cuboidal plates seen at coolant temperatures of -15 °C and -20 °C but changed to needle-type morphology at -25 °C. The change in morphology occurred as a consequence of increased supersaturation and not the difference in surface topography. The needles that crystallized on the primary surface moved freely and slowly near the HX plate, resembling Brownian motion. The needles crystallizing on the rough surface adhered, and continued to grow, following the contours of the valleys of the HX surface until ice heterogeneously nucleated. It was evident, therefore, that the change in crystal morphology might also alter the scaling mode in a system.

For this first time, there were instances where the needle salt crystals adhered to the primary surface. These needle-type crystals may have been able to lodge in the narrow crevices, unlike the cuboidal type morphology. The salt crystals remained in Brownian motion until they ultimately agglomerated and ceased movement as they adhered to the primary surface. Once these agglomerated salt crystals adhered to the HX surfaces, ice scaling started at the centre of the salt scale. The nucleation of ice might have been premature because the salt scale may have created quiescent regions in between the adhered salt crystals, resulting in ice nucleation. In some cases, the adhered $Na_2SO_4 \cdot 10H_2O$ agglomerates were dislodged from the primary surface by the shear force exerted by the flowing bulk solution on to the salt scale mass. The ability of the bulk fluid to dislodge the adhered salt scale was consistent with findings by Förster and Bohnet (1999), who showed that a surface such as that of primary-SS316 provided minimal sites for adhesion compared to the micro-blasted-SS316 with its broader valleys.

Previous studies have shown that salt scaling of $CaSO_4$, $CaCO_3$ and in some cases, co-precipitation of the two salts (Förster and Bohnet, 1999; Helalizadeh et al., 2000; MacAdam and Parsons, 2004; Kazi et al., 2010; Cheong et al., 2013; Pääkkönen et al., 2015). Salt scaling compounds covered in the research literature are known to be mainly of the sparingly soluble. Khan (2005) investigated the deposition of sodium salts on HX surfaces but did not investigate the effect of the surface topography. Heating crystallization was used in the experiments, thus crystallizing Na_2SO_4, which subsequently scaled on the HX surface. Scaling by $Na_2SO_4 \cdot 10H_2O$ has not been reported in literature, which indicates that this salt has not been identified as one prevalent in fouling of HX surfaces. The findings of this investigation indicated that the surface topography could render a non-scaling salt into a scaling salt. This highlights the importance of surface topography on the scaling process during crystallization. This knowledge is important because these experiments showed that $Na_2SO_4 \cdot 10H_2O$ salt scaling, induced ice scaling during EFC.

5.3.4. Effect of surface roughness on crystallization kinetics of the ice scale layer

This section focuses on the effects of material surface topographic roughness on the scaling phenomenon. Heterogeneous nucleation and growth of ice contributed to the overall ice scaling rate on an HX plate. The effects of surface roughness on the heterogeneous nucleation, growth and overall scaling rates of ice were analysed, as indicated in *Figure 5.19* and *Figure 5.20*.

Figure 5.19 shows the nucleation and subsequent growth rates which occurred on the primary-SS316 and the rough-SS316 HX surfaces, at different coolant set temperatures. The nucleation rates increased with the coolant temperature, while the subsequent growth rates decreased. The nucleation rates on the rough HX surface were positively linear with the coolant temperature, while the nucleation rates on the primary HX surface plateaued at higher coolant temperatures. The opposite trends were observed for the growth rates on both surfaces. This result indicated that at lower supersaturations, the nucleation rate barely changed but the induction time was extended.

Although the nucleation rates on both surfaces increased with coolant temperature, the rate at which it occurred was different on the different materials. At a coolant temperature of -15 °C, nucleation rates were 1.14 times higher on the rough-SS316 surface than on the primary-SS316 surface. At coolant temperatures of -20 °C and -25 °C, the nucleation rates were 1.25 and 1.83-fold higher on the primary surface than on the rough surface. The higher nucleation rates on the primary surface were attributed to the surface topography of the primary-SS316 HX surface, which consisted of the narrow crevices that intersected large surface area peaks of the HX surface (*Figure 5.15*). Förster et al. (1999) and Bi et al. (2017) showed that rougher surfaces made for stronger interfacial strength due to increased interfacial contact area. Therefore, the resulting high interfacial bonding area should, therefore, minimise the free energy for nucleation, giving rise to the high nucleation rate.

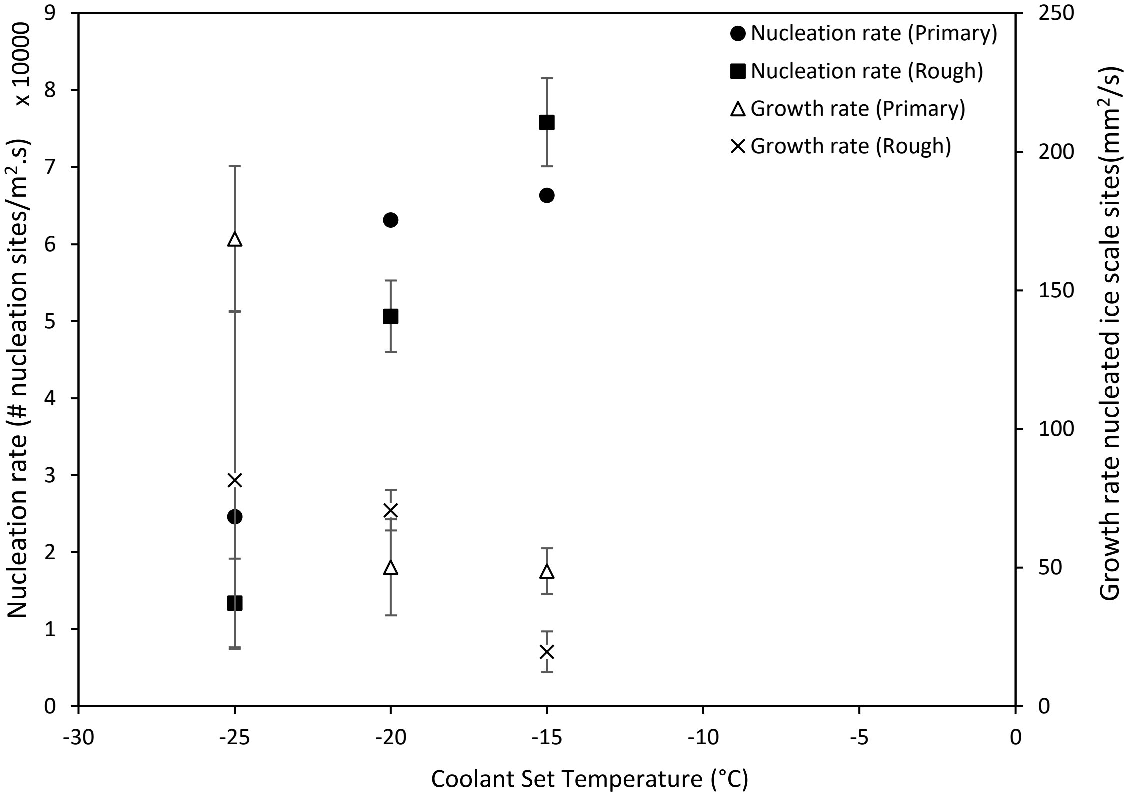

Figure 5.19: *Average nucleation rates of ice on Primary and Rough-SS316 HX plates at different coolant temperatures.*

However, the results presented *in Figure 5.19,* partially contradicted this statement at coolant temperatures -20 °C and -25 °C. The roughed surface had an R_q of 446.5 nm while the primary surface had an R_q of 120.5 nm, but the nucleation rates were higher on the primary HX plate. Therefore, nucleation not only depends on the degree of roughness (R_q) but also on the surface profile, which results in the roughness. As shown in this study, a surface profile that consisted of crevices intensified the scaling through heterogeneous nucleation in a way that a highly rough surface with broader valleys did not. Therefore, it can be deduced that surface roughness enhanced nucleation on the surface, but the roughness profile also influenced the rate of heterogeneous nucleation.

Although it was tempting to expect that the resulting nucleation rates would be inversely proportional to the induction times as per the classical nucleation theory, *Figure 5.11, Figure 5.13* and *Figure 5.19* indicated that there was no such correlation in this investigation. This was unexpected result arose from the continuously changing supersaturation during the cooling process, which resulted in a cumulative effect. Therefore, if it were possible to maintain a constant supersaturation, then the experimental and theoretical induction times would be comparable. In addition to the cumulative supersaturation, there were numerous variables which were affecting the ice scaling induction time. It would not, therefore, be correct to compare the theoretical nucleation rates and the inverse of the scaling induction directly.

Both heterogeneous nucleation and growth rates contributed to the overall rate at which the ice scaled on the HX surface. *Figure 5.20* shows the combined effect of the crystallization processes, resulting in a scaled HX surface.

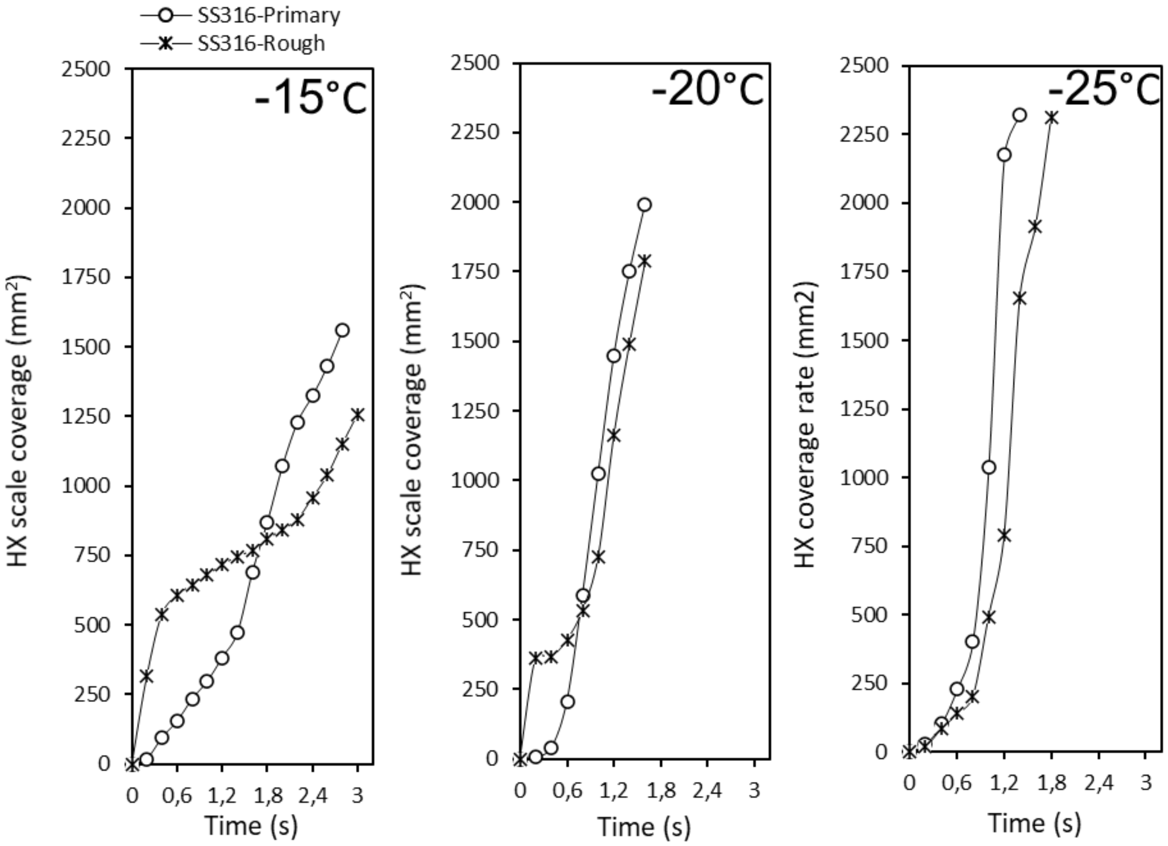

Figure 5.20: *The cumulative horizontal ice layer growth with time, at coolant cooling temperatures of -15°C, -20°C, and -25°C for the Primary and Rough HX surfaces.*

Figure 5.20 shows the effect of surface roughness on the rate of scaling at different coolant temperatures. The scaling rate increased with a decrease in the coolant temperature for both the rough and primary-SS316 HX surfaces. When the coolant temperature was lowered from -15 °C to -20 °C, and -25 °C, the scaling rates on the rough surface escalated by 91.70 % and 101.71 % respectively. The scaling rate on the primary surface showed a similar trend as it increased by 73.7 % and 99.33 % when the coolant temperature was reduced from -15 °C to -20 °C and then to -25 °C, respectively. These observations suggest that the scaling rate is enhanced on a rough HX surface.

When the system operated at -15 °C, the rougher surface exhibited high initial scaling rates which were mainly attributed to the adhered salt scale formation. The combination of rough topography, which created regions of local supersaturations, and the salt scale in those areas resulted in the high initial scaling rates with the roughened surfaces. The roughened surface had an initial scaling rate of 1345.64 mm^{2}s^{-1} in the first 0.4s, the highest recorded for the initial 0.4s. This spike in nucleation plateaued, reaching a scaling rate of 203.52 mm^{2}s^{-1} between 0.4s and 2.2s. During this period, the nucleation site grew within the salt crystals. Therefore, the presence of the salt crystals may have limited the growth rate by impeding the attachment of growth units of water on the growth front. Once the ice scale growth front reached the HX surface that was free from salt scaling, heterogeneous nucleation initiated, which resulted in a spike in the scaling rate. This spike was showed in the faster scaling rate after 1.4s, which peaked at 468.78 mm^{2}s^{-1}.

Scaling on the rough-SS316 surface was initially due to the faster horizontal growth of the ice island from within the salt scaled area. Ice growth within the vicinity of the scaled salt occurred in the initial periods between 0s and 0.4s, 0.2s and 0.8s, when operating at -15 °C, -20 °C and -25 °C respectively. Between these periods, scaling did not occur on the HX surface. It was only once the ice grew to the perimeter of the salt scale, that heterogeneous nucleation started on the regions free of salt scale. The faster the ice scale layer reached the unscaled HX surface, the faster the initiation of nucleation sites on the HX surface, resulting in a faster scaling rate.

It is not clear why the initiation of nucleation sites only appeared once the growing ice scale reached the boundary of the salt scale layer. However, this type of ice scaling mode was consistent on rougher surfaces, including PTFE coated-SS316, which shows that it was a function of the surface topography. As described by Hodgson and Haq (2009), this development could be a result of secondary nucleation, where the formation of a nucleation site may trigger the formation of other nucleation sites where the monolayer had already adsorbed on to the surface.

At -25 °C, the primary and rough HX surface nucleation rates peaked at 2530.56 mm^2s^{-1} (between 1s and 1.2s), and 2834.42 mm^2s^{-1} (between 1.2 and 1.4s), respectively. At all coolant temperatures, the rough-SS316 had the highest scaling rate despite initial delays in ice scaling due to salt scale. Furthermore, the variation in scaling rate depended on the presence of salt scale at the interface, and whether nucleation or growth was the predominant scaling mode within a particular time interval. This result is in line with previous studies which showed that the rougher surface topography led to higher scaling rates (Doyle et al., 2002; Heydari et al., 2016). In those studies, a final mass was measured after a set period, whereas in this study, the technique used allowed for the observation of the initial scale layer formation in real-time. This approach provided a more detailed insight into how an initial ice scale layer formed across the different surface topographies. The practical detail provided by this study is currently unavailable in published literature due to the techniques used, which did not allow real-time analysis of the scaling process.

6. Conclusions

Ice scaling of the HX surface is one of the major challenges faced in the industrial implementation of continuous EFC. Controlling the formation of ice scale has been done with limited success by using mechanical scrapers. Some of these limitations have been associated with the HX surface properties such as the HX surface topography. This observation highlighted the requirement to understand the influence of HX surface properties on ice scaling, to improve the control of ice scaling in EFC.

This research aimed to understand the effect of the HX surface properties on ice scaling. The focus was specifically on the effect of the surface free energy and roughness of the HX material on ice scaling. The use of a uniquely designed crystallizer test cell, which mimicked the region near the HX wall of a crystallizer, made it possible to study the effect of these HX surface properties on ice scaling. Using the DIC method, together with the crystallizer test cell, proved an effective method for achieving the objectives of this study, as for the first time, it was possible to investigate the scaling phenomenon in a continuous crystallizing system, using in situ, real-time observations.

This method allowed the study of the initial ice scale layer as it formed on different HX surfaces, a part of the process which has not previously been observed. Overall, the initial ice scale layer developed through heterogeneous nucleation, followed by horizontal growth. Although the actual nucleation process (which occurs at nanometre scale) was not observable with the equipment used, the distinct ice islands that formed on the HX surface indicated where nucleation started. While horizontal growth occurred, the DIC method also allowed for the approximation of the thickness of the ice layer, by the observed retardations, which indicated that growth proceeded both parallel and normal to the HX surface.

Scaling predominating through nucleation, horizontal growth, or a balance of both defined the scaling mode. The scaling modes differed on the different HX surfaces. The Aluminium HX plate scaled through a balance of nucleation and growth, but growth dominated at the initial stages of scaling, followed by an increase in nucleation later in the scaling process. The Brass HX plate also exhibited a balance of both nucleation and growth throughout the scaling process, showing the most balanced scaling mode. The Copper HX plate was dominated by growth with the fewest nucleation island of all the HX surfaces used. The scaling mode for both the primary-SS316 and roughened-SS316 was predominantly nucleation. In contrast, nucleation was reduced, and growth increased on the PTFE coated-SS316 as the scaling modes observed were a function of the surface topography and surface free energy.

The predominance of either nucleation or growth ultimately affected the overall scaling rate on the different HX surfaces. The scaling rates were highest with the SS316 HX plate followed by Aluminium, then Copper, and lastly the Brass HX plate. The observation indicated that materials with nucleation-dominated scaling mode resulted in higher scaling rates than those with the growth dominated scaling mode. Coating the SS316 decreased the overall scaling rate while roughening the SS316 increased the scaling rate. These results have considerable practical implications, as they provide an understanding that the HX surface topography contributes to the difficulty faced by the industry to keep the SS316 free from ice, even when scraping. Therefore, using materials with surface properties that lower the probability for nucleation can assist in reducing the scaling rate. These findings suggested that a smooth surface of low surface free energy would be most efficient in reducing the rate of ice scaling.

Temperature measurements were used to determine the times at which nucleation occurred. The period between the attainment of the eutectic temperature and nucleation temperature was referred to as the scaling induction time. Quantitative analysis of the scaling phenomenon showed that ice scaling induction times were longer when using a material of low surface free energy. Therefore, materials of lower surface energy delayed the onset of heterogeneous nucleation, due to the higher energy barrier for nucleation on the surface, meaning a higher driving force was required for ice scaling on the HX surface. This is vital in the implementation of EFC as it can reduce the frequency of downtime due to ice scaling on the HX surface. In addition to increasing the scaling induction times, the material of lower surface free energy increased the level of supersaturation within the bulk solution, resulting in instances of bulk nucleation. The increase of supersaturation in the bulk solution is beneficial to the EFC process because continuous bulk crystallization is required for an efficient EFC process.

At faster cooling rates, however, the low surface free energy material ceased to be efficient in increasing the induction time. At rapid cooling rates, the PTFE coated-SS316 and primary-SS316 showed no difference in the scaling induction times. Therefore, the ability of the low surface free energy material to increase the scaling induction time was limited by the cooling rate imposed on the system. At lower cooling rates, the PTFE coated-SS316 was able to increase the scaling induction time 2.79-fold. Therefore, the results suggest that lowering the surface free energy of an HX material is dependent on the system parameters. It is therefore important to establish the best cooling rate to realise the benefits of using a material of low surface free energy for a particular system.

The scaling induction time was also found to be strongly affected by the HX surface topography. A rough surface reduced the scaling induction times at higher cooling rates and increased the scaling induction time at lower cooling rates. Although fluid dynamics were not covered in this study, rough surfaces are known to increase turbulence at the interface. The results obtained indicate that this phenomenon might be effective at lower cooling rates. At faster cooling rates, however, the rough surface resulted in short scaling induction times, possibly indicating that the faster cooling rates increased the rate ordering of water molecules within the valleys, resulting in shorter scaling induction times. Therefore, the faster cooling rates may have reduced the turbulence created by the rough surface, due to rapid ordering of water molecules at the solution-liquid interface.

The length of the scaling induction times was found to influence the number of nuclei observed on the Aluminium, Brass, Copper and SS316 metal plates. Shorter induction times resulted in the formation of fewer nucleation islands on all the HX surfaces, while longer induction times resulted in more nucleation islands seen on all the metals used. This observation indicated that longer induction times might have increased in the number of stable nuclei at the point of nucleation, hence increasing the nucleation rate. However, the PTFE coated-SS316 had minimal nucleation sites compared the primary-SS316, irrespective of the length of the scaling induction time. The material of low surface free energy could, therefore, reduce the nucleation rate, and thus, the overall scaling rate.

Overall, scaling is a complex phenomenon which is governed simultaneously by multiple variables and understanding the effect of some of the primary variables, such as surface free energy and topography could assist in reducing and efficiently controlling scale formation in EFC. The current study has, therefore, demonstrated that the selection of smooth HX materials of low surface free energy would be most beneficial in increasing the process scaling induction time, increasing solution supersaturation and reducing the scaling rate on the HX surface.

7. Recommendations

This study demonstrated how the ice scale layer started on different HX surfaces in ways which revealed that different materials scale differently in similar operating conditions. Therefore, a careful selection of an appropriate HX construction material is crucial for effective control of the scaling problem. However, it is recommended that more experiments should be conducted to increase the data and thereby allow a statistical analysis approach, which would refine the data obtained in this study.

The test cell design can be improved to eliminate the quiescent regions that can initiate nucleation and allow harvesting of crystallized salt to ensure it does not influence the ice crystallization process. Experiments can be conducted with the test cell positioned upright to mimic the original crystallizing units. This position could reduce the likelihood of salt scaling, as the salt would not settle on the HX plate, and thus reduce the subsequent ice nucleation on the scaled surfaces.

It is also recommended that different HX materials should be treated to have the same roughness when studying the effect of surface free energy. Previous studies have shown that differences in surface roughness affect the resulting scaling phenomenon. It becomes difficult to observe the effect of surface free energy independently from surface roughness (Förster and Bohnet, 1999). Instead of micro-blasting the surface for coating, using a technique such as spin coating could reduce the roughness of the coated surface.

It would also be beneficial to conduct studies on measuring the thermal and velocity boundary layer at the HX plate to observe the effect of the material property on the thickness of these regions, which ultimately affects the interactions at the interface.

The use of a high-speed, high-definition camera is recommended in future experiments. The high-quality imaging may help reduce errors in scaling rate analysis and allow precise characterisation of the ice scale morphologies. A high-speed camera may also allow for analysing the bulk crystals that move at high velocity.

8. References

Abdelmonem, A., Lützenkirchen, J. & Leisner, T. 2015. Probing ice-nucleation processes on the molecular level using second harmonic generation spectroscopy. *Atmospheric Measurement Techniques*. 8(8):3519–3526.

Albert, F., Augustin, W. & Scholl, S. 2011. Roughness and constriction effects on heat transfer in crystallization fouling. *Chemical Engineering Science*. 66(3):499–509.

Alizadeh, A., Yamada, M., Li, R., Shang, W., Otta, S., Zhong, S., Ge, L., Dhinojwala, A., Conway, K.R., Bahadur, V., Vinciquerra, A.J., Stephens, B. & Blohm, M.L. 2012. Dynamics of ice nucleation on water repellent surfaces. *Langmuir*. 28(6):3180–3186.

Andrews, E.H. & Lockington, N.A. 1983. The cohesive and adhesive strength of ice. *Journal of Materials Science*. 18(5):1455–1465.

Aspeling, B.J. 2019. Selective recovery of salts from a ternary eutectic system in EFC using seeding. University of Cape Town.

Aspenes, G., Hoeiland, S., Barth, T., Askvik, J.M., Kini, R.A. & Larsen, R. 2008. Petroleum hydrate deposition mechanisms: The influence of pipeline wettability. *6th Gas Hydrates International Conference [ICGH] (Vancouver, British Columbia, 7/6-10/2008) Proceedings*. (Icgh).

Beckmann, W. 2013. *Crystallization*. W. Beckmann, Ed. Weinheim, Germany: Wiley-VCH Verlag GmbH & Co. KGaA.

Bell, F.G., Bullock, S.E.T., Hälbich, T.F.J. & Lindsay, P. 2001. Environmental impacts associated with an abandoned mine in the Witbank Coalfield, South Africa. *International Journal of Coal Geology*. 45(2):195–216.

Bharathidasan, T., Kumar, S.V., Bobji, M.S., Chakradhar, R.P.S. & Basu, B.J. 2014. Effect of wettability and surface roughness on ice-adhesion strength of hydrophilic, hydrophobic and superhydrophobic surfaces. *Applied Surface Science*. 314:241–250.

Bi, Y., Cao, B. & Li, T. 2017. Enhanced heterogeneous ice nucleation by special surface geometry. *Nature Communications*. 8(May):1–7.

Björneholm, O., Hansen, M.H., Hodgson, A., Liu, L.M., Limmer, D.T., Michaelides, A., Pedevilla, P., Rossmeisl, J., Shen, H., Tocci, G., Tyrode, E., Walz, M.M., Werner, J. & Bluhm, H. 2016. Water at Interfaces. *Chemical Reviews*. 116(13):7698–7726.

Budair, M.O., Khan, M.S., Zubair, S.M., Sheikh, A.K. & Quddus, A. 1998. CaCO3 scaling in AISI 316 stainless steel tubes - Effect of thermal and hydraulic parameters on the induction time and growth rate. *Heat and Mass Transfer/Waerme- und Stoffuebertragung*. 34(2–3):163–170.

Carpenter, K. & Bahadur, V. 2015. Saltwater icephobicity: Influence of surface chemistry on saltwater icing. *Scientific Reports*. 5:1–11.

Cheong, W.C., Gaskell, P.H. & Neville, A. 2013. Substrate effect on surface adhesion/crystallisation of calcium carbonate. *Journal of Crystal Growth*. 363:7–21.

Crespí-Llorens, D., Martínez, P., Vicente, P. & Viedma, A. 2013. Effect of the axial scraping velocity on enhanced heat exchangers. *International Journal of Heat and Fluid Flow*. 44:265–275.

De Goede, R. & De Jong, E.. 1992. Heat transfer properties of a scraped-surface heat exchanger in the turbulent flow regime. *Chemical Engineering Science*. 48(8):1393–1404.

Dehkordi, S.K., Fazilati, M.A. & Hajatzadeh, A. 2015. Surface Scraped Heat Exchanger for cooling

Newtonian fluids and enhancing its heat transfer characteristics, a review and a numerical approach. *Applied Thermal Engineering*. 87:56–65.

Delly, G. 2012. The Michel-Lévy Interference Color Chart – Microscopy's magical color key. *Modern Microscopy Journal*. (2):1–32.

Diao, Y., Myerson, A.S., Hatton, T.A. & Trout, B.L. 2011. Surface design for controlled crystallization: The role of surface chemistry and nanoscale pores in heterogeneous nucleation. *Langmuir*. 27(9):5324–5334.

Dotan, A., Dodiuk, H., Laforte, C. & Kenig, S. 2009. The relationship between water wetting and ice adhesion. *Journal of Adhesion Science and Technology*. 23(15):1907–1915.

Doyle, J.D., Oldring, K., Churchley, J. & Parsons, S.A. 2002. Struvite formation and the fouling propensity of different materials. *Water Research*. 36(16):3971–3978.

Ensikat, H.J., Schulte, A.J., Koch, K. & Barthlott, W. 2009. Droplets on superhydrophobic surfaces: Visualization of the contact area by cryo-scanning electron microscopy. *Langmuir*. 25(22):13077–13083.

Fitzner, M., Sosso, G.C., Cox, S.J. & Michaelides, A. 2015. The Many Faces of Heterogeneous Ice Nucleation: Interplay between Surface Morphology and Hydrophobicity. *Journal of the American Chemical Society*. 137(42):13658–13669.

Förster, M. & Bohnet, M. 1999. Influence of the interfacial free energy crystal/heat transfer surface on the induction period during fouling. *International Journal of Thermal Sciences*. 38(11):944–954.

Förster, M., Augustin, W. & Bohnet, M. 1999. Influence of the adhesion force crystal/heat exchanger surface on fouling mitigation. *Chemical Engineering and Processing: Process Intensification*. 38(4–6):449–461.

Genceli, F.E. 2008. *Scaling-Up Eutectic Freeze Crystallization*. Available: http://resolver.tudelft.nl/uuid:c64d84d8-6552-4d3c-9c02-1d511c689c43.

Genceli, F.E. & Witkamp, G.J. 2008. Scaling-up eutectic freeze crystallization. Technische Universiteit Delft.

Genceli, F.E., Trambitas, D.O., Gärtner, R.S., Rodriguez, M. & Witkamp, G.J. 2005. 3Rdgeneration Cooled Disk Column Crystallizer and a Skid Mounted Unit for Eutectic Freeze Crystallization. *VDI Berichte*. 275(1901 II):855–860.

Genceli, F.E., Gärtner, R. & Witkamp, G.J. 2005. Development of eutectic freezing process for brine disposal. *Journal of Crystal Growth*. 275(1–2):e1369–e1372.

Gittens, G.J. 1969. Variation of surface tension of water with temperature. *Journal of Colloid And Interface Science*. 30(3):406–412.

Gutwald, T. & Mersmann, A. 1990. Batch cooling crystallization at constant supersaturation: Technique and experimental results. *Chemical Engineering & Technology*. 13(1):229–237.

Hare, E.F., Shafrin, E.G. & Zisman, W.A. 1954. Properties of films of adsorbed fluorinated acids. *Journal of Physical Chemistry*. 58(3):236–239.

Hasan, M. & Louhi-Kultanen, M. 2015. Ice growth kinetics modeling of air-cooled layer crystallization from sodium sulfate solutions. *Chemical Engineering Science*. 133:44–53.

Hasan, M., Rotich, N., John, M. & Louhi-Kultanen, M. 2017. Salt recovery from wastewater by air-cooled eutectic freeze crystallization. *Chemical Engineering Journal*. 326:192–200.

Hassan, M.F., Lee, H.P. & Lim, S.P. 2010. The variation of ice adhesion strength with substrate surface roughness. *Measurement Science and Technology*. 21(7).

Helalizadeh, A., Müller-Steinhagen, H. & Jamialahmadi, M. 2000. Mixed salt crystallisation fouling. *Chemical Engineering and Processing: Process Intensification*. 39(1):29–43.

Heydari, G., Sedighi Moghaddam, M., Tuominen, M., Fielden, M., Haapanen, J., Mäkelä, J.M. & Claesson, P.M. 2016. Wetting hysteresis induced by temperature changes: Supercooled water on hydrophobic surfaces. *Journal of Colloid and Interface Science*. 468:21–33.

Himawan, C., Kramer, H.J.M. & Witkamp, G.J. 2006. Study on the recovery of purified MgSO4·7H2O crystals from industrial solution by eutectic freezing. *Separation and Purification Technology*. 50(2):240–248.

Hodgson, A. & Haq, S. 2009. Water adsorption and the wetting of metal surfaces. *Surface Science Reports*. 64(9):381–451.

Kapembwa, M., Rodríguez-Pascual, M. & Lewis, A.E. 2014. Heat and mass transfer effects on ice growth mechanisms in pure water and aqueous solutions. *Crystal Growth and Design*. 14(1):389–395.

Kazi, S.N., Duffy, G.G. & Chen, X.D. 2010. Mineral scale formation and mitigation on metals and a polymeric heat exchanger surface. *Applied Thermal Engineering*. 30(14–15):2236–2242.

Keysar, S., Semiat, R., Hasson, D. & Yahalom, J. 1994. Effect of Surface Roughness on the Morphology of Calcite Crystallizing on Mild Steel. *Journal of Colloid and Interface Science*. (162):311–319.

Khan, M.S. 2005. Deposition of sodium carbonate and sodium sulfate in supercritical water oxide systems and its mitigation. The University of British Columbia.

Kreder, M.J., Alvarenga, J., Kim, P. & Aizenberg, J. 2016. Design of anti-icing surfaces: Smooth, textured or slippery? *Nature Reviews Materials*. 1(1).

Kulinich, S.A. & Farzaneh, M. 2009. Ice adhesion on super-hydrophobic surfaces. *Applied Surface Science*. 255(18):8153–8157.

Lang, W. 1968. Nomarski differential interference-contrast imaging. *Zeiss Information*. (70):114–120.

Langham, E.J. & Mason, J. 1958. The heterogeneous and homogeneous nucleation of supercooled water. *Proceedings of the Royal Society of London. Series A. Mathematical and Physical Sciences*. 247(1251):493–504.

Lei, C., Peng, Z., Day, T., Yan, X., Bai, X. & Yuan, C. 2011. Experimental observation of surface morphology effect on crystallization fouling in plate heat exchangers. *International Communications in Heat and Mass Transfer*. 38(1):25–30.

Lewis, A., Nathoo, J., Reddy, T., Randall, D., Zibi, L. & Jivanji, R. 2010. *Novel technology for recovery of water and solid salts from hypersaline brines :* Cape Town.

Lewis, A.E., Seckler, M.M., Kramer, H. & Van Rosmalen, G. 2015. *Industrial crystallization: Fundamentals and applications*. Cambridge: Cambridge University Press.

Leyland, D., Chivavava, J. & Lewis, A.E. 2019. Investigations into ice scaling during eutectic freeze crystallization of brine streams at low scraper speeds and high supersaturation. *Separation and Purification Technology*. 220(March):33–41.

Li, J., Tilbury, C.J., Kim, S.H. & Doherty, M.F. 2016. A design aid for crystal growth engineering. *Progress in Materials Science*. 82:1–38.

Liu, J., Zhu, C., Liu, K., Jiang, Y., Song, Y., Francisco, J.S., Zeng, X.C. & Wang, J. 2017. Distinct ice patterns on solid surfaces with various wettabilities. *Proceedings of the National Academy of Sciences of the United States of America*. 114(43):11285–11290.

Lupi, L. & Molinero, V. 2014. Does hydrophilicity of carbon particles improve their ice nucleation ability? *Journal of Physical Chemistry A*. 118(35):7330–7337.

Lupi, L., Hudait, A. & Molinero, V. 2014. Heterogeneous nucleation of ice on carbon surfaces. *Journal of the American Chemical Society*. 136(8):3156–3164.

Lupi, L., Peters, B. & Molinero, V. 2016. Pre-ordering of interfacial water in the pathway of heterogeneous ice nucleation does not lead to a two-step crystallization mechanism. *Journal of Chemical Physics*. 145(21).

Lv, F.Y. & Zhang, P. 2016. Drag reduction and heat transfer characteristics of water flow through the tubes with superhydrophobic surfaces. *Energy Conversion and Management*. 113:165–176.

MacAdam, J. & Parsons, S.A. 2004. Calcium carbonate scale formation and control. *Reviews in Environmental Science and Biotechnology*. 3(2):159–169.

Martínez, D.S., Solano, J.P., Illán, F. & Viedma, A. 2014. Analysis of heat transfer phenomena during ice slurry production in scraped surface plate heat exchangers. *International Journal of Refrigeration*. 48:221–232.

Matsumoto, K. & Kobayashi, T. 2007. Fundamental study on adhesion of ice to cooling solid surface. *International Journal of Refrigeration*. 30(5):851–860.

Matsumoto, K., Akimoto, T. & Teraoka, Y. 2010. Study of scraping force of ice growing on cooling solid surface. *International Journal of Refrigeration*. 33(2):419–427.

Matsumoto, K., Akaishi, M., Teraoka, Y., Inaba, H. & Koshizuka, M. 2012. Investigation of method for measuring adhesion force of ice in nano/micro scale by using SPM. *International Journal of Refrigeration*. 35(1):130–141.

Mattox, D.M. 2010. *Handbook of Physical Vapor Deposition (PVD) Processing*. Kidlington: Elsevier.

Meng, S., Wang, E.G. & Gao, S. 2004. Water adsorption on metal surfaces: A general picture from density functional theory studies. *Physical Review B - Condensed Matter and Materials Physics*. 69(19):1–13.

Moaven, K., Rad, M. & Taeibi-Rahni, M. 2013. Experimental investigation of viscous drag reduction of superhydrophobic nano-coating in laminar and turbulent flows. *Experimental Thermal and Fluid Science*. 51:239–243.

Mullin, J.W. 2001. *Crystallization*. 4th ed. London: Butterworth-Heinemann.

Murphy, D.B., Spring, K.R., Fellers, T.J. & Davidson, M.W. 2020. *Principles of Birefringence | MicroscopyU*. Available: https://www.microscopyu.com/techniques/polarized-light/principles-of-birefringence [2020, March 21].

Myerson, A.S. 2002. *Handbook of Industrial Crystallization*. 2nd ed. London: Butterworth-Heinemann.

Némethy, G. & Scheeaga, H.A. 1962. Structure of water and hydrophobic bonding in proteins. I. A model for the thermodynamic properties of liquid water. *The Journal of Chemical Physics*. 36(12):3382–3400.

Nishino, T., Meguro, M., Nakamae, K., Matsushita, M. & Ueda, Y. 1999. The lowest surface free energy based on -CF3 alignment. *Langmuir*. 15(13):4321–4323.

Nosonovsky, M. & Hejazi, V. 2012. Why superhydrophobic surfaces are not always icephobic. *ACS*

Nano. 6(10):8488–8491.

Ozbay, S. & Erbil, H.Y. 2016. Ice accretion by spraying supercooled droplets is not dependent on wettability and surface free energy of substrates. *Colloids and Surfaces A: Physicochemical and Engineering Aspects*. 504:210–218.

Pääkkönen, T.M., Riihimäki, M., Simonson, C.J., Muurinen, E. & Keiski, R.L. 2015. Modeling CaCO3crystallization fouling on a heat exchanger surface - Definition of fouling layer properties and model parameters. *International Journal of Heat and Mass Transfer*. 83:84–98.

Petrenko, V.F. & Whitworth, R.W. 2002. *Physics of Ice*. New York: Oxford University Press.

Pronk, P., Infante Ferreira, C.A. & Witkamp, G.J. 2008. Prevention of crystallization fouling during eutectic freeze crystallization in fluidized bed heat exchangers. *Chemical Engineering and Processing: Process Intensification*. 47(12):2140–2149.

Qin, F.G.F., Russell, A.B., Chen, X.D. & Robertson, L. 2003. Ice fouling on a subcooled metal surface examined by thermo-response and electrical conductivity. *Journal of Food Engineering*. 59(4):421–429.

Rahimi, M., Afshari, A., Fojan, P. & Gurevich, L. 2015. The effect of surface modification on initial ice formation on aluminum surfaces. *Applied Surface Science*. 355:327–333.

Randall, D.G. & Nathoo, J. 2015. A succinct review of the treatment of Reverse Osmosis brines using Freeze Crystallization. *Journal of Water Process Engineering*. 8:186–194.

Randall, D.G., Nathoo, J. & Lewis, A.E. 2011. A case study for treating a reverse osmosis brine using Eutectic Freeze Crystallization-Approaching a zero waste process. *Desalination*. 266(1–3):256–262.

Reddy, S.T., Lewis, A.E., Witkamp, G.J., Kramer, H.J.M. & van Spronsen, J. 2010. Recovery of Na2SO4·10H2O from a reverse osmosis retentate by eutectic freeze crystallisation technology. *Chemical Engineering Research and Design*. 88(9):1153–1157.

Rodriguez Pascual, M., Genceli, F.E., Trambitas, D.O., Evers, H., Van Spronsen, J. & Witkamp, G.J. 2010. A novel scraped cooled wall crystallizer. Recovery of sodium carbonate and ice from an industrial aqueous solution by eutectic freeze crystallization. *Chemical Engineering Research and Design*. 88(9):1252–1258.

Seo, J. & Mani, A. 2016. On the scaling of the slip velocity in turbulent flows over superhydrophobic surfaces. *Physics of Fluids*. 28(2).

Sheikholeslami, R. 2004. Assessment of the scaling potential for sparingly soluble salts in RO and NF units. *Desalination*. 167(1–3):247–256.

Sojoudi, H., Wang, M., Boscher, N.D., McKinley, G.H. & Gleason, K.K. 2016. Durable and scalable icephobic surfaces: similarities and distinctions from superhydrophobic surfaces. *Soft Matter*. 12(7):1938–1963.

Sojoudi, H., Nemani, S.K., Mullin, K.M., Wilson, M.G., Aladwani, H., Lababidi, H. & Gleason, K.K. 2019. Micro-/nanoscale approach for studying scale formation and developing scale-resistant surfaces. *ACS Applied Materials and Interfaces*. 11(7):7330–7337.

Sørensen, B.E. 2013. A revised Michel-Lévy interference colour chart based on first-principles calculations. *European Journal of Mineralogy*. 25(1):5–10.

Stepakoff, G.L., Siegelman, D., Johnson, R. & Gibson, W. 1974. Development of a eutectic freezing process for brine disposal. *Desalination*. 15(1):25–38.

Sunagawa, I. 2007. *Crystals : Growth, morphology, and perfection*. Cambridge University Press.

Thürmer, K. & Bartelt, N.C. 2008. Growth of multilayer ice films and the formation of cubic ice imaged with STM. *Physical Review B - Condensed Matter and Materials Physics*. 77(19):1–10.

Tourkine, P., Merrer, M.L. & Quéré, D. 2009. Delayed freezing on water repellent materials. *Langmuir*. 25(13):7214–7216.

Vaessen, R., Seckler, M. & Witkamp, G.J. 2003. Eutectic Freeze Crystallization with an Aqueous KNO3 - HNO3 Solution in a 100-L Cooled-Disk Column Crystallizer. *Industrial and Engineering Chemistry Research*. 42:4874–4880.

Vaessen, R.J.C., Himawan, C. & Witkamp, G.J. 2002. Scale formation of ice from electrolyte solutions on a scraped surface heat exchanger plate. *Journal of Crystal Growth*. 237–239(1-4 III):2172–2177.

Vaessen, R.J.C., Janse, B.J.H., Seckler, M.M. & Witkamp, G.J. 2003. Evaluation of the performance of a newly developed eutectic freeze crystallizer: Scraped cooled wall crystallizer. *Chemical Engineering Research and Design*. 81(10):1363–1372.

Vaessen, R.J.C., Seckler, M.M. & Witkamp, G.J. 2004. Heat transfer in scraped eutectic crystallizers. *International Journal of Heat and Mass Transfer*. 47(4):717–728.

Vali, G. 2008. Repeatability and randomness in heterogeneous freezing nucleation. *Atmospheric Chemistry and Physics*. 8(16):5017–5031.

Van der_Ham, F., Witkamp, G.J., de Graauw, J. & van Rosmalen, G.M. 1998. Eutectic freeze crystallization: Application to process streams and waste water purification. *Chemical Engineering and Processing: Process Intensification*. 37(2):207–213.

Van't Land, C. 2004. Melt Crystallization. In *Industrial Crystallization of Melts*. New York: CRC Press. 183–240.

Verdaguer, A., Sacha, G.M., Bluhm, H. & Salmeron, M. 2006. Molecular structure of water at interfaces: Wetting at the nanometer scale. *Chemical Reviews*. 106(4):1478–1510.

Xu, W., Lan, Z., Peng, B.L., Wen, R.F. & Ma, X.H. 2015. Effect of surface free energies on the heterogeneous nucleation of water droplet: A molecular dynamics simulation approach. *Journal of Chemical Physics*. 142(5).

Yamamoto, K. 2012. Optical visualization of acoustic fields: The schlieren technique, the Fresnel method and the photoelastic method applied to ultrasonic transducers. In *Ultrasonic Transducers: Materials and Design for Sensors, Actuators and Medical Applications*. Elsevier Inc. 314–328.

Yang, M. & Dai, H.L. 2003. Heterogeneous nucleation and wetting of water thin films on a metal surface: A study by optical second harmonic generation. *Journal of Chemical Physics*. 118(11):5106–5114.

Yang, Q., Liu, Y., Gu, A., Ding, J. & Shen, Z. 2002. Investigation of induction period and morphology of CaCO3 fouling on heated surface. *Chemical Engineering Science*. 57(6):921–931.

Yin, L., Xia, Q., Xue, J., Yang, S., Wang, Q. & Chen, Q. 2010. In situ investigation of ice formation on surfaces with representative wettability. *Applied Surface Science*. 256(22):6764–6769.

Zou, M., Beckford, S., Wei, R., Ellis, C., Hatton, G. & Miller, M.A. 2011. Effects of surface roughness and energy on ice adhesion strength. *Applied Surface Science*. 257(8):3786–3792.

A. Appendix

A.1. Test cell design specifications

Front View

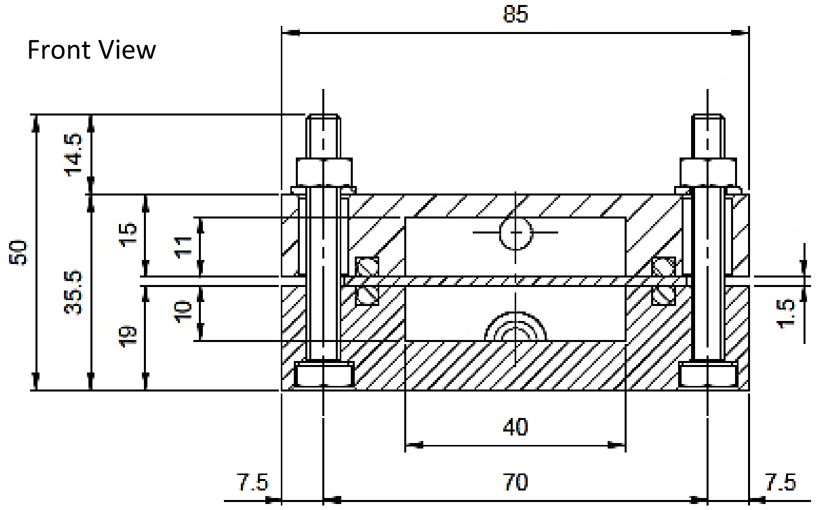

Top View

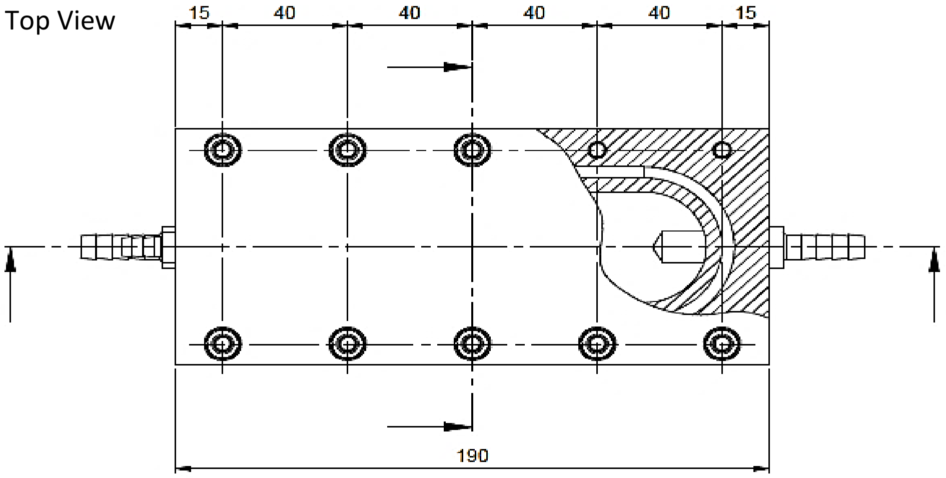

Side View

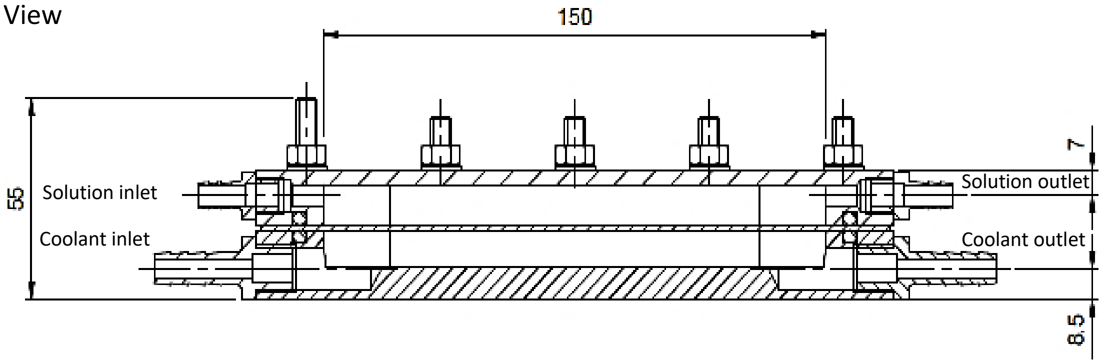

Figure A.1: *Crystallizer test cell from a cross-section front view, the top view, the side view. All measurements are in mm.*

A.2. Heat exchanger material properties

***Table A.1**: Metals used and their properties as received from the manufacturer*

Metals	Thermal Conductivity (W/mK)*	Surface Energy (mJ.m $^{-2}$)$^{\#}$	Roughness (R_q)$^{+}$	Composition (%)~	
Copper	386	50	63.60 ± 6	Cu	99.993
Aluminium (1050)	204	48	18.53 ± 4	Al	99.57
				Fe	0.32
				Si	0.07
Brass (30/70)	111	35	69.55 ± 9	Cu	68-72
				Zn	28-32
SS 316L	12-45	40	120.50 ± 17	Fe	60
				Cr	14-18
				Ni	7-8
				Mo	3-2
				Mn	1.3-2

**www.Engineeringtoolbox.com, $^{\#}$* (Förster and Bohnet, 1999)*, $^{+}$ AFM Analysis, $^{\sim}$ SEM-EDS analysis.*

***Table A.2**: Heat exchanger plate roughness*

	Brass	Aluminium	Copper	SS316 (primary)	SS316 (coated)	SS316 (rough)
Rq (nm)	69.55 ± 9	18.53 ± 4	63.60 ± 6	120.50 ± 17	87.45± 1	446.5± 9

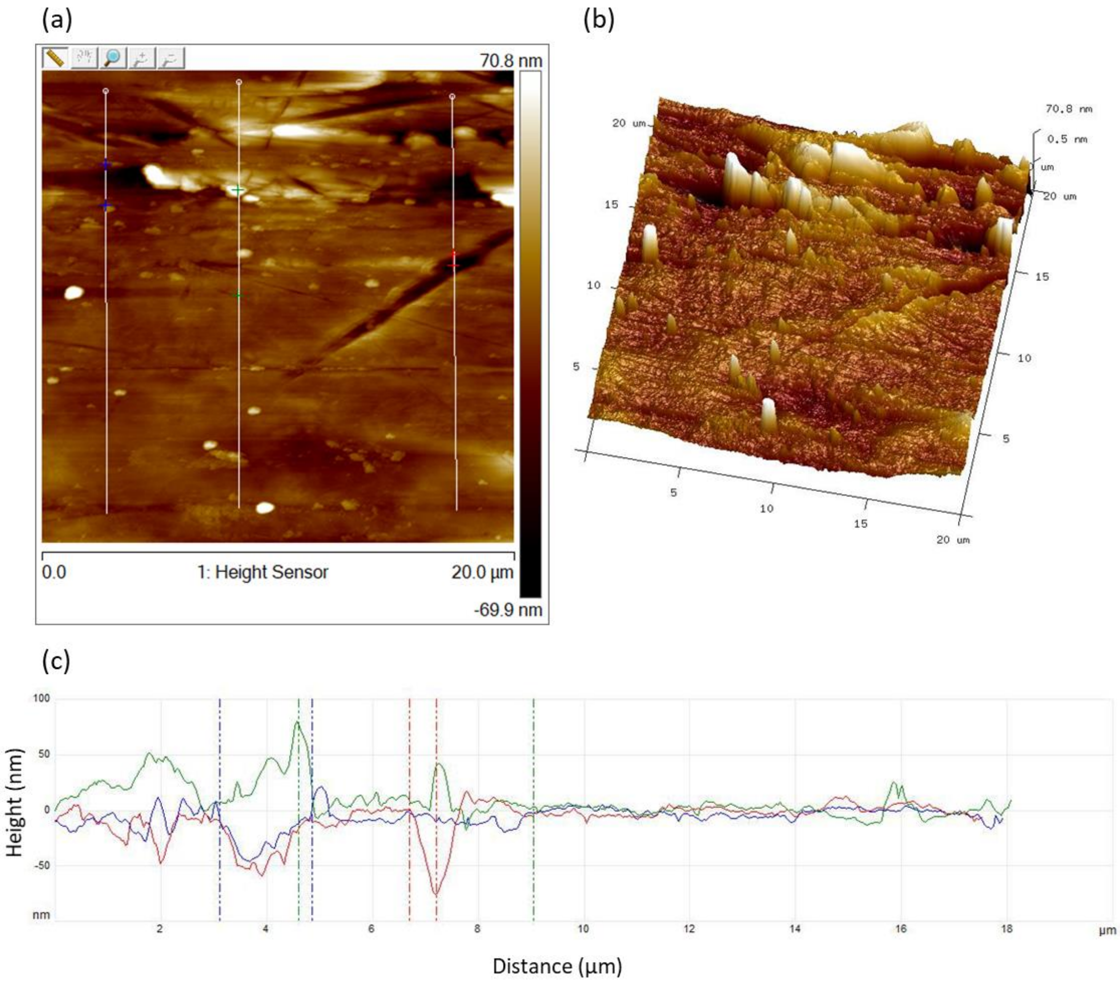

Figure A.2*: Atomic Force Microscopy topography images of Aluminium, from the manufacturer, on a 400µm*^{2} *area. Image (a) is the top view and (b) is the 3D view and (c) represents the height variations along the line segments in image (a).*

The Aluminium surface was analysed on three randomly selected, 400 µm^{2} areas, represented by *Figure A.2* 2D image (a) and 3D image (b). The average root-mean-square roughness (Rq) of the analysed area, was 14.7 nm. The surface was characterised by minimal peaks and troughs, where the observed peaks were due to the protective layer used to cover the material prior to use, and the deep troughs were due to mishandling of the materials during transportation. Therefore, *Figure A.2* (c) represents this variation graphically. From a distance 0 to 8 µm, the surface peaks and troughs due to external impacts are indicated. After 8µm, the surfaces unobstructed topography is shown. It is represented by minimal roughness peak height and spacings, as well as minimal waviness height and spacing. This surface analysis shows that Aluminium was the smoothest surface used in this investigation.

The 2D height image shows that the highest peak in the analysed area had an amplitude of 70.8 nm and the deepest valley had an amplitude of 69.9 nm. These measurements indicate that this HX plate provided a surface that would allow for a uniform formation of the most uniform ice crystal lattice, which would result in higher regions of immobile water molecules with longer induction times. This material has the smoothest topography which may have reduced the sites for local supersaturation and peaks for adhesion of bulk crystals.

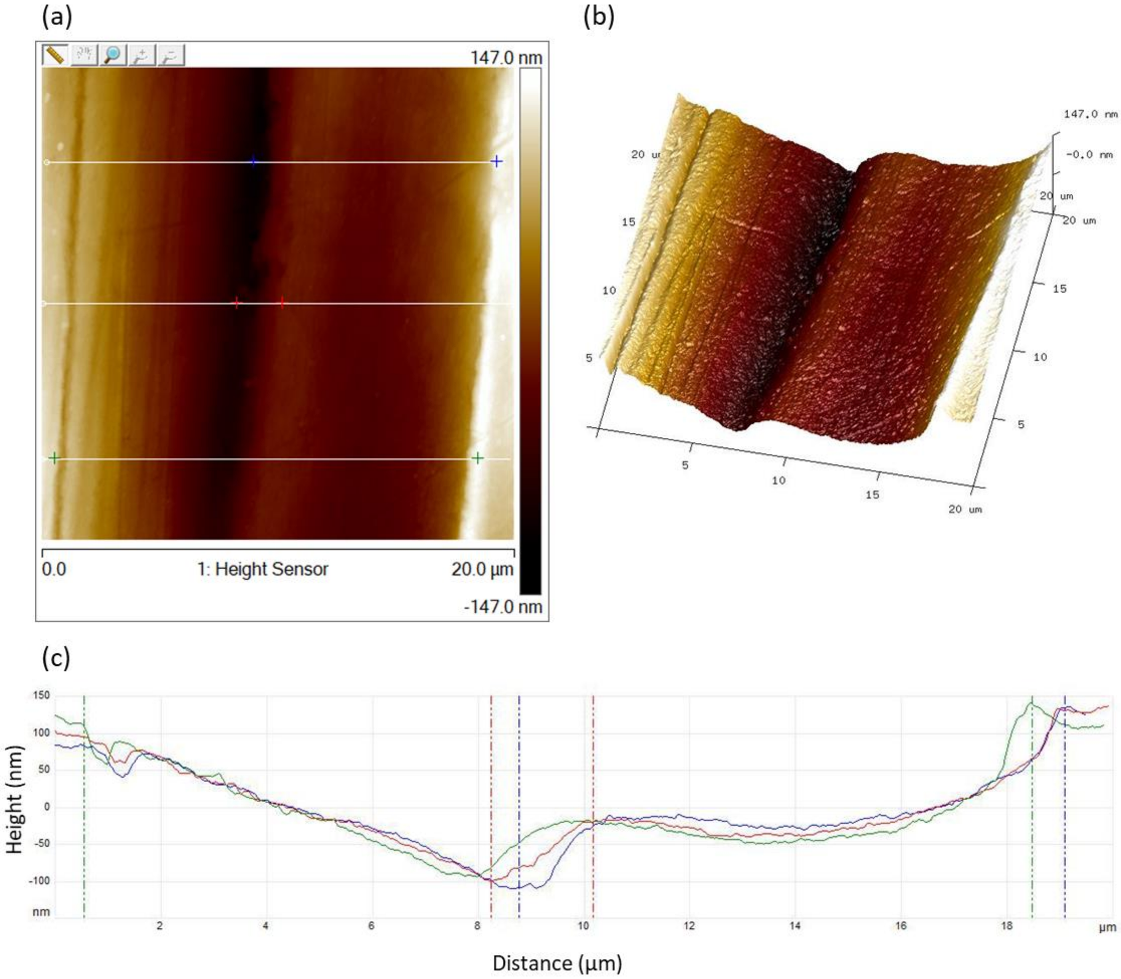

Figure A.3: *Atomic Force Microscopy topography images of Brass, from the manufacturer, on a 400µm^2 area. Image (a) is the top view and (b) is the 3D view and (c) represents the height variations along the line segments in image (a)*

The Brass surface was analysed on three randomly selected, 400 µm^2 areas, represented by *Figure A.3* (a) and (b). The average root-mean-square roughness (Rq) of the analysed area, was 57.10 nm. The surface was characterised by roughness heights and widths which are not very pronounced. The waviness height and width of the surface is highly pronounced, as indicated by the 3D image.

The 2D height image shows that the highest peak in the analysed area had an amplitude of 147 nm and the deepest valley had one of 147 nm. *Figure A.3*(c) indicates the high peak to peak distance for the Brass plate. This indicates that this HX plate did not provide areas for localised supersaturations. Instead, the waviness spacing could have contributed to increasing the turbulence of the solution closer to the HX surface. This was the case with the Brass plate, in addition to the lower surface energy, which increased the motion of the fluid close to the surface by drag reduction. This property of significant waviness spacing could have also contributed to the efficiency that was observed in the heat transfer when using the Brass plate.

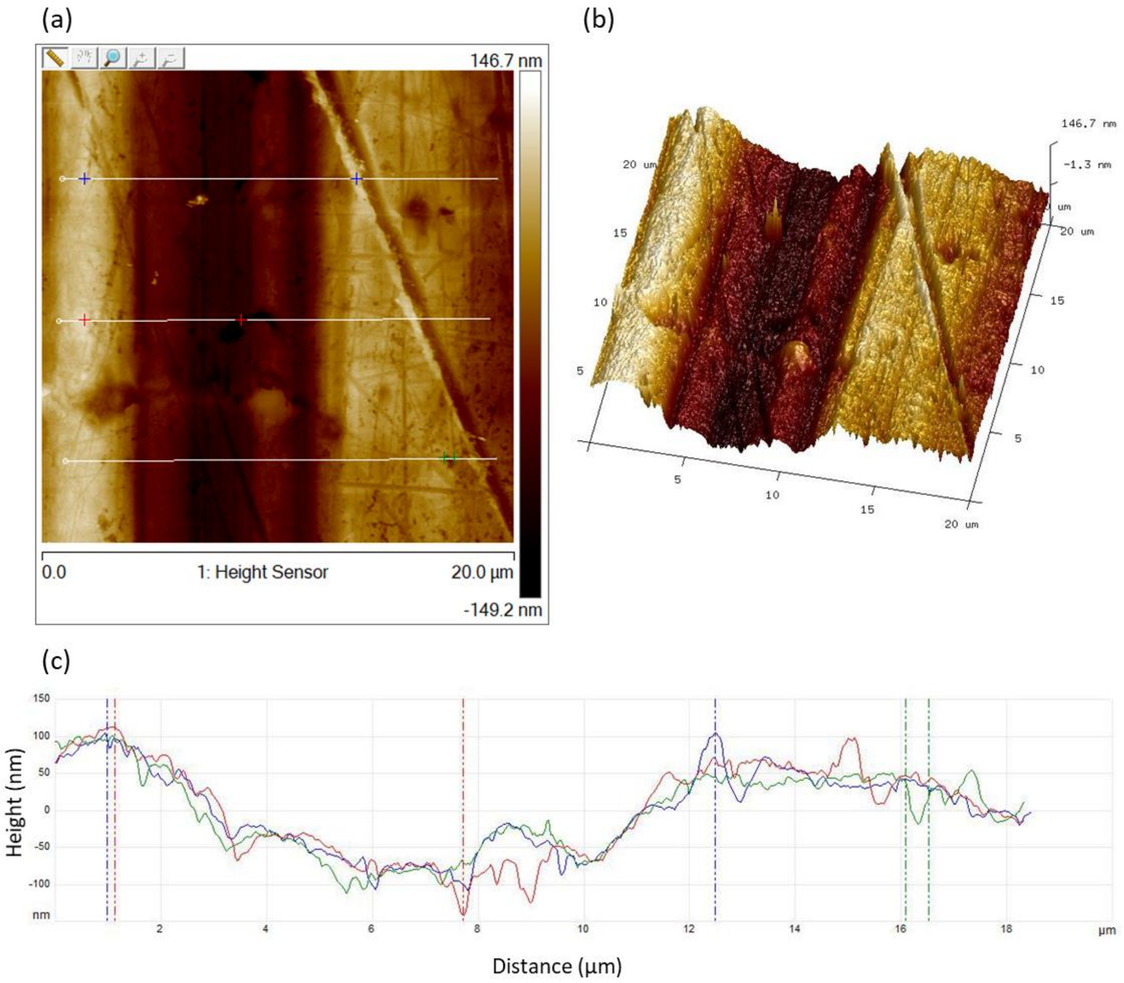

Figure A.4: *Atomic Force Microscopy topography images of Copper, from the manufacturer, on a 400µm² area. Image (a) is the top view and (b) is the 3D view and (c) represents the height variations along the line segments in image (a).*

The Copper surface was analysed on three randomly selected, 400 µm² areas, represented by *Figure A.4* (a) and (b). The average root-mean-square roughness (Rq) of the analysed area above, was 55.1 nm. The surface was characterised by roughness heights and widths that were slightly more pronounced than those on the Brass plate. The 2D height image shows that the highest peak in the analysed area had an amplitude of 146.7 nm and the deepest valley one of 149.2 nm. However, the waviness height and width was similar to that of the Brass, as indicated by the 3D image. This similarity could be a result of similar manufacturing processes.

The Copper HX plate surface topography resembled that of the Brass plate, in that they were both characterised by having a distinct waviness spacing. This, as discussed for Brass, may have had a positive influence in the heat transfer from the surface into the bulk solution. Although this benefit was not as clear in the case of Copper, the effect of surface energy is still shown. Copper has a higher surface free energy than Brass, therefore even though it has a similar waviness, and roughness which was known to assist in bulk mixing of the solution, the supersaturation level was found to be lower than that reached by Brass at similar heat fluxes. This result helped to increase the system bulk supersaturation.

It is important to note that the surface roughness profiles of the Brass and Copper plates were comparable. This similarity implies that the differences seen in the ice scaling induction times, scaling modes and scaling rates at similar heat fluxes could be attributed to the materials surface energies. From the results obtained, it can be said that the scaling induction time increased with a material of lower surface energy, and the scaling modes differed, resulting in a decreased scaling rate horizontally across the HX plate. Additionally, the bulk crystallization and higher supersaturations levels observed when using the Brass plate indicated the efficiency of heat removal by the system because of the shorter interaction time between the solution and HX surface.

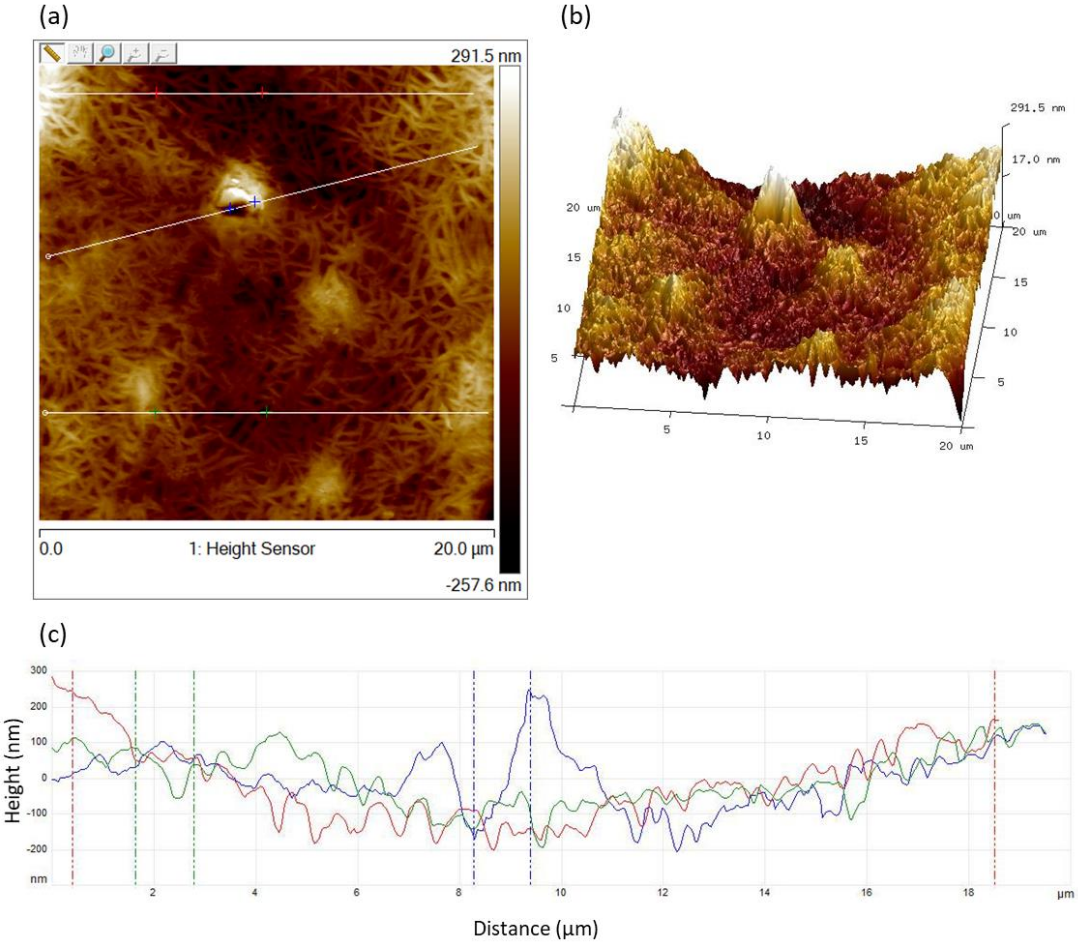

Figure A.5: *Atomic Force Microscopy topography images of PTFE-coated SS316 on a 400µm^2 area. Image (a) is the top view, (b) is the 3D view and (c) represents the height variations along the line segments in image (a).*

The coated surface was analysed on three randomly selected, 400 µm^2 areas, represented by Figure A.5 (a) and (b). The average root-mean-square roughness (Rq) of the analysed areas, was 72.9 nm. This was a decrease of approximately 33 % decrease in the average roughness from the primary SS316 surface. The surface was characterised by a grainy form of roughness, resembling that of a honeycomb. There were areas where there seemed to have been an error in the coating process, or the roughening process, which resulted in some tall peaks that were hollow. These peaks ranged in size, but not all were hollow. These peaks spread randomly across the surface. They could have led to increased adhesion sites which could have exacerbated the scaling process.

The 2D height image shows that the highest peak in the analysed area had an amplitude of 291.5 nm and the deepest valley one of 257.6 µm. The surface topography indicated roughness height and spacing that was more frequent, as indicated by *Figure A.5*(c). It is therefore important that a coating process which can produce a smoother surface is used in further investigations to prevent adhesion of bulk crystals on the peaks formed during the coating process. The coated SS316 surface was smoother than the primary surface, which was unexpected since it went through a process of micro blasting prior to coating. The coating soothed out the increased roughness created by micro-blasting and eliminated the crevices innate to the primary SS316. This was beneficial to the scaling problem, as elimination of the sharp crevices by micro blasting eliminated the areas of possible local supersaturation.

The unexpected result of high salt deposition on a surface of lower surface energy was attributed to the material roughness, as well as the longer ice scaling induction times. These longer induction times allowed more salt to adhere to the peaks of the surface prior to ice scaling. Therefore, despite the positive effect that the lower surface energy provided, by increasing the ice scaling induction times, the inherently high surface roughness drove crystallizing salt particles to adhere to the peaks of the surface, leading to severe salt scaling despite the lower surface energy.

Therefore, it seems that sodium sulphate can become a scaling agent in the EFC system on surfaces of a specific form of roughness, because the primary surface, although categorised as rough, did not result in salt scaling. This difference indicated that the crevices on the primary SS316 did not encourage salt scaling, whereas the peaks that were created by roughening the surface-enhanced salt adhesion.

A.3. Induction and Temperature Graphs

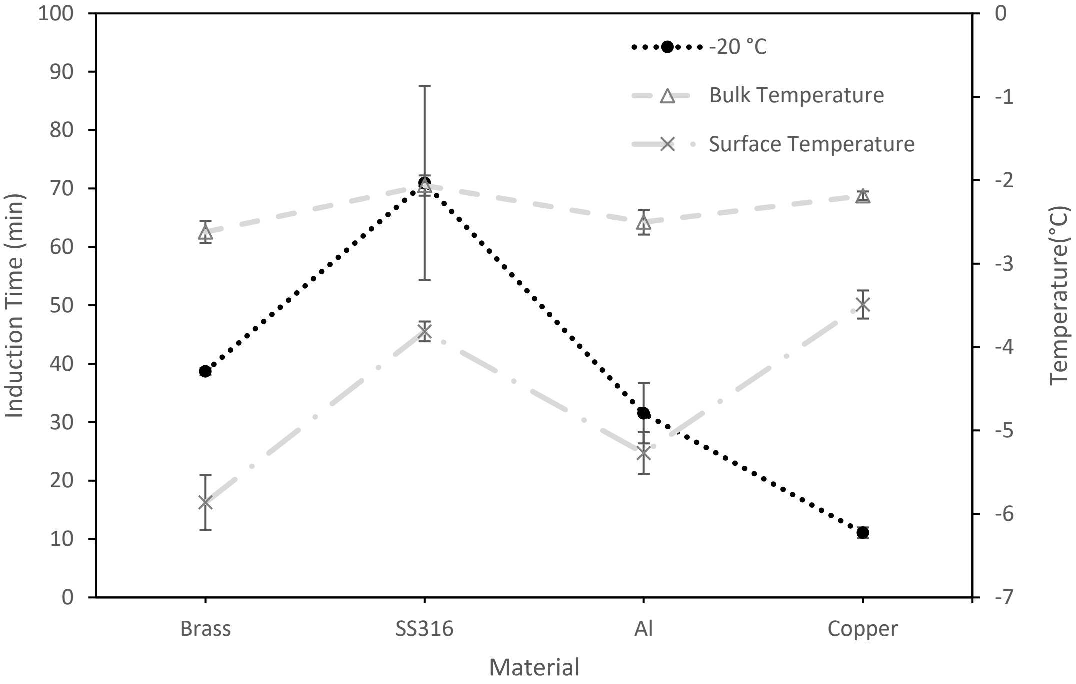

***Figure A.6**: Scaling induction times obtained when using different HX materials, at a coolant set temperature of -20°C and their corresponding temperatures at nucleation.*

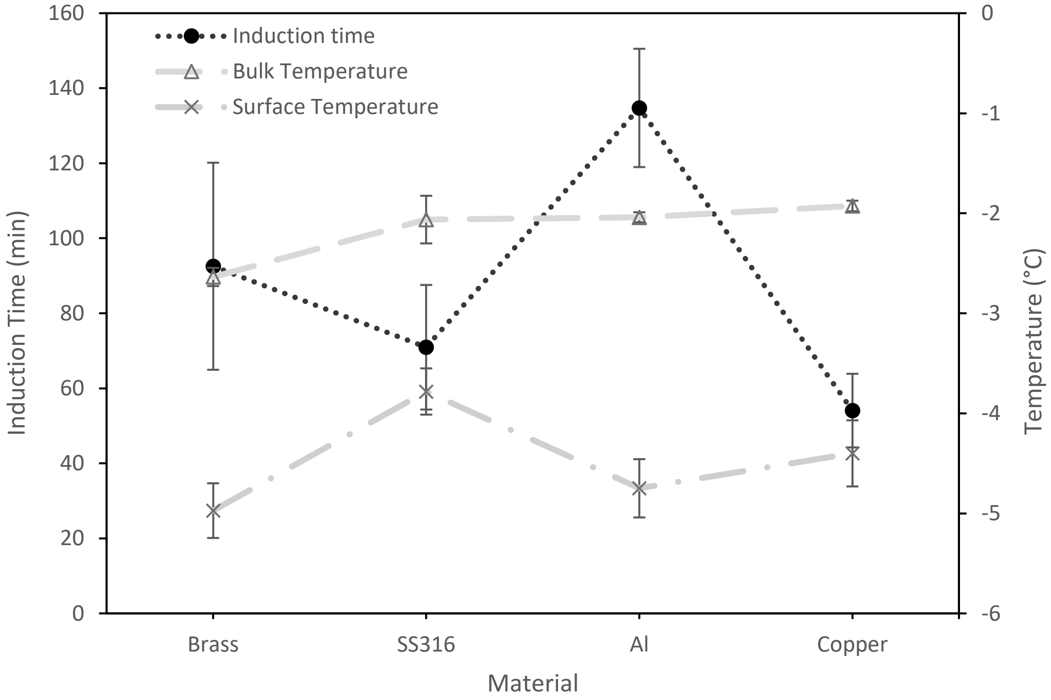

***Figure A.7:** Effect of surface properties on the scaling induction time and the bulk and surface temperatures at nucleation, operating at similar heat fluxes.*

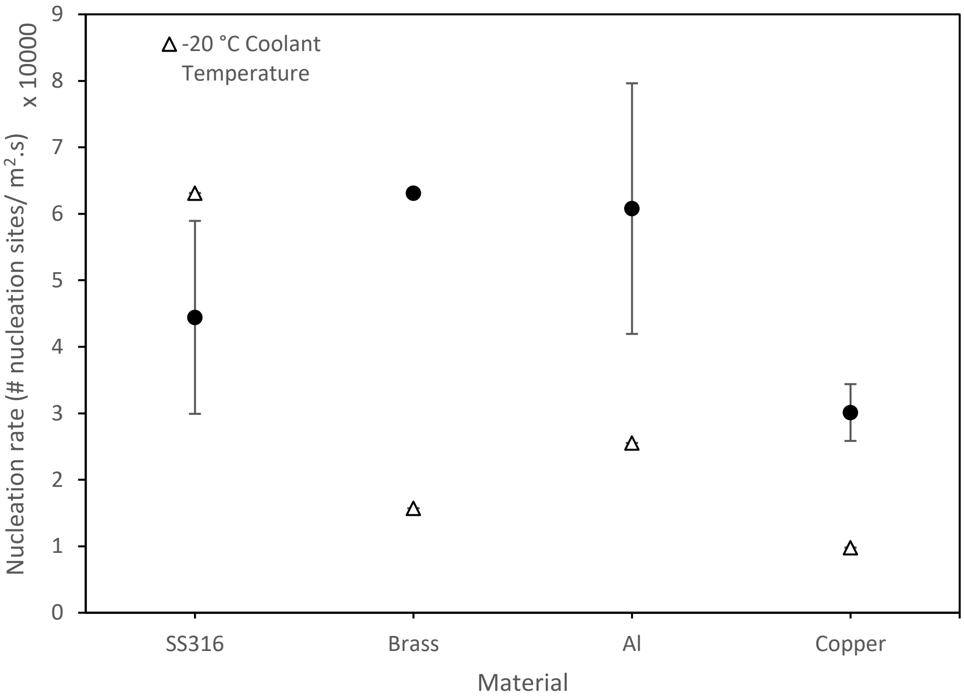

Figure A.8: *Average ice heterogeneous nucleation rates on the different metals at operating temperatures of -20°C and at similar heat fluxes*

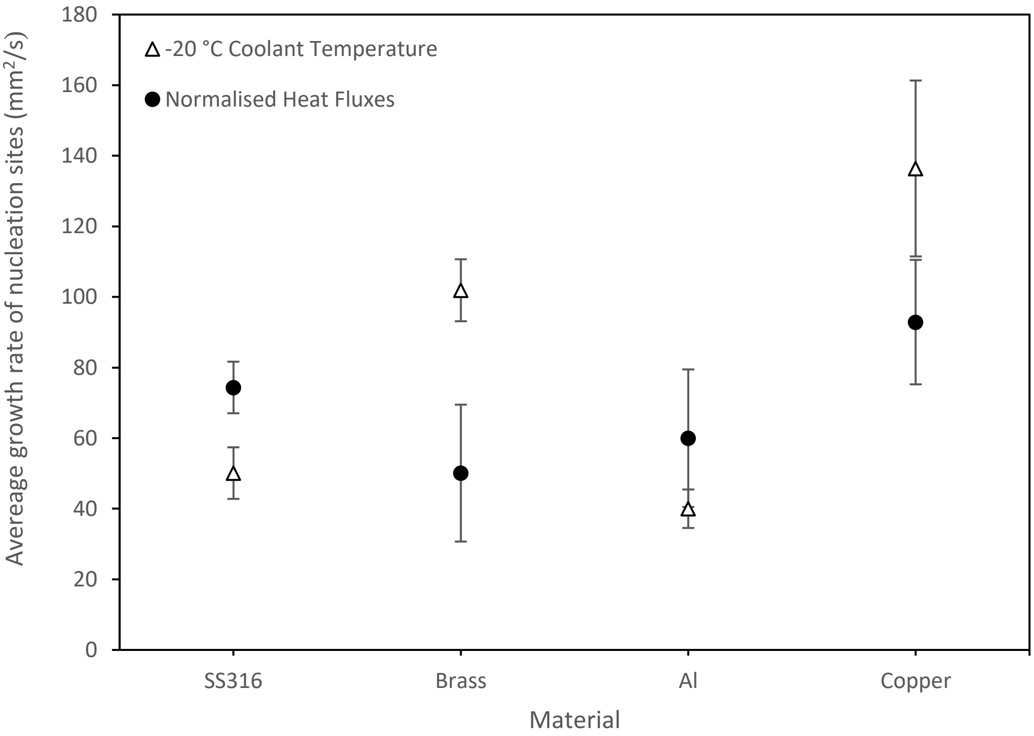

Figure A.9: *Average growth rate of nucleation sites formed on the surface of the different materials at an operating a temperature of-20°C and at similar heat fluxes.*

A.4. Michel-Lévy Interference colour chart.

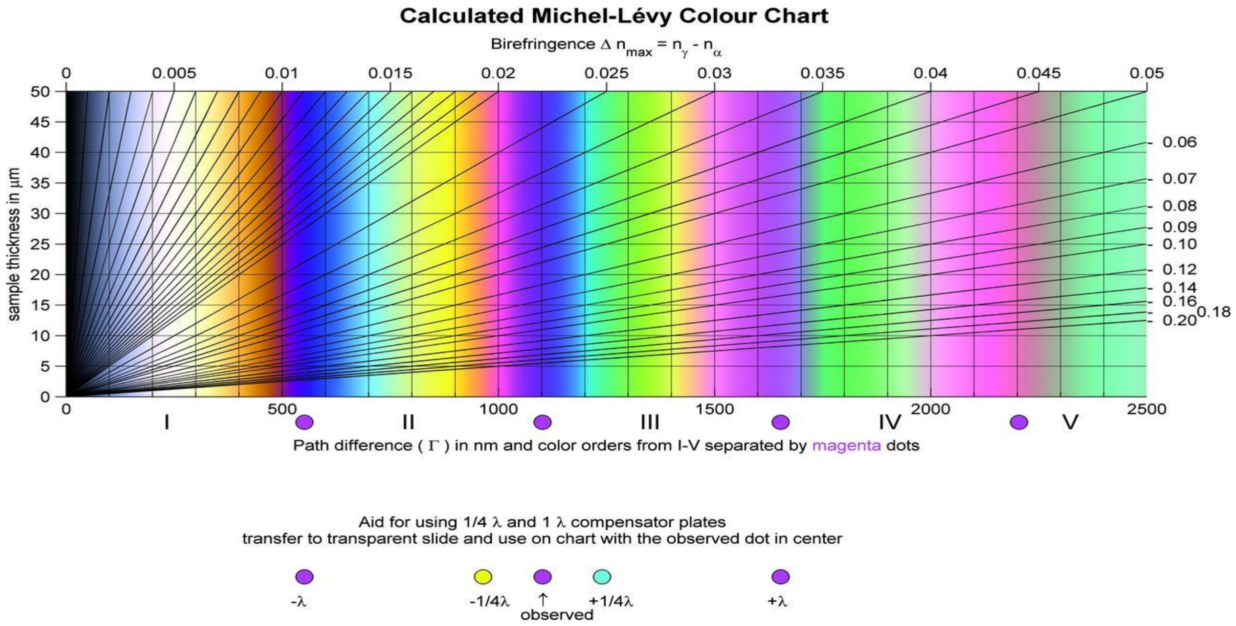

Figure A.10: *Michel-Lévy chart. Markers for use of 1-lambda and ¼-lambda plates added.* (Delly, 2012).

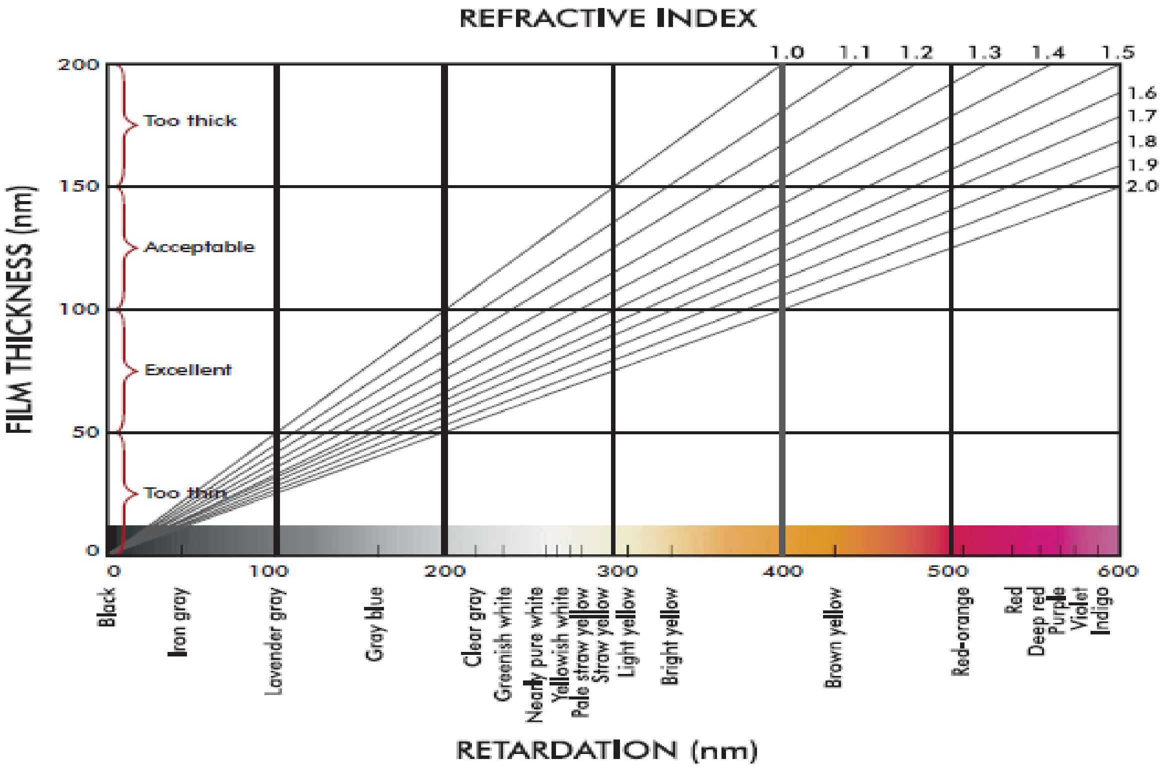

Figure A.11: *Relationship between thin film thickness, refractive index and retardation. (Delly, 2012)*

A.5. DIC images

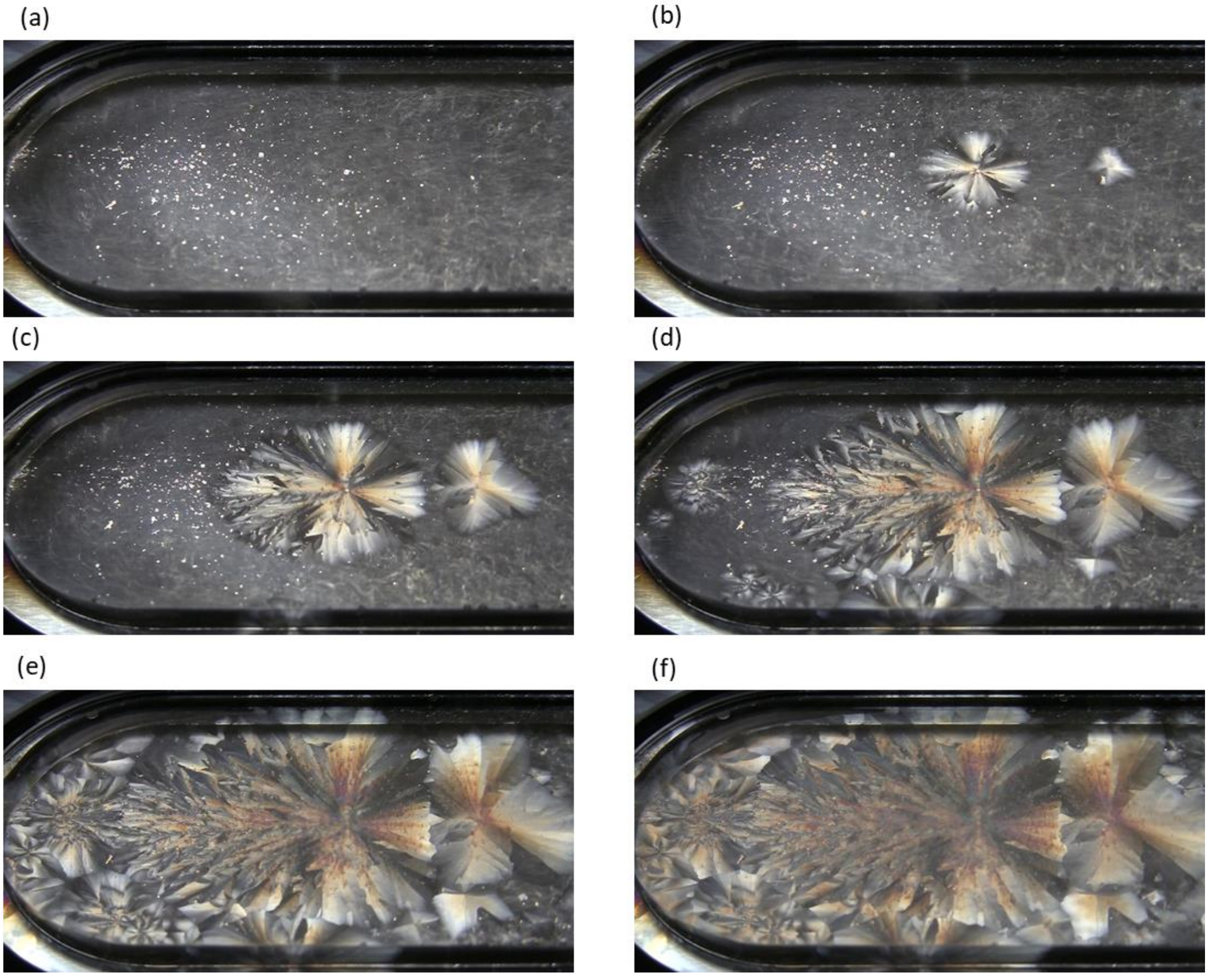

Figure A.12: *DIC photographs of ice scale formation on Aluminium at normalised thermal conductivities, where (a) is the frame before an initial nucleation site is detected and frames (b) to (f) are 0.4s, 0.8s, 1,2s, 1.6s and 2s after the nucleation site is detected.*

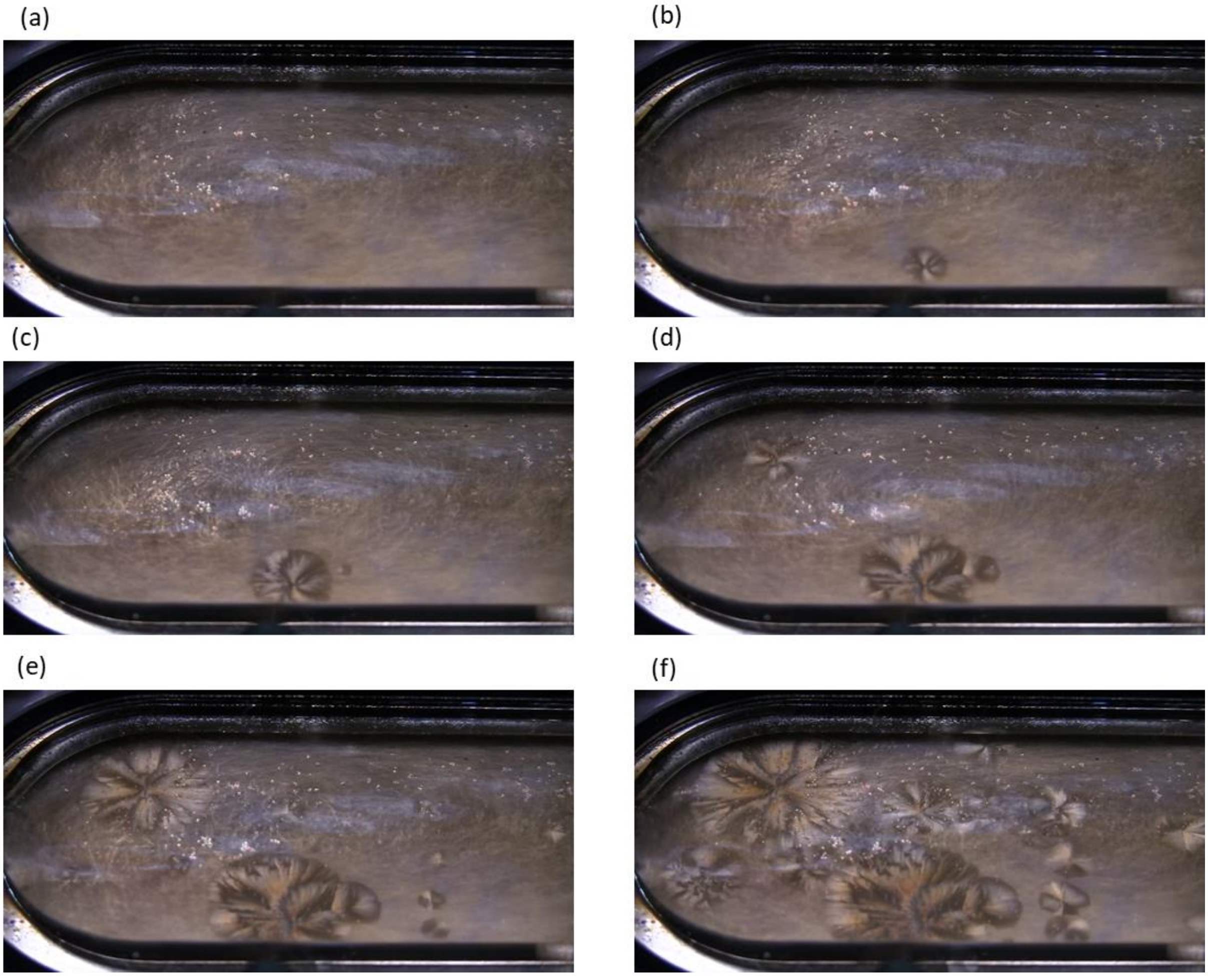

Figure A.13: *DIC photographs of ice scale formation on Copper at normalised thermal conductivities, where (a) is the frame before an initial visible nucleation site is detected and frames (b) to (f) are 0.4s, 0.8s, 1,2s, 1.6s and 2s after the nucleation site detected.*

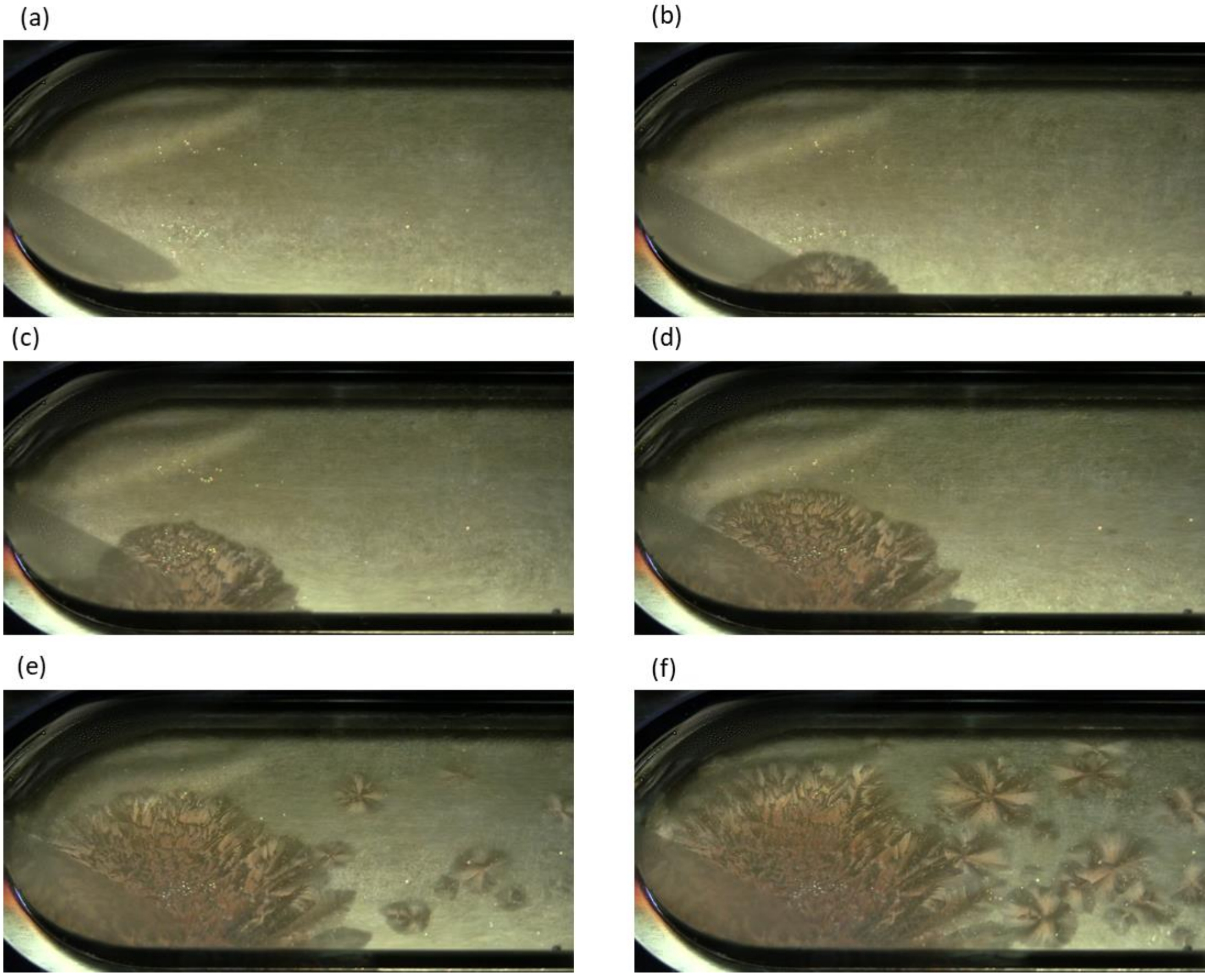

Figure A.14: *DIC photographs of ice scale formation on Brass at normalised thermal conductivities, where (a) is the frame before an initial visible nucleation site was detected and frames (b) to (f) are 0.4s, 0.8s, 1,2s, 1.6s and 2s after the detectable nucleation site was detected.*

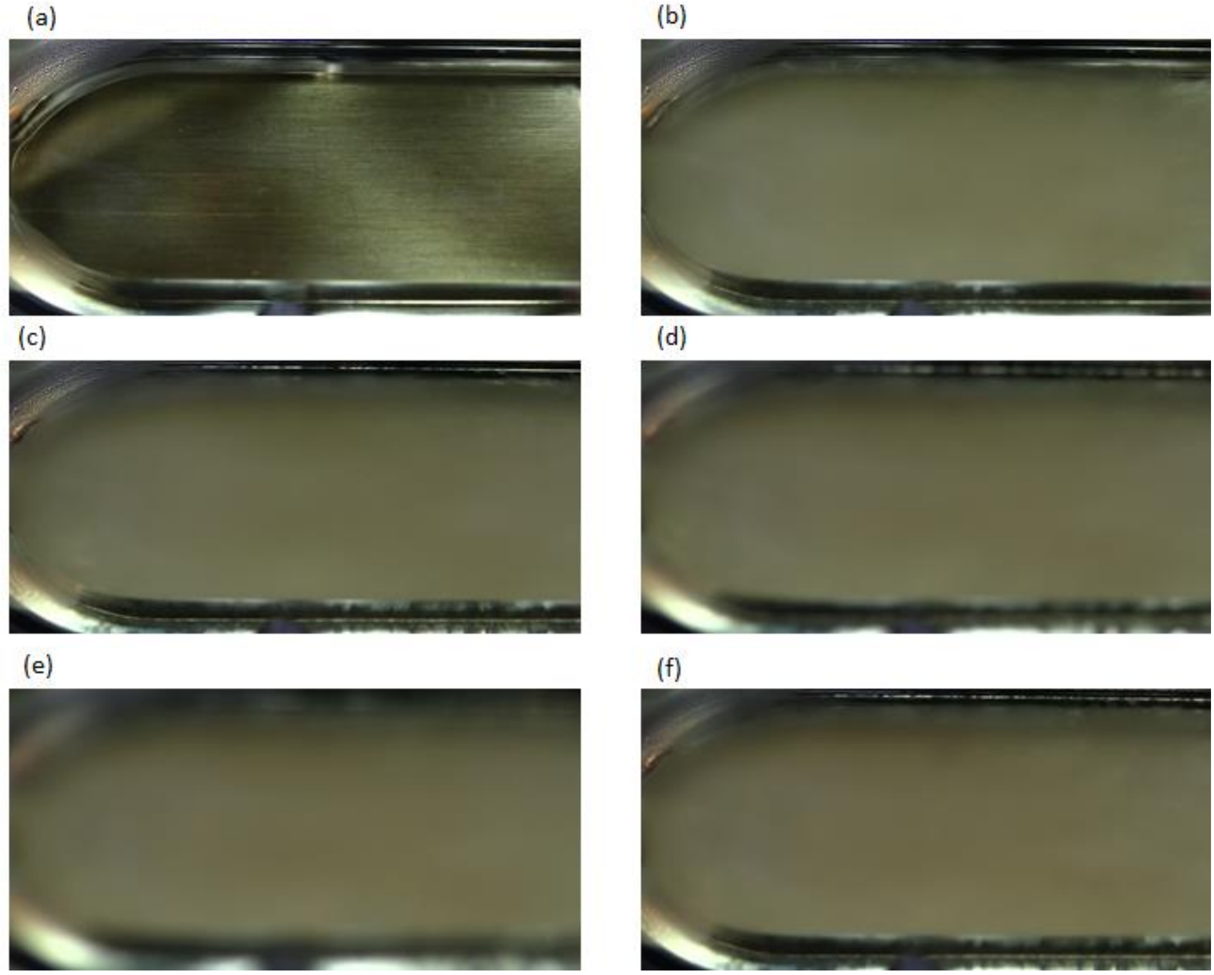

Figure A.15*: DIC photographs of bulk ice nucleation when using the Brass plate at normalised thermal conductivities where bulk nucleation occurred before scaling, where (a) is the frame before bulk ice nucleation occurred, and frames (b) to (f) are 0.4s, 0.8s, 1,2s, 1.6s and 2s after the nucleation site was detected.*

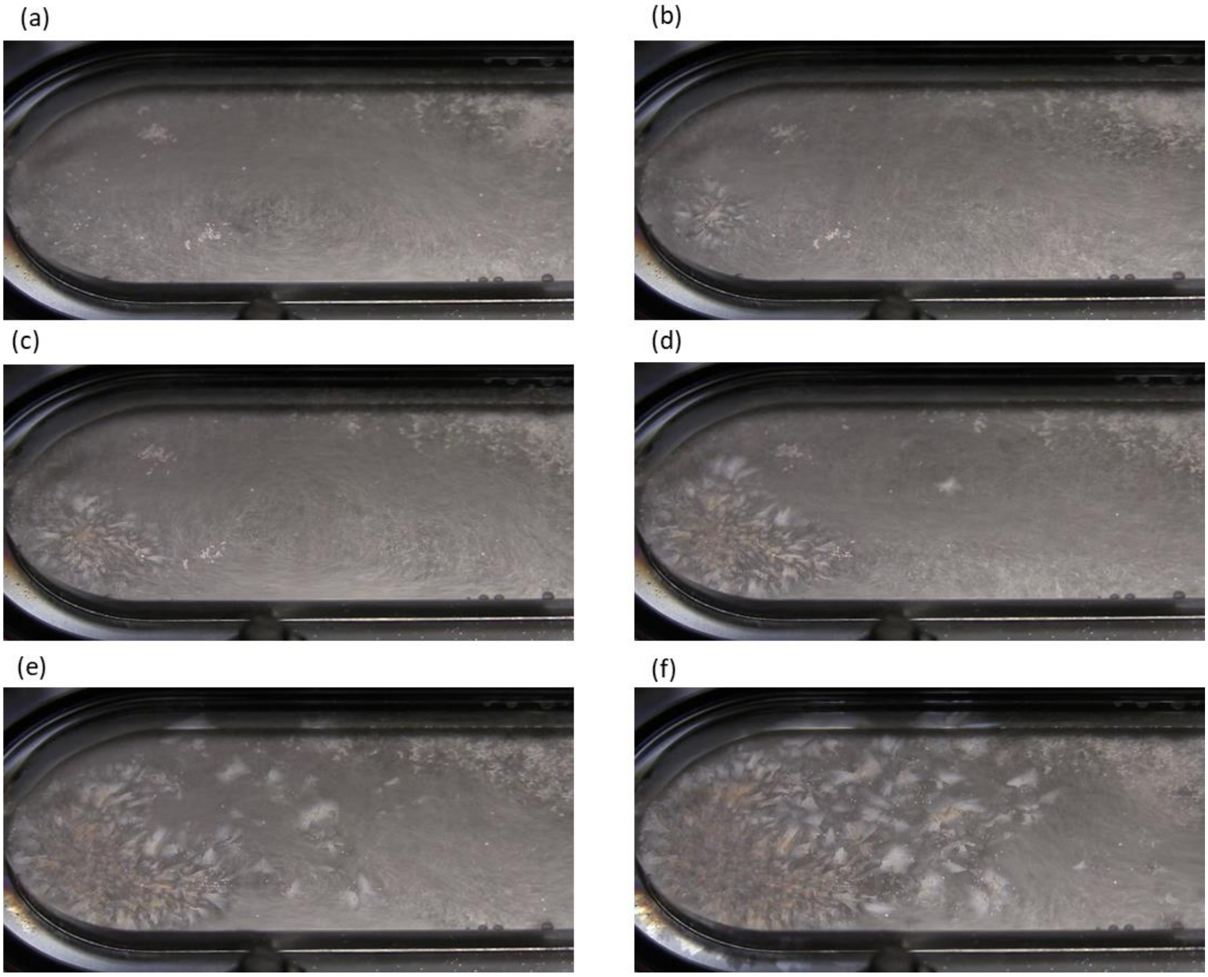

Figure A.16: *DIC photographs of ice scale formation on Primary SS316 at a coolant temperature of -15°C where (a) is the frame before a visible nucleation site was detected and frames (b) to (f) are 0.4s, 0.8s, 1,2s, 1.6s and 2s after the nucleation site was detected.*

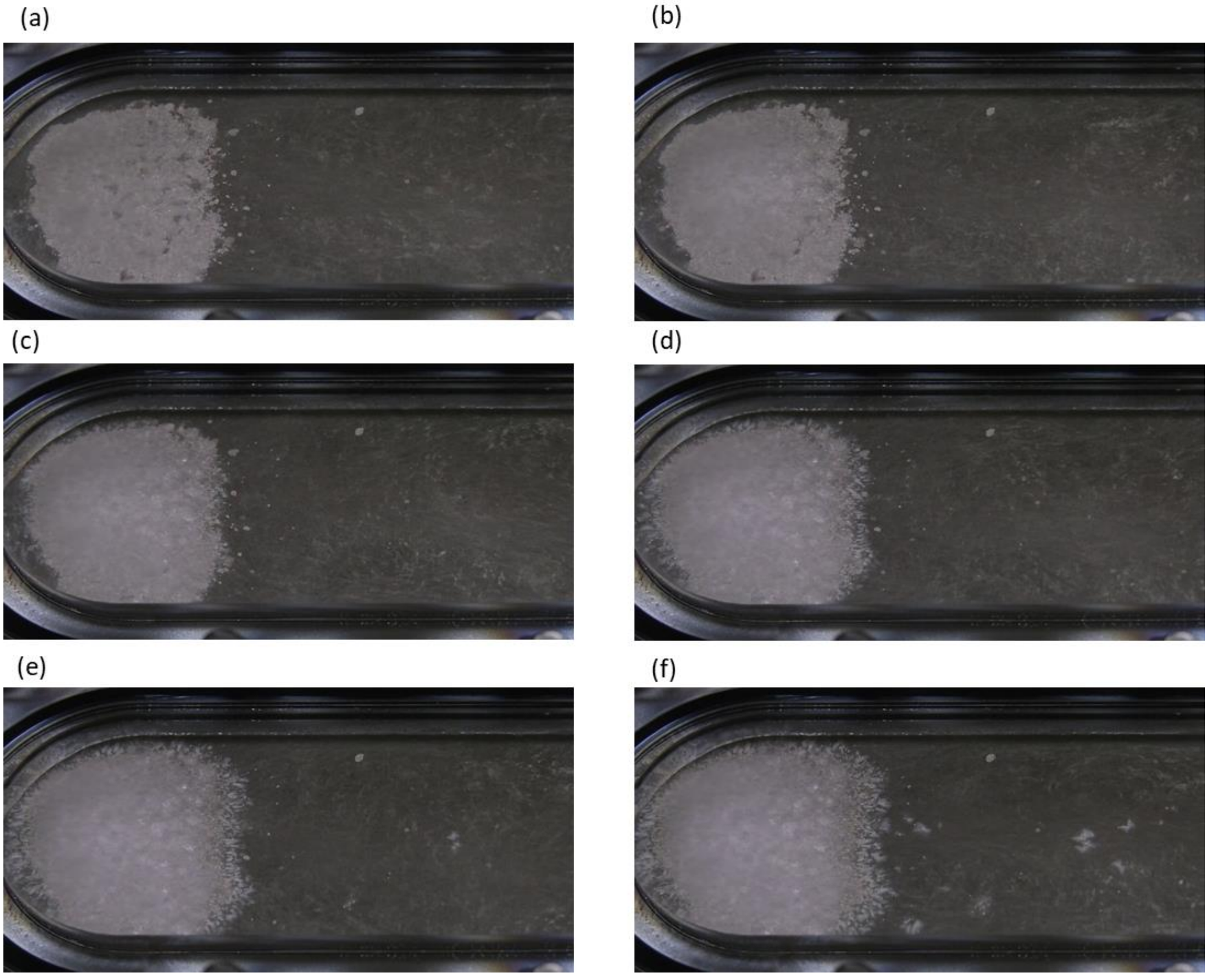

Figure A.17: *DIC photographs of ice scale formation on Rough SS316 at a coolant temperature of -15°C where (a) is the frame before an initial visible nucleation site was detected and frames (b) to (f) are 0.4s, 0.8s, 1,2s, 1.6s and 2s after the nucleation site was detected.*

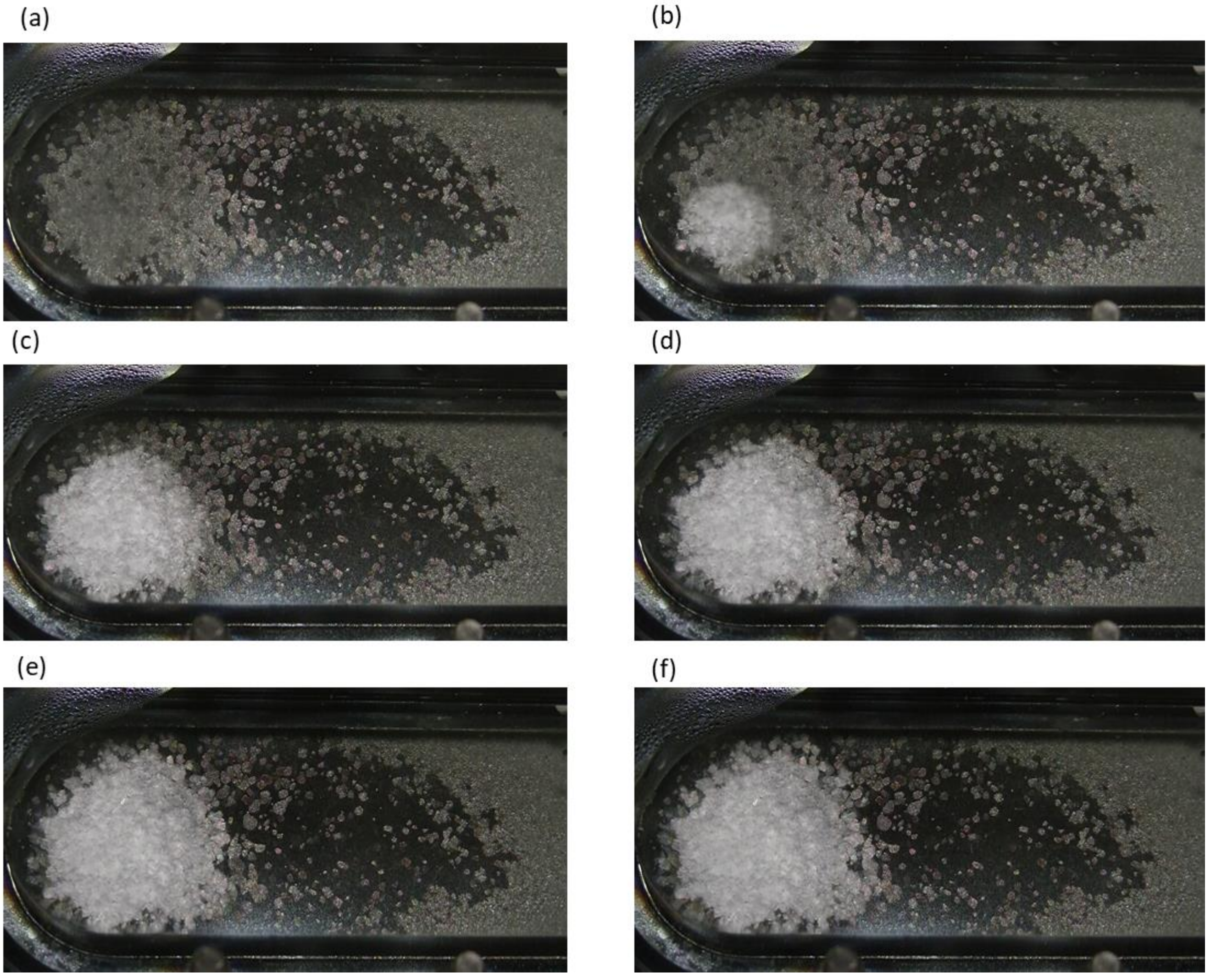

Figure A.18: *DIC photographs of ice scale formation on Coated SS316 at a coolant temperature of -15°C where (a) is the frame before a visible nucleation site was detected and frames (b) to (f) are 0.4s, 0.8s, 1,2s, 1.6s and 2s after the nucleation site was detected.*

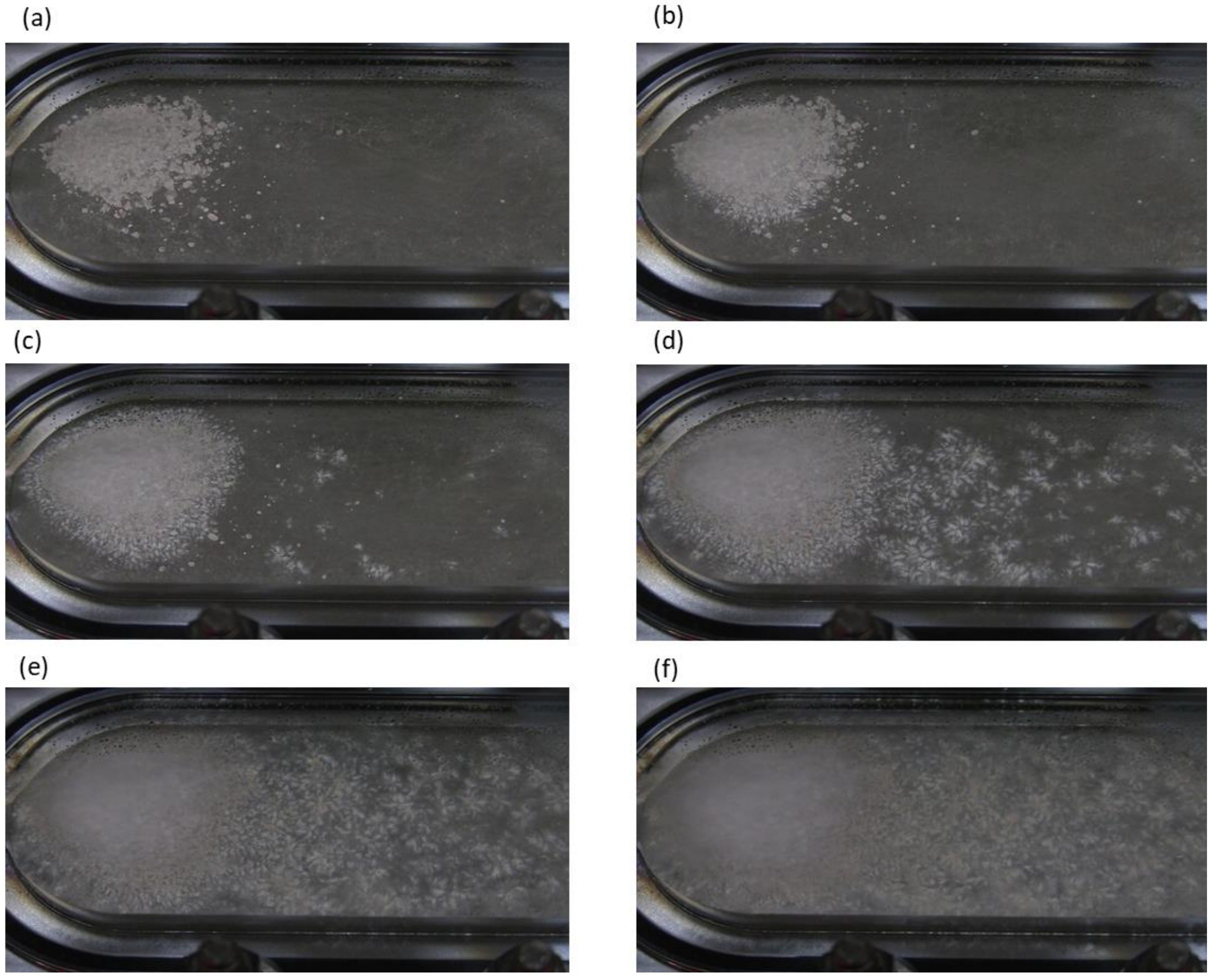

Figure A.19: *DIC photographs of ice scale formation on Rough SS316 at a coolant temperature of -20°C where (a) is the frame before an initial visible nucleation site was detected and frames (b) to (f) are 0.4s, 0.8s, 1,2s, 1.6s and 2s after the nucleation site was detected.*

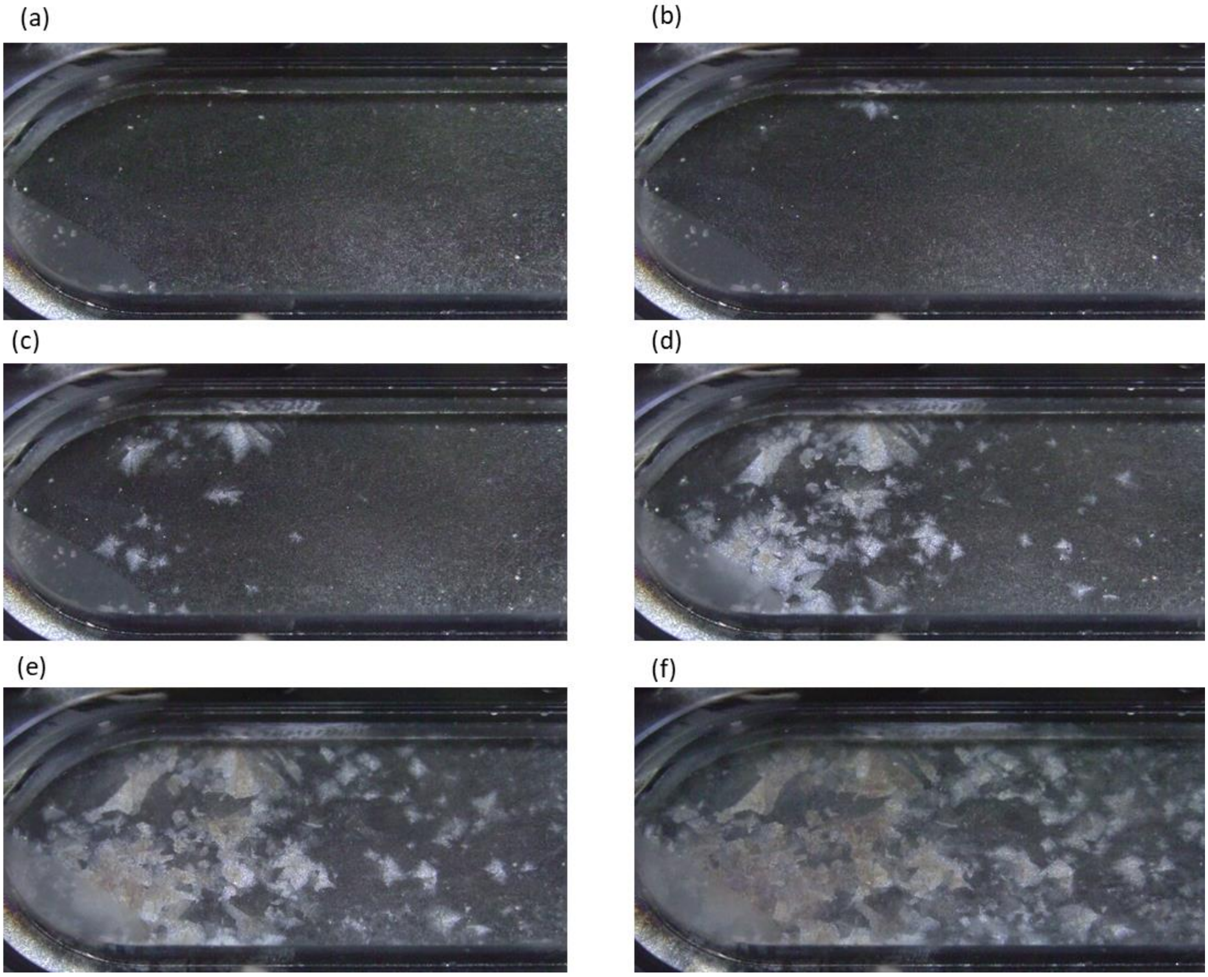

Figure A.20: *DIC photographs of ice scale formation on Coated SS316 at a coolant temperature of -20°C where (a) is the frame before an initial visible nucleation site was detected and frames (b) to (f) are 0.4s, 0.8s, 1,2s, 1.6s and 2s after the nucleation site was detected.*

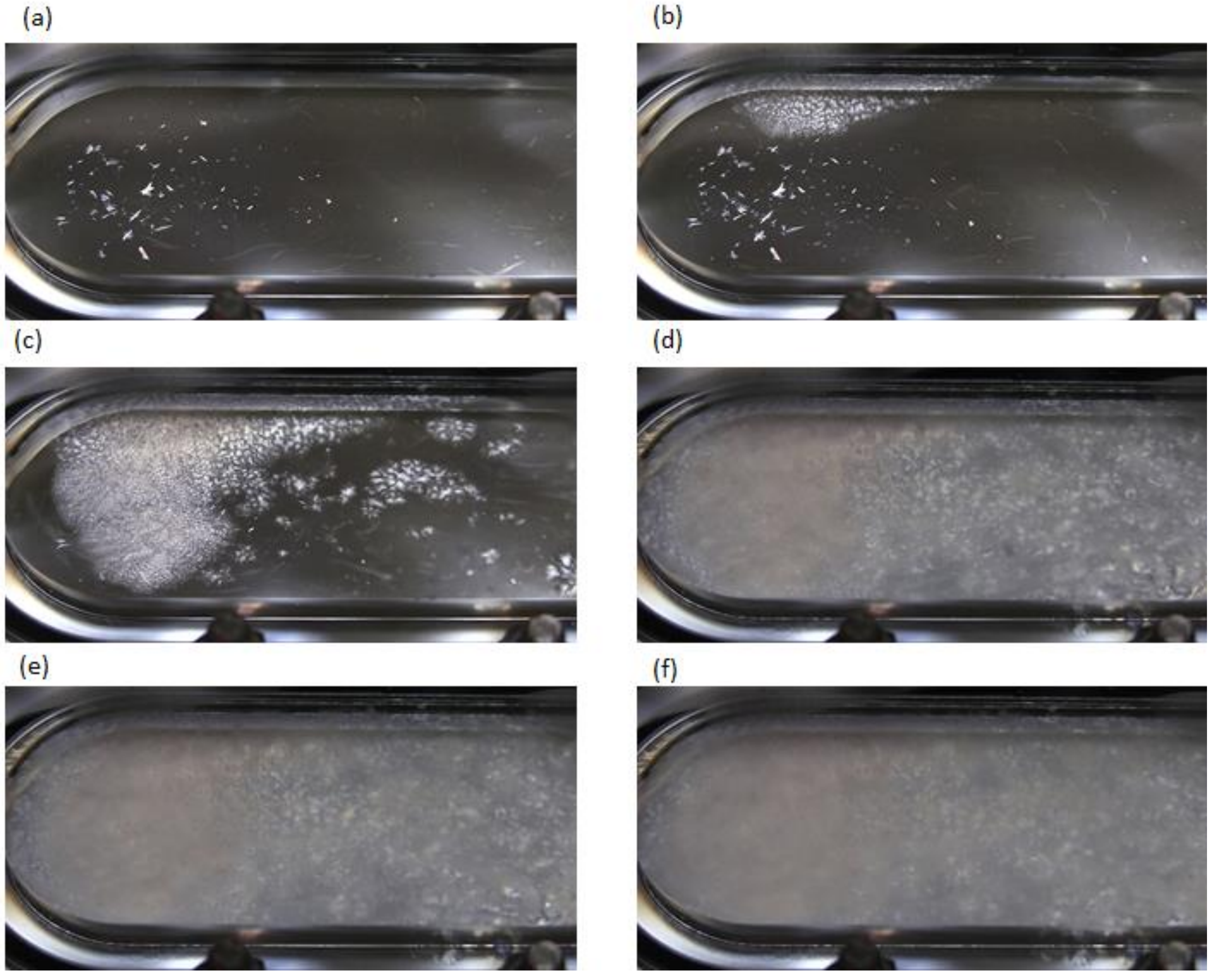

Figure A.21: *DIC photographs of ice scale formation on Primary SS316 at a coolant temperature of -25°C where (a) is the frame before an initial visible nucleation site was detected and frames (b) to (f) are 0.4s, 0.8s, 1,2s, 1.6s and 2s after the nucleation site was detected.*

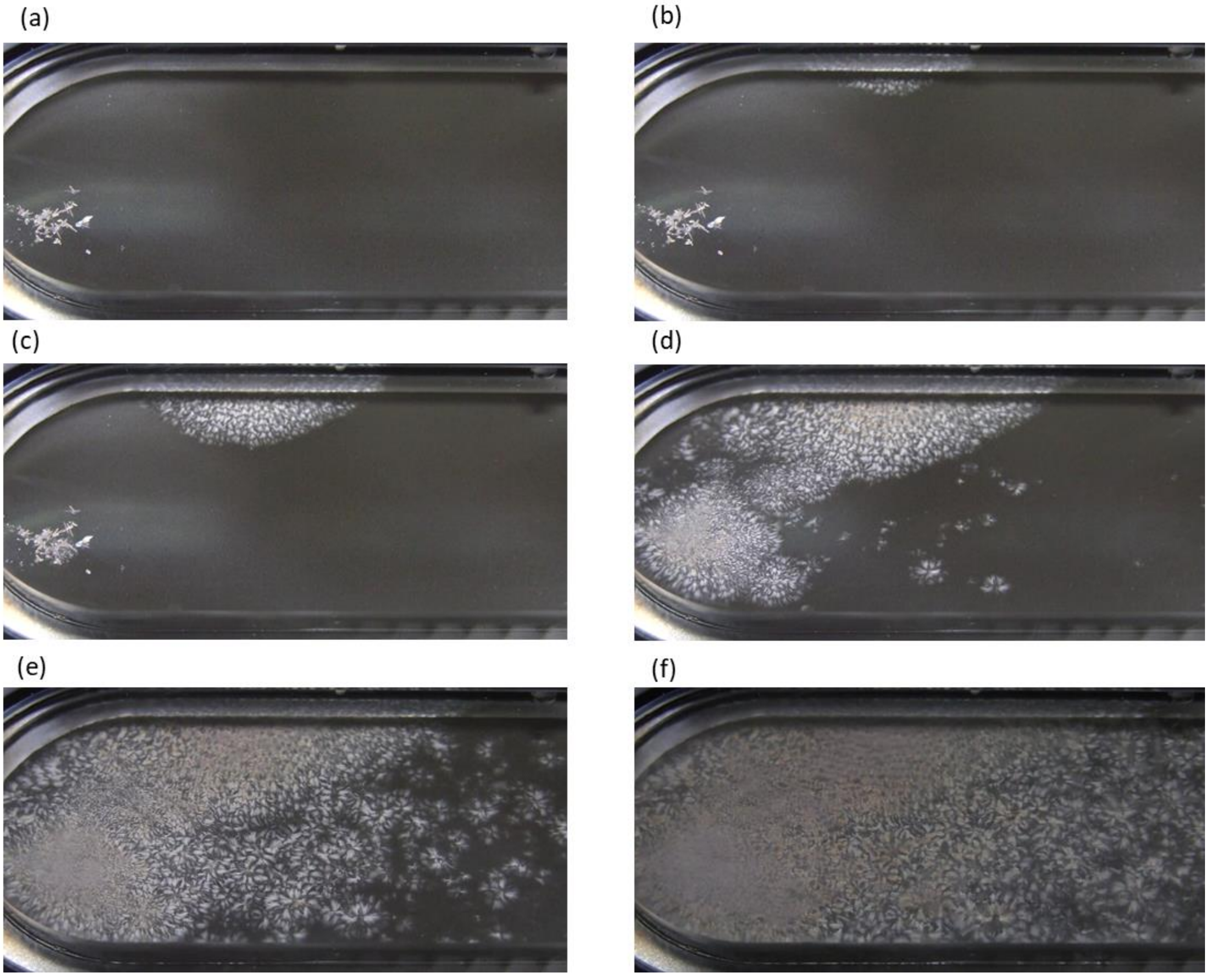

Figure A.22: *DIC photographs of ice scale formation on Rough SS316 at a coolant temperature of -25°C where (a) is the frame before an initial visible nucleation site was detected and frames (b) to (f) are 0.4s, 0.8s, 1,2s, 1.6s and 2s after the nucleation site was detected.*

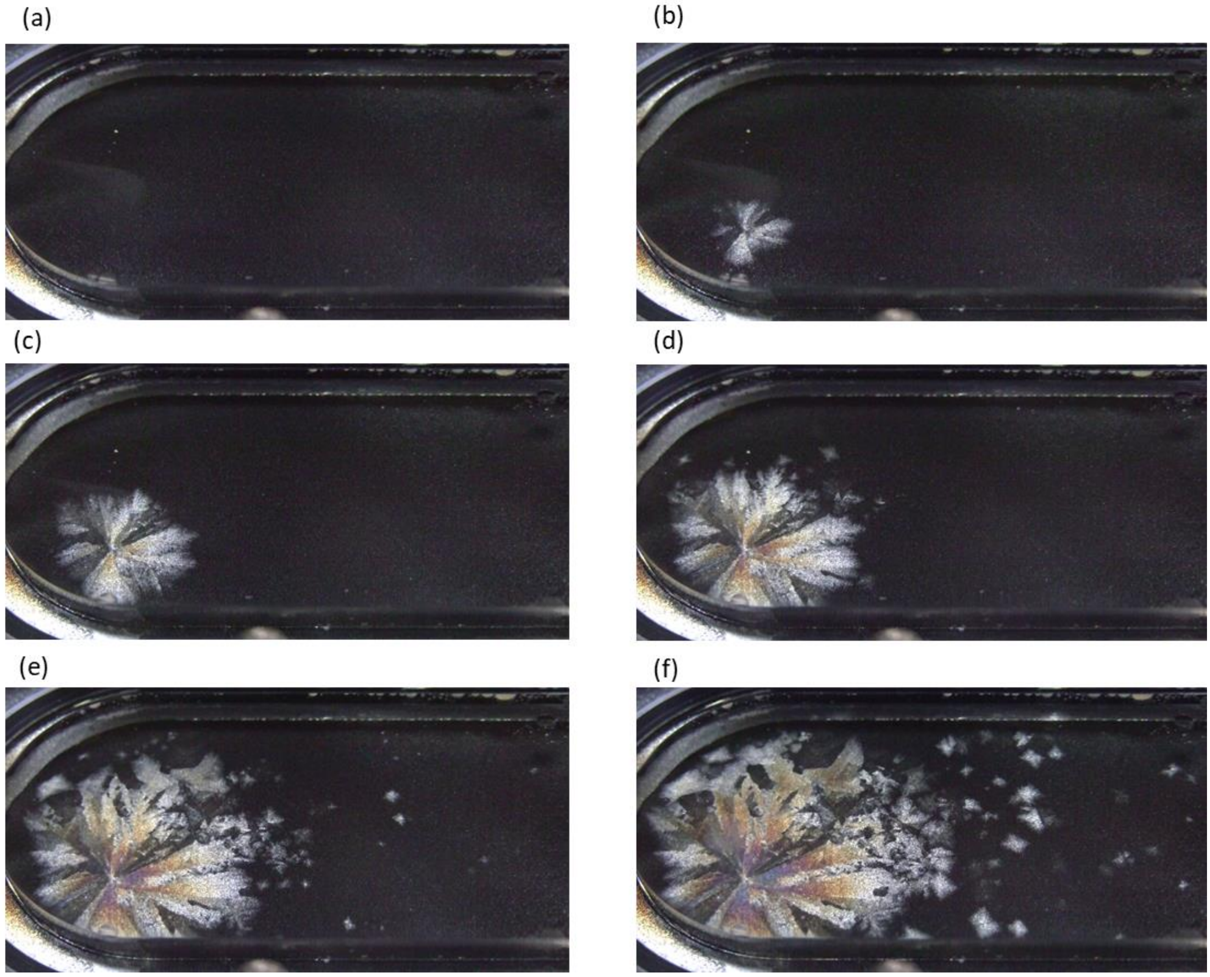

Figure A.23: *DIC photographs of ice scale formation on Coated SS316 at a coolant temperature of -25°C where (a) is the frame before an initial nucleation site was detected and frames (b) to (f) are 0.4s, 0.8s, 1,2s, 1.6s and 2s after the nucleation site was detected.*